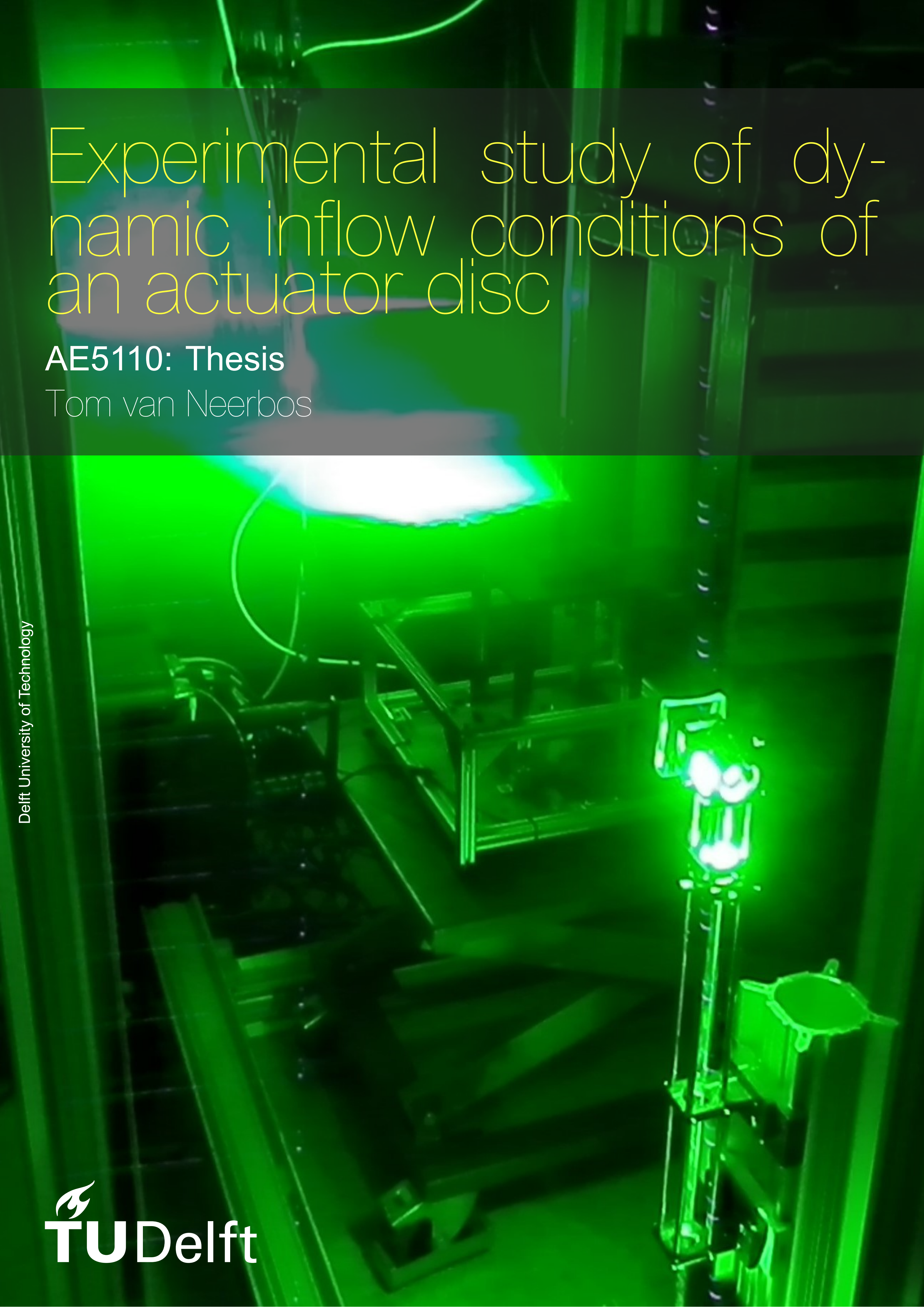

Experimental study of dynamic inflow conditions of an actuator disc

AE5110: Thesis

Tom van Neerbos

Delft University of Technology

TUDelft

Experimental study of dynamic inflow conditions of an actuator disc

by

Tom van Neerbos

Student Name	Student Number
Tom van Neerbos	4276663

Thesis committee:	Prof. Dr. Ir Carlos Simao Ferreira
	Dr. Wei Yu
	Dr. Andrea Sciacchitano
Project Duration:	February, 2022 - November, 2022
Faculty:	Faculty of Aerospace Engineering, Delft

Abstract

The main objective of this master's thesis report is to experimentally investigate the effects of dynamic inflow conditions on the wake of an actuator disc. Dynamic inflow is the unsteady wake in momentum theory. Dynamic inflow can experimentally be generated by a gust generator. During the experiments, in which Particle Image Velocimetry (PIV) was used as a flow measurement technique, the gust generator produced different gust frequencies and gust amplitudes. The oscillating gust results in the oscillating wake of the actuator disc. The oscillations of the wake cause wake expansion and compression. The expansion and compression of the wake is mainly dependent on the gust frequency. The higher the gust frequency is, the more oscillations the wake will see.

Acknowledgement

I would like to express my deepsest gratitude to Dr. Wei Yu for her incredible support during the literature study, and master thesis post-processing. I am extremely grateful to Prof. Ferreira for his effort to change the master thesis topic, due to delivery problems and long waiting times of components. Besides, words cannot express my gratitude for his idea to set the camera frequency equal to the gust vane frequency. This simple action helped a lot in the reduction of post-processing time.

Many thanks to David; Quanqun, and Abhratej for there support during the experiments, and their help in post-processing. I am also grateful for Dr. Sodja, who lent me his gust generator. Without his gust generator, the dynamic inflow conditions could not be simulated in the W-Tunnel. Thanks should also go to Dr. Sciacchitano for his support during the experiments, and his help in post-processing.

I would like to acknowlegde Siddharth for his help with the DaVis software. Besides, the actuator discs could not made without help, and support from Johan of the DEMO workshop.

Summary

The actuator disc model is a simplified method to calculate flow effects of a wind turbine. The method assumes incompressible, steady, one-dimensional flow. Dynamic inflow describes the unsteady wake-induced velocity. For dynamic inflow simulations, there are several options to simulate it. For numerical analysis, engineering models of Stig Øye; Pitt-Peters, and the ECN model can be used to simulate dynamic inflow conditions. Several analyses have been done in the past into these models. Besides numerical analysis, experiments in wind tunnels have also been done on dynamic inflow conditions. Dynamic inflow conditions in a wind tunnel are simulated by so-called active grids.

The main objective of this master's thesis is to investigate the effect of dynamic inflow conditions on an actuator disc. The experiments were done in the W-Tunnel of Delft's University of Technology. A specially designed gust generator can be mounted to the exit of the open wind tunnel. Three actuator discs with different porosities have been manufactured.

The wind tunnel data is collected by two cameras in a Particle Image Velocimetry (PIV) set-up. The captured images are analysed with software for intelligent imaging. Several test cases were done during the experiments. In the test cases, there are three variables:

- Porosity, or change of actuator disc. In total four different settings, namely the three different actuator discs, and one case without disc.
- The gust vane amplitude.
- The gust vane frequency

After several trials, the set-up was changed. The second camera was shifted downstream to also have a view of the area further downstream. Due to time limitations in the wind tunnel, only some tests were repeated to extend the captured flow field.

The flow field shows the wake of the gust vanes together with the wake of the actuator discs. The wake of the actuator disc is expanding and compressing due to the oscillating wakes of the gust vanes. The main difference between the change in gust frequency is the behavior of the wake of the actuator disc. The wake is expanding, and compressing for both low and high gust frequencies. In high frequency cases, the wake is compressed exactly at opposite gust vane angles in comparison to low gust frequency cases. This is the result of the faster oscillating gusts in high frequency cases. The gust amplitude shows a change in the induction upstream of the actuator disc. The induction is dependent on the gust phase in combination with the gust amplitude. The induction for high gust amplitudes is much further upstream than for lower gust amplitudes.

The thrust coefficients are calculated from the velocity field using a linear interpolation method. The thrust coefficients of the two actuator discs with the lowest porosity are closest to literature data. The third actuator disc shows a slightly different behavior to the steady case. However, if a gust is introduced to the flow field, it increases or decreases the thrust coefficient. The results of the actuator discs with the lowest porosities are still close to literature data. The third actuator disc shows similar behavior as the other two discs, except for one case which is close to the steady case of the third disc. During the experiments, the actuator discs were changed by hand, which added small errors, even with a mark on the actuator disc.

Contents

Abstract iii

Acknowledgement v

Summary vii

1 Introduction 1
- 1.1 Project overview . . . 1
- 1.2 Project objective . . . 1
- 1.3 Report overview . . . 2

2 Background 3
- 2.1 Actuator Disc model . . . 3
  - 2.1.1 Actuator disc model . . . 3
  - 2.1.2 The assumptions in Momentum theory . . . 7
- 2.2 Dynamic inflow . . . 7
  - 2.2.1 Modelling dynamic inflow . . . 8
  - 2.2.2 Stig Øye dynamic inflow model . . . 8
  - 2.2.3 Pitt-Peters dynamic inflow model . . . 9
  - 2.2.4 ECN dynamic inflow model . . . 9
- 2.3 The wake of the wind turbine . . . 9
  - 2.3.1 Near wake . . . 10
  - 2.3.2 Far wake . . . 11
- 2.4 Flow phenomena . . . 11
  - 2.4.1 Vortex ring system . . . 12
  - 2.4.2 Wake meandering . . . 12
- 2.5 Particle Image Velocimetry . . . 13

3 Experimental and numerical work on Actuator Discs 15
- 3.1 Numerical work dynamic inflow conditions . . . 15
- 3.2 Experimental work dynamic inflow conditions . . . 16
  - 3.2.1 Active grid . . . 16
  - 3.2.2 Experimental work with active grids . . . 19
- 3.3 Actuator disc design for experimental work . . . 21

4 Experimental set-up and test cases 23
- 4.1 Experimental set-up . . . 23
  - 4.1.1 Wind tunnel . . . 23
  - 4.1.2 Gust generator . . . 24
  - 4.1.3 Particle Image Velocimetry . . . 25
  - 4.1.4 Actuator disc design . . . 27
  - 4.1.5 Actuator disc mounting . . . 28
  - 4.1.6 Final set-up . . . 29
- 4.2 Test cases . . . 30
- 4.3 Image processing . . . 32
- 4.4 Gust vane amplitude . . . 33

5 Results and discussion of steady cases 35

6 Results and discussion of unsteady cases 39
- 6.1 Gust . . . 39
- 6.2 Flow field . . . 42
- 6.3 Pearson correlation coefficient . . . 52

6.4 Proper Orthogonal Decomposition . . . 55
6.5 Wake expansion and compression . . . 59
6.6 Upstream induction field . . . 61
6.7 Actuator disc thrust . . . 62

7 Uncertainty estimation **67**
7.1 Uncertainties . . . 67
7.2 Uncertainty in PIV . . . 68

8 Conclusion and recommendations **69**
8.1 Conclusion . . . 69
8.2 Recommendations . . . 70

References **71**

A Appendix A **75**
A.1 Steady cases . . . 75
A.2 Unsteady cases . . . 76

B Appendix B **81**

C Appendix C **83**
C.1 Velocity fluctuations steady cases . . . 83
C.2 Convergence steady cases . . . 86

D Appendix D **89**

List of Figures

2.1 Streamlines, axial velocity and pressure [18] 4
2.2 Rectangular control volume [18] 5
2.3 Alternative control volume [18] 5
2.4 Thrust and power coefficients with respect to axial induction factor [18] 6
2.5 Wake mixing [47] 7
2.6 Wake of wind turbine [46] 10
2.7 Wake of wind turbine [26] 11
2.8 Side view of a vortex ring [4] 12
2.9 Wake of a wind turbine [9] 12
2.10 Turbulent inflow: contours of the instantaneous velocity field behind the wind turbine on the horizontal plane at hub height. (a) streamwise velocity using AD; (b) streamwise velocity using AS; The solid black line at x = 0 illustrates the location and the diameter of the wind turbine; (c) streamwise velocity of the turbulent inflow without wind turbine [30] 13
2.11 Experimental arrangement of PIV in a wind tunnel [44] 14

3.1 Experimental set up, units in mm. [33] 16
3.2 Active grid [24] 17
3.3 Technical drawing of the 2D active grid containing the stepper motors (1–9), the gauge of the shafts gshaft, the span of the shafts sshaft and the chord length of the shafts cshaft. At the right side, the definition of shaft angle γ is shown (top view onto the shaft) [25] . . 17
3.4 Shafts for the 2D active grid. I: Flat plates with a chord length of 90 mm. II: NACA0018 airfoils with a chord length of 71 mm. III: NACA0009 with a chord length of 180 mm. The red mark indicates the pivot point. [25] 18
3.5 Shaft setups of the 2D active grid as top view on the shafts. i shows a setup with nine shafts, ii uses six shafts and in iii only two shafts of type NACA0009 are installed. [25] . 18
3.6 Gust generator with laser light [16] 19
3.7 Experimental set-up (a) and Schematic set-up (b) [8] 20
3.8 Set-up [29] 20
3.9 Experimental setup, showing the three model turbines mounted on the wind tunnel turntable. The x–y–z frame is fixed with respect to the tunnel and does not rotate with the turntable. [10] 21
3.10 C_T versus porosity [22] 22
3.11 Normalised streamwise velocity. Circular (top), square (middle), rectangular (bottom) actuator. The white contour line represents the location where the wake attains 50% of the free-stream-value. The white patch is placed in an area with high uncertainty, due to an accidently increased background reflection. [22] 22

4.1 W-Tunnel 24
4.2 Gust vane generator 24
4.3 Indication of the movement of the gust vanes 25
4.4 Gust generator cosine 25
4.5 Gust generator sine 25
4.6 PIV Camera [38] 26
4.7 PTU [38] 26
4.8 Schematic set-up with camera two in original position 27
4.9 Schematic set-up with camera two in shifted position 27
4.10 Designed actuator discs. From left to right: Disc 3; Disc 2, and Disc 1. 28
4.11 Tower 29
4.12 Original set-up 30

4.13 Set-up with shifted camera and laser . . . 30
4.14 Flow field camera two in upwind position . . . 32
4.15 Flow field camera two in downstream position . . . 32
4.16 Gust vane positive and negative angle . . . 33

5.1 Combined non-dimensional velocity field steady cases; top left no disc; top right disc 1; bottom left disc 2; bottom right disc 3 . . . 36
5.2 Combined non-dimensional vorticity field steady cases; top left no disc; top right disc 1; bottom left disc 2; bottom right disc 3 . . . 37

6.1 Comparison gust of steady case versus unsteady case; disc 1; 5 degree amplitude; 6Hz 40
6.2 Comparison gust of case with disc versus case without disc; disc 1; 5 degree amplitude; 6Hz . . . 40
6.3 Comparison gust of steady case versus unsteady case; disc 1; 5 degree amplitude; 12Hz 41
6.4 Comparison gust of case with disc versus case without disc; disc 1; 5 degree amplitude; 12Hz . . . 41
6.5 Comparison gust of steady case versus unsteady case; disc 1; 6.5 degree amplitude, 12Hz 42
6.6 Comparison gust of case with disc versus case without disc; disc 1; 6.5 degree amplitude, 12Hz . . . 42
6.7 No disc; non-dimensional velocity field; 5 degree amplitude; 6Hz; left positive gust vane angle; right negative gust vane angle . . . 43
6.8 Disc 1; non-dimensional velocity field; 5 degree amplitude; 6Hz; left positive gust vane angle; right negative gust vane angle . . . 43
6.9 Disc 2; non-dimensional velocity field; 5 degree amplitude; 6Hz; left positive gust vane angle; right negative gust vane angle . . . 43
6.10 Disc 3; non-dimensional velocity field; 5 degree amplitude; 6Hz; left positive gust vane angle; right negative gust vane angle . . . 44
6.11 No disc; non-dimensional vorticity field; 5 degree amplitude; 6Hz; left positive gust vane angle; right negative gust vane angle . . . 44
6.12 Disc 1 non-dimensional vorticity field; 5 degree amplitude; 6Hz; left positive gust vane angle; right negative gust vane angle . . . 44
6.13 Disc 2; non-dimensional vorticity field; 5 degree amplitude; 6Hz; left positive gust vane angle; right negative gust vane angle . . . 45
6.14 Disc 3 non-dimensional vorticity field; 5 degree amplitude; 6Hz; left positive gust vane angle; right negative gust vane angle . . . 45
6.15 No disc; non-dimensional velocity field; 5 degree amplitude; 12Hz; left positive gust vane angle; right negative gust vane angle . . . 45
6.16 Disc 1 non-dimensional velocity field; 5 degree amplitude; 12Hz; left positive gust vane angle; right negative gust vane angle . . . 46
6.17 Disc 2; non-dimensional velocity field; 5 degree amplitude; 12Hz; left positive gust vane angle; right negative gust vane angle . . . 46
6.18 Disc 3 non-dimensional velocity field; 5 degree amplitude; 12Hz; left positive gust vane angle; right negative gust vane angle . . . 46
6.19 No disc; non-dimensional vorticity field; 5 degree amplitude; 12Hz; left positive gust vane angle; right negative gust vane angle . . . 46
6.20 Disc 1 non-dimensional vorticity field; 5 degree amplitude; 12Hz; left positive gust vane angle; right negative gust vane angle . . . 47
6.21 Disc 2; non-dimensional vorticity field; 5 degree amplitude; 12Hz; left positive gust vane angle; right negative gust vane angle . . . 47
6.22 Disc 3 non-dimensional vorticity field; 5 degree amplitude; 12Hz; left positive gust vane angle; right negative gust vane angle . . . 47
6.23 No disc; non-dimensional velocity field; 6.5 degree amplitude; 12Hz; left positive gust vane angle; right negative gust vane angle . . . 47
6.24 Disc 1; non-dimensional velocity field; 6.5 degree amplitude 12Hz; left positive gust vane angle; right negative gust vane angle . . . 48

6.25 Disc 2; non-dimensional velocity field; 6.5 degree amplitude; 12Hz; left positive gust vane angle; right negative gust vane angle . . . 48
6.26 Disc 3; non-dimensional velocity field; 6.5 degree amplitude 12Hz; left positive gust vane angle; right negative gust vane angle . . . 48
6.27 No disc; non-dimensional vorticity field; 6.5 degree amplitude; 12Hz; left positive gust vane angle; right negative gust vane angle . . . 48
6.28 Disc 1; non-dimensional vorticity field; 6.5 degree amplitude; 12Hz; left positive gust vane angle; right negative gust vane angle . . . 49
6.29 Disc 2; non-dimensional vorticity field; 6.5 degree amplitude; 12Hz; left positive gust vane angle; right negative gust vane angle . . . 49
6.30 Disc 3; non-dimensional vorticity field; 6.5 degree amplitude; 12Hz; left positive gust vane angle; right negative gust vane angle . . . 49
6.31 No disc; non-dimensional velocity field; 6.5 degree amplitude; 6Hz; left positive gust vane angle; right negative gust vane angle . . . 49
6.32 Disc 2; non-dimensional velocity field; 6.5 degree amplitude; 6Hz; left positive gust vane angle; right negative gust vane angle . . . 50
6.33 No disc; non-dimensional vorticity field; 6.5 degree amplitude; 6Hz; left positive gust vane angle; right negative gust vane angle . . . 50
6.34 Disc 2; non-dimensional vorticity field; 6.5 degree amplitude; 6Hz; left positive gust vane angle; right negative gust vane angle . . . 50
6.35 No disc; non-dimensional velocity field; 10 degree amplitude; 6Hz; left positive gust vane angle; right negative gust vane angle . . . 50
6.36 Disc 1; non-dimensional velocity field; 10 degree amplitude; 6Hz; left positive gust vane angle; right negative gust vane angle . . . 51
6.37 Disc 2; non-dimensional velocity field; 10 degree amplitude; 6Hz; left positive gust vane angle; right negative gust vane angle . . . 51
6.38 Disc 3; non-dimensional velocity field; 10 degree amplitude; 6Hz; left positive gust vane angle; right negative gust vane angle . . . 51
6.39 No disc; non-dimensional vorticity field; 10 degree amplitude; 6Hz; left positive gust vane angle; right negative gust vane angle . . . 51
6.40 Disc 1; non-dimensional vorticity field; 10 degree amplitude; 6Hz; left positive gust vane angle; right negative gust vane angle . . . 52
6.41 Disc 2; non-dimensional vorticity field; 10 degree amplitude; 6Hz; left positive gust vane angle; right negative gust vane angle . . . 52
6.42 Disc 3; non-dimensional vorticity field; 10 degree amplitude; 6Hz; left positive gust vane angle; right negative gust vane angle . . . 52
6.43 Pearson correlation coefficient; no disc; 5 degree amplitude; 6Hz . . . 53
6.44 Pearson correlation coefficient; disc 2; 5 degree amplitude; 6Hz . . . 53
6.45 Pearson correlation coefficient; disc 1; 5 degree amplitude; 6Hz . . . 53
6.46 Pearson correlation coefficient; disc 3; 5 degree amplitude; 6Hz . . . 53
6.47 Pearson correlation coefficient; no disc; 5 degree amplitude; 12Hz . . . 54
6.48 Pearson correlation coefficient; disc 2; 5 degree amplitude; 12Hz . . . 54
6.49 Pearson correlation coefficient; disc 1; 5 degree amplitude; 12Hz . . . 54
6.50 Pearson correlation coefficient; disc 3; 5 degree amplitude; 12Hz . . . 54
6.51 Pearson correlation coefficient; 6.5 degree amplitude; 12Hz; top left no disc; top right disc 1; bottom left disc 2; bottom right disc 3 . . . 54
6.52 Pearson correlation coefficient; 6.5 degree amplitude; 6Hz; left no disc; right disc 2 . . . 55
6.53 Pearson correlation coefficient; 10 degree amplitude; 6Hz; top left no disc; top right disc 1; bottom left disc 2; bottom right disc 3 . . . 55
6.54 POD eigenvalues; disc 1; ; 5 degree amplitude; 6Hz . . . 56
6.55 No disc, POD mode 1; 5 degree amplitude; 6Hz . . . 56
6.56 No disc, POD mode 2; 5 degree amplitude; 6Hz . . . 56
6.57 No disc, POD mode 3; 5 degree amplitude; 6Hz . . . 56
6.58 No disc, POD mode 4; 5 degree amplitude; 6Hz . . . 56
6.59 Disc 2, POD mode 3; 5 degree amplitude; 6Hz . . . 57
6.60 Disc 2, POD mode 4; 5 degree amplitude; 6Hz . . . 57

6.61 No disc, POD mode 3; 5 degree amplitude; 12Hz . . . 57
6.62 No disc, POD mode 4; 5 degree amplitude; 12Hz . . . 57
6.63 Disc 2, POD mode 3; 5 degree amplitude; 12Hz . . . 57
6.64 Disc 2, POD mode 4; 5 degree amplitude; 12Hz . . . 57
6.65 No disc, POD mode 3; 6.5 degree amplitude; 12Hz . . . 58
6.66 No disc, POD mode 4; 6.5 degree amplitude; 12Hz . . . 58
6.67 Disc 2, POD mode 3; 6.5 degree amplitude; 12Hz . . . 58
6.68 Disc 2, POD mode 4; 6.5 degree amplitude; 12Hz . . . 58
6.69 No disc, POD mode 3; 6.5 degree amplitude; 6Hz . . . 58
6.70 No disc, POD mode 4; 6.5 degree amplitude; 6Hz . . . 58
6.71 Disc 2, POD mode 3; 6.5 degree amplitude; 6Hz . . . 58
6.72 Disc 2, POD mode 4; 6.5 degree amplitude; 6Hz . . . 58
6.73 No disc, POD mode 3; 10 degree amplitude;6Hz . . . 59
6.74 No disc, POD mode 4; 10 degree amplitude; 6Hz . . . 59
6.75 Disc 2, POD mode 3; 10 degree amplitude; 6Hz . . . 59
6.76 Disc 2, POD mode 4; 10 degree amplitude; 6Hz . . . 59
6.77 Top left disc 1, 5 degree amplitude, 6Hz; top right: disc 1, 5 degree amplitude, 12Hz; bottom left disc 2, 5 degree amplitude, 6Hz; bottom right: disc 2, 5 degree amplitude, 12Hz 60
6.78 Wake expansion comparison between disc 1 and disc 2; 5 degree amplitude, 6Hz . . . 60
6.79 Wake expansion comparison between disc 1 and disc 2; 5 degree amplitude, 12Hz . . . 61
6.80 Induction changes upstream of the disc; top left: 5 degree amplitude, 6Hz; top right: 5 degree amplitude, 12Hz; bottom left: 6.5 degree amplitude, 12Hz; bottom right: 10 degree amplitude, 6Hz . . . 62
6.81 Thrust coefficient of the steady cases in comparison to literature [6] [5] [31] [37] [42] [49] [56] [22] . . . 63
6.82 The mean thrust coefficients of the unsteady cases in comparison to literature data [6] [5] [31] [37] [42] [49] [56] [22] . . . 64
6.83 Thrust coefficient incudling standard deviation; Disc 1 . . . 64
6.84 Thrust coefficient incudling standard deviation; Disc 2 . . . 65
6.85 Thrust coefficient incudling standard deviation; Disc 3 . . . 65

A.1 No disc; Dimensionless velocity versus y [D] . . . 75
A.2 No disc; Dimensionless velocity versus y [D] . . . 75
A.3 Disc 1; Dimensionless velocity versus y [D] . . . 75
A.4 Disc 1; Dimensionless velocity versus y [D] . . . 75
A.5 Disc 2; Dimensionless velocity versus y [D] . . . 76
A.6 Disc 2; Dimensionless velocity versus y [D] . . . 76
A.7 Disc 3; Dimensionless velocity versus y [D] . . . 76
A.8 Disc 3; Dimensionless velocity versus y [D] . . . 76
A.9 No disc; 5 degree amplitude, 6Hz; Dimensionless velocity versus y [D] . . . 76
A.10 No disc; 5 degree amplitude, 6Hz; Dimensionless velocity versus y [D] . . . 76
A.11 Disc 1; 5 degree amplitude, 6Hz; Dimensionless velocity versus y [D] . . . 77
A.12 Disc 1; 5 degree amplitude, 6Hz; Dimensionless velocity versus y [D] . . . 77
A.13 Disc 2; 5 degree amplitude, 6Hz; Dimensionless velocity versus y [D] . . . 77
A.14 Disc 2; 5 degree amplitude, 6Hz; Dimensionless velocity versus y [D] . . . 77
A.15 Disc 3; 5 degree amplitude, 6Hz; Dimensionless velocity versus y [D] . . . 77
A.16 Disc 3; 5 degree amplitude, 6Hz; Dimensionless velocity versus y [D] . . . 77
A.17 No disc; 5 degree amplitude, 12Hz; Dimensionless velocity versus y [D] . . . 77
A.18 No disc; 5 degree amplitude, 12Hz; Dimensionless velocity versus y [D] . . . 77
A.19 Disc 1; 5 degree amplitude, 12Hz; Dimensionless velocity versus y [D] . . . 78
A.20 Disc 1; 5 degree amplitude, 12Hz; Dimensionless velocity versus y [D] . . . 78
A.21 Disc 2; 5 degree amplitude, 12Hz; Dimensionless velocity versus y [D] . . . 78
A.22 Disc 2; 5 degree amplitude, 12Hz; Dimensionless velocity versus y [D] . . . 78
A.23 Disc 3; 5 degree amplitude, 12Hz; Dimensionless velocity versus y [D] . . . 78
A.24 Disc 3; 5 degree amplitude, 12Hz; Dimensionless velocity versus y [D] . . . 78
A.25 No disc; 10 degree amplitude, 6Hz; Dimensionless velocity versus y [D] . . . 78

A.26 No disc; 10 degree amplitude, 6Hz; Dimensionless velocity versus y [D] 78
A.27 Disc 1; 10 degree amplitude, 6Hz; Dimensionless velocity versus y [D] 79
A.28 Disc 1; 10 degree amplitude, 6Hz; Dimensionless velocity versus y [D] 79
A.29 Disc 2; 10 degree amplitude, 6Hz; Dimensionless velocity versus y [D] 79
A.30 Disc 2; 10 degree amplitude, 6Hz; Dimensionless velocity versus y [D] 79
A.31 Disc 3; 10 degree amplitude, 6Hz; Dimensionless velocity versus y [D] 79
A.32 Disc 3; 10 degree amplitude, 6Hz; Dimensionless velocity versus y [D] 79

B.1 No disc; Dimensionless velocity versus y [D] 81
B.2 No disc; Dimensionless velocity versus y [D] 81
B.3 Disc 1; Dimensionless velocity versus y [D] 81
B.4 Disc 1; Dimensionless velocity versus y [D] 81
B.5 Disc 2; Dimensionless velocity versus y [D] 82
B.6 Disc 2; Dimensionless velocity versus y [D] 82
B.7 Disc 3; Dimensionless velocity versus y [D] 82
B.8 Disc 3; Dimensionless velocity versus y [D] 82

C.1 No disc; steady case velocity fluctuations camera 1 part 1 83
C.2 No disc; steady case velocity fluctuations camera 1 part 2 83
C.3 No disc; steady case velocity fluctuations camera 1 part 3 83
C.4 No disc; steady case velocity fluctuations camera 2 part 1 83
C.5 No disc; steady case velocity fluctuations camera 2 part 2 84
C.6 No disc; steady case velocity fluctuations camera 2 part 3 84
C.7 Disc 1; steady case velocity fluctuations camera 1 part 1 84
C.8 Disc 1; steady case velocity fluctuations camera 1 part 2 84
C.9 Disc 1; steady case velocity fluctuations camera 1 part 3 84
C.10 Disc 1; steady case velocity fluctuations camera 2 part 1 84
C.11 Disc 1; steady case velocity fluctuations camera 2 part 2 84
C.12 Disc 1; steady case velocity fluctuations camera 2 part 3 84
C.13 Disc 2; steady case velocity fluctuations camera 1 part 1 85
C.14 Disc 2; steady case velocity fluctuations camera 1 part 2 85
C.15 Disc 2; steady case velocity fluctuations camera 1 part 3 85
C.16 Disc 2; steady case velocity fluctuations camera 2 part 1 85
C.17 Disc 2; steady case velocity fluctuations camera 2 part 2 85
C.18 Disc 2; steady case velocity fluctuations camera 2 part 3 85
C.19 Disc 3; steady case velocity fluctuations camera 1 part 1 85
C.20 Disc 3; steady case velocity fluctuations camera 1 part 2 85
C.21 Disc 3; steady case velocity fluctuations camera 1 part 3 86
C.22 Disc 3; steady case velocity fluctuations camera 2 part 1 86
C.23 Disc 3; steady case velocity fluctuations camera 2 part 2 86
C.24 Disc 3; steady case velocity fluctuations camera 2 part 3 86
C.25 No disc; steady case convergence camera 1 86
C.26 No disc; steady case convergence camera 2 86
C.27 Disc 1; steady case convergence camera 1 86
C.28 Disc 1; steady case convergence camera 2 86
C.29 Disc 2; steady case convergence camera 1 87
C.30 Disc 2; steady case convergence camera 2 87
C.31 Disc 3; steady case convergence camera 1 87
C.32 Disc 3; steady case convergence camera 2 87

D.1 No disc; Dimensionless velocity versus y [D] at $x = -1D$; 5 degree amplitude; 6Hz . . . 90
D.2 No disc; Dimensionless turbulence intensity versus y [D] at $x = -1D$; 5 degree amplitude; 6Hz 90
D.3 No disc; Dimensionless velocity versus y [D] at $x = -1D$; 5 degree amplitude; 12Hz . . 90
D.4 No disc; Dimensionless turbulence intensity versus y [D] at $x = -1D$; 5 degree amplitude; 12Hz 90
D.5 No disc; Dimensionless velocity versus y [D] at $x = -1D$; 10 degree amplitude; 6Hz . . 90

D.6 No disc; Dimensionless turbulence intensity versus y [D] at $x = -1D$; 10 degree amplitude; 6Hz . . . 90
D.7 No disc; Dimensionless velocity versus y [D] at $x = 0.2D$; 5 degree amplitude; 6Hz . . . 91
D.8 No disc; Dimensionless turbulence intensity versus y [D] at $x = -0.2D$; 5 degree amplitude; 6Hz . . . 91
D.9 No disc; Dimensionless velocity versus y [D] at $x = 0.2D$; 5 degree amplitude; 12Hz . . . 91
D.10 No disc; Dimensionless turbulence intensity versus y [D] at $x = 0.2D$; 5 degree amplitude; 12Hz . . . 91
D.11 No disc; Dimensionless velocity versus y [D] at $x = 0.2D$; 10 degree amplitude; 6Hz . . . 91
D.12 No disc; Dimensionless turbulence intensity versus y [D] at $x = 0.2D$; 10 degree amplitude; 6Hz . . . 91

List of Tables

4.1 Test cases 32
4.2 PIV parameters 33

1
Introduction

On December 19, 2019, Frans Timmermans, vice-president of the European Commission, launched the European Green Deal [11]. In the next decades, Europe should reduce its emissions to stop climate change. Sustainable energy sources are required to replace fossil fuels. An example of a sustainable energy source is wind energy. Wind is a very old energy source. The first usage of wind energy was for the propulsion of boats along the river Nile [2]. Nowadays, wind energy could be used to reduce fossil fuels.

Wind turbines convert kinetic energy of the wind into electricity. The extraction of energy from the flow results in a lower velocity in the wake of the actuator disc. Wind turbines operate alone or in groups. If the wind turbines are in groups, the spatial distance between the wind turbines can result in different power extraction processes of the downstream wind turbine, due to the influence of wake losses caused by the upstream wind turbine.

Dynamic inflow conditions are the unsteady effects of wind turbine wake-induced velocity. Simulating dynamic inflow conditions in an experimental case is rather difficult. The gust may not be too strong, because then the dynamic inflow conditions could be so dominant that no measurements can be performed on the object itself. If the gust is too soft, the measurement results will be the same as for uniform inflow conditions. In the Aerospace Structures & Computational Mechanics department of the faculty of Aerospace Engineering of Delft's University of Technology, there is a possible solution. Dynamic inflow conditions can be simulated in a wind tunnel using a so-called gust vane generator. The gust vane generator consists of two symmetrical airfoils. The gust vane generator can be mounted in the faculty's so-called W-Tunnel wind tunnel.

1.1. Project overview

Actuator discs are commonly used to simulate wind turbines. Therefore, the actuator disc simplifies the numerical implementation of the flow field behind a so-called horizontal axis wind turbine. The momentum theory on which the actuator disc model based was first proposed by Froude in 1889 [14]. The method assumes an infinitely thin disc with uniform loading in a steady, inviscid, incompressible flow. In reality, wind turbines operate in highly unsteady flows caused by many reasons such as turbulence, gusts, wind shear, etc. One option is to use dynamic inflow conditions in numerical simulations. Other models use unsteady load conditions. In experimental work, a so-called active grid can be used. With an active grid, the flow in a wind turbine can be repeatedly disturbed in a controlled environment.

1.2. Project objective

In this master's thesis project, steps are taken to further extend the knowledge of dynamic inflow conditions on actuator discs. The main objective is to study the behavior of the wake behind the actuator disc under dynamic inflow conditions. Only a small number of studies have been dedicated to experimental work on wind turbines under dynamic inflow conditions. In order to extend the knowledge of this topic, an experimental approach is taken. Particle Image Velociymetry (PIV) is used as a flow measurement technique in order to study the flow field behind the actuator disc. Hereby, the actuator disc is modeled as a porous disc. The porosity of the actuator disc is used to compare the effect on the wake of the disc. The dynamic inflow conditions are generated by a gust generator with two symmetrical NACA airfoils. The gust is simulated in a sinusoidal way.

The following steps have been taken to realize this objective:

1. The first step is to review previous work related to the topic of interest. Work related to actuator disc theory, experimental work on dynamic inflow conditions, engineering models, etc. are reviewed.
2. The second step is experimental work to study the influence of dynamic inflow on the wake of the actuator disc. Hereby, several actuator discs with different porosities are used. The gusts are varied during the experiments.
3. The third step is post-processing of the captured images using DaVis software to estimate flow field characteristics. Besides the DaVis software, Matlab is used to compare various data sets.
4. The fourth step is to report all the results. Results from both steady and unsteady cases are discussed.

1.3. Report overview

The report is structured in five parts.

- **Background information**: Chapter 2 and chapter 3 introduce the theory behind the actuator disc model, and aerodynamics of the wind turbine wake. Besides some state-of-the-art models are presented.
- **Methodology**: In chapter 4, the experimental set-up is explained.
- **Results**: The steady state cases are analysed in chapter 5. Chapter 6 is about the analysis of the unsteady cases..
- **Uncertainty**: An uncertainty estimation of the results is given in chapter 7.
- **Conclusion and recommendations**: Finnaly, the report ends with conclusion from all the results and recommendations for further research. The conclusion can be read in chapter 8
- **Appendices**: Appendix A gives an overview of the non-dimensional velocity versus y for several x-locations in the domain. In appendix B, the gusts of the steady cases are shown. Appendix C shows the velocity fluctuations of the steady cases, and the convergence of the steady cases. Appendix D analyses the velocity profile and turbulent intensity at specific planes in the wake, and compares it to the steady cases.

2
Background

This chapter describes the analysis methods for wind turbines. The main analysis method in this report is the actuator disc theory (see section 2.1). For unsteady conditions, dynamic inflow conditions could be used (see section 2.2). The wake of the wind turbine is discussed in section 2.3. The fourth section (section 2.4) is about some flow phenomena around actuator discs. The last section is about Particle Image Velocimetry (see section 2.5).

2.1. Actuator Disc model

This section describes the actuator disc model. The Actuator Disc (AD) model is a well-known and often used model to analyze a wind turbine. The model avoids scaling issues and simplifies the simulation. The model has been studied in numerous cases for steady loading. In this subsection the theory and the assumptions of relevance are discussed in sections 2.1.1 and 2.1.2.

2.1.1. Actuator disc model

In the Actuator Disc model, the wind turbine rotor is modeled as a disc. The disc is assumed to be ideal, which means that the disc is frictionless. Therefore, there is no rotational velocity in the wake of the disc. Furthermore, the disc is assumed to be a wind turbine with an infinite number of blades where the loads act uniformly on the disc [18].

Further assumptions in the actuator disc model are:

- Incompressibility and frictionless flow with no external forces. Normally, the operating tip speed of a wind turbine is around 80m/s, which means that the flow can be assumed to be incompressible.
- Another assumption in the actuator disc model is inviscid flow.
- Also, the actuator disc model is a 1D model. However, in reality, wind turbines operate in yawed conditions due to various wind directions and/or upstream wind turbines.
- The last assumption for the actuator disc model is stationary flow. The flow in the wake changes immediately if the inflow condition is changed.

A wind turbine extracts energy from the air flow. This means that the velocity far upstream of the rotor is higher than the velocity at the rotor itself, and the velocity far downstream is again lower than the velocity at the rotor. The velocities at the specific location are defined by the following symbols: U_∞ is the velocity far upstream; u is the velocity at the disc, and u_1 is the velocity far downstream.

The mass flow rate is defined as:

$$\dot{m} = \rho A U_\infty \tag{2.1}$$

where ρ is the density, A is the area, and U_∞ is the velocity. The density is assumed to be constant. From this assumption, the mass flow rate should also be constant. The area far upstream is smaller than the area at the disc. Also, the area far downstream is larger than the area on the disc. Thus, the streamlines must diverge as shown in figure 2.1.

The drag of the disk model is also obtained by a pressure drop over the rotor. Far upstream, the pressure is at atmospheric conditions indicated by the symbol p_o. Closer to the disk, the pressure rises to a higher pressure. A discontinuous pressure drop of Δp over the disk occurs before the pressure recovers to atmospheric level downstream of the disk. A force in the streamwise direction, the thrust, can be defined as:

$$T = \Delta p A \tag{2.2}$$

where A is the area of the disc and defined as:

$$A = \pi R^2 \tag{2.3}$$

As already mentioned, the flow is assumed to be stationary, incompressible, frictionless, and experiences no external forces on the fluid. Therefore, Bernoulli's equation is valid from far upstream to just in front of the disk and from just behind the disk to far downstream.

$$p_o + \frac{1}{2}\rho U_\infty^2 = p + \frac{1}{2}\rho u^2 \tag{2.4}$$

$$p_o + \frac{1}{2}\rho u_1^2 = p - \Delta p + \frac{1}{2}\rho u^2 \tag{2.5}$$

Combining the two equations (2.4 and 2.5) yields:

$$\Delta p = \frac{1}{2}\rho \left(U_\infty^2 - u_1^2\right) \tag{2.6}$$

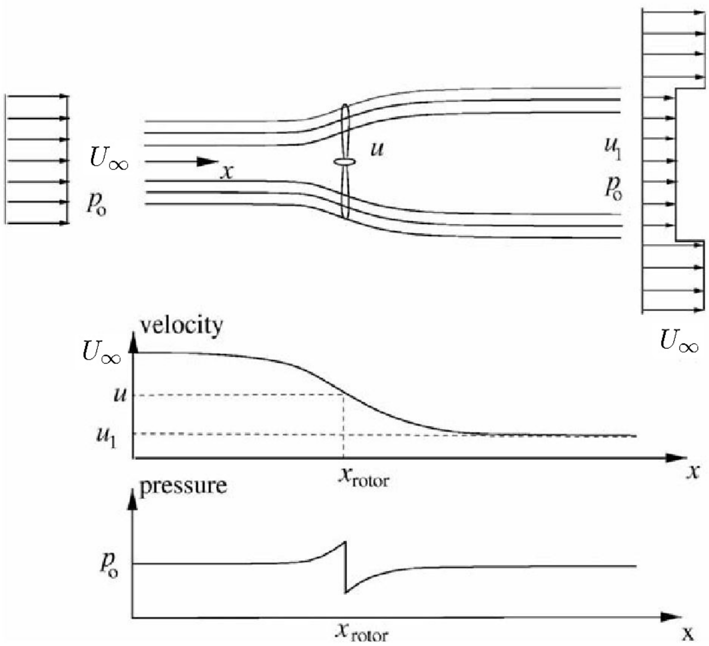

Figure 2.1: Streamlines, axial velocity and pressure [18]

Using the control volume in figure 2.2, the axial momentum equation could be written as:

$$\frac{\delta}{\delta t}\iiint_{cv} \rho u\left(x,y,z\right)\, dx\, dy\, dy + \iint_{cv} u\left(x,y,z\right)\rho V \dot{d}A = F_{ext} + F_{pres} \tag{2.7}$$

The first term is equal to zero, because the assumption is made of a stationary flow. The last term is zero, because the pressure is equal on both end plates and the area is equal. The force on the lateral boundary has no lateral component. Using the assumption for an ideal rotor, the equation (2.7) becomes:

$$-T = \rho u_1^2 A_1 + \rho U_\infty^2 \left(A_{CV,in} - A_1\right) - \rho U_\infty^2 A_{CV,in} + \dot{m}_{side} U_\infty \tag{2.8}$$

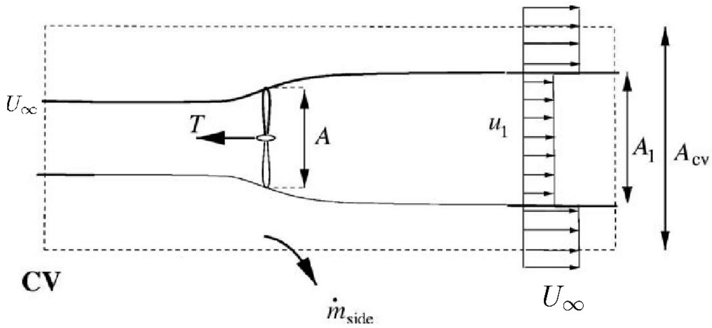

Figure 2.2: Rectangular control volume [18]

Both m_{side} and the relation between A_1 and A can be found from the conservation of mass:

$$\rho u_1 A_1 + \rho U_\infty \left(A_{CV,in} - A_1\right) - \rho U_\infty A_{CV,in} + \dot{m}_{side} = 0 \rightarrow \dot{m}_{side} = \rho A_1 \left(U_\infty - u_1\right) \tag{2.9}$$

$$\dot{m} = \rho u_1 A_1 = \rho u A \tag{2.10}$$

Combining the equations:

$$T = \rho u A \left(U_\infty - u_1\right) = \dot{m} \left(U_\infty - u_1\right) A \tag{2.11}$$

Using equations (2.6, 2.10 and 2.11) leads to:

$$U = \frac{1}{2} \left(U_\infty - u_1\right) \tag{2.12}$$

The velocity on the disk is the mean of the freestream velocity and the final value of the velocity in the wake. The shaft power P can be found from the integral energy equation using the control volume (below) of figure 2.3.

$$P = \dot{m}(\frac{1}{2} U_\infty^2) + \frac{p_o}{p} - \frac{1}{2} u_1^2 - \frac{p_o}{p} \tag{2.13}$$

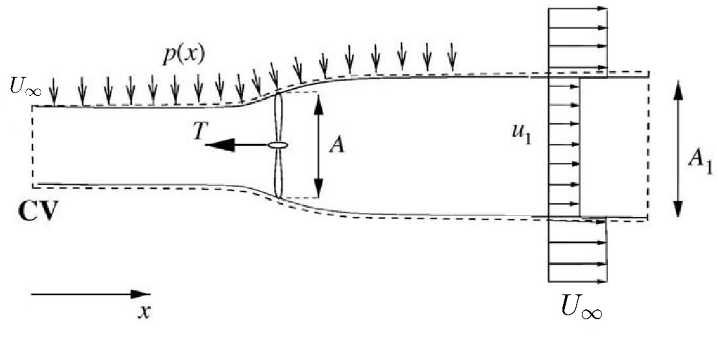

Figure 2.3: Alternative control volume [18]

Expressions can be determined by the power (equation 2.18) and thrust (equation 2.19) of a wind turbine by defining equations 2.14, 2.15, 2.16, and 2.17.

$$P = \frac{1}{2} \rho u A \left(U_\infty^2 - u_1^2\right) \tag{2.14}$$

$$u = (1 - a)\, U_\infty \tag{2.15}$$

$$u_1 = (1 - 2a)\, U_\infty \tag{2.16}$$

$$T = \rho u A \left(U_\infty - u_1\right) \tag{2.17}$$

$$P = 2\rho U_\infty^3 A \left(1 - a\right)^2 \tag{2.18}$$

$$T = 2\rho U_\infty^2 A \left(1 - a\right)^2 \tag{2.19}$$

The available power in the area of the disc is:

$$P_{avail} = \frac{1}{2} \rho A U_\infty^3 \tag{2.20}$$

Both the power and the thrust could be made dimensionless:

$$C_P = \frac{P_{avail}}{\left(\frac{1}{2}\rho A U_\infty^3\right)} \tag{2.21}$$

$$C_T = \frac{T}{\left(\frac{1}{2}\rho A U_\infty^2\right)} \tag{2.22}$$

Both coefficients could be rewritten into a relation with the induction factor:

$$C_P = 4a \left(1 - a\right)^2 \tag{2.23}$$

$$C_T = 4a \left(1 - a\right) \tag{2.24}$$

The maximum C_P can be analyzed by differentiating the formula of the pressure coefficient (equation 2.23) with respect to a.

$$\frac{C_P}{da} = a \left(1 - a\right) \left(1 - 3a\right) \tag{2.25}$$

It can be analysed that the maximum C_P is equal to $\frac{16}{27}$ for $a = \frac{1}{3}$. This theoretical maximum for an ideal wind turbine is known as the Betz limit. This limit is visible in figure 2.4.

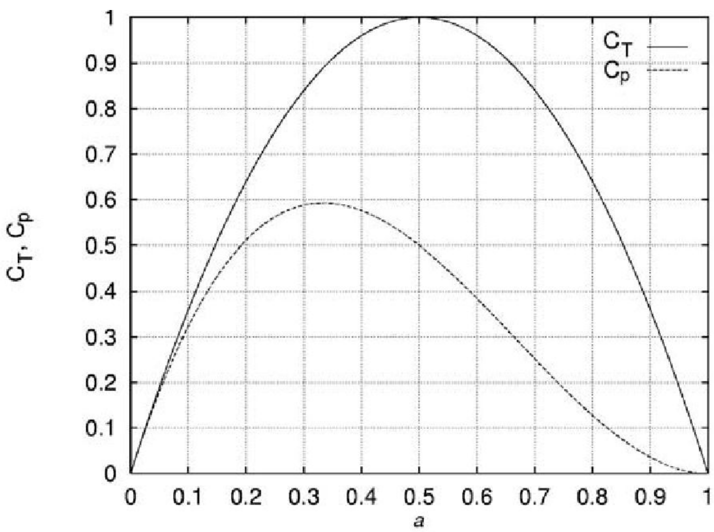

Figure 2.4: Thrust and power coefficients with respect to axial induction factor [18]

2.1.2. The assumptions in Momentum theory

Various assumptions were made in the Actuator Disc model.

- A disc with uniform loading is used to model a wind turbine. In reality, the loading is not uniform. Therefore, the Prandtl's tip correction factor is applied in Blade Element Momentum Theory (BEM).
- Corrections should be made to compensate for the incompressibility and inviscid flow. The corrections could be on the airfoil characteristics for the actual Mach number or the Prandtl-Glauert correction. However, mostly the corrections are neglected, because the tip speed is generally around 80m/s and therefore the Mach number is below 0.3.
- Another assumption for the Actuator Disc model is stationary. In normal operational conditions, in the wake, shed vorticity occurs together with trailing vorticity. Shed vorticity is, for example, the unsteadiness of the bound vortex. Trailing vorticity relates to the spanwise variation of the bound vortex [47].
- One of the reasons that the power generated by the wind turbine is often less than the Betz limit is that viscous effects are neglected in momentum theory. The momentum theory is based on a simplified streamtube concept. Various effects are neglected. Moreover, there is a discontinuity in the pressure and velocity at the disc edge. From an experiment by J.G. Schepers [47], it is known that near the wake, the streamtube concept is almost right.

2.2. Dynamic inflow

Dynamic inflow describes the unsteady effect of wind turbine wake-induced velocity. The wake-induced velocity is influenced by variations in wind turbine rotor load. These variations in wind turbine load come from changes in blade pitch angle or wind gusts. The flow requires a response, which indicates that the flow is not always in equilibrium. An example is a sudden change in blade pitch angle; this causes an overshoot in angle of attack which results in an overshoot in loading on the blade. This means a steady state is reached after a short-time delay [51].

H. Snel [51] and J.G. Schepers [47] state that the dynamic inflow phenomenon can also be explained using the change in vorticity. A trailing vortex is formed at the blade and moves downstream with the flow. A change in pitch angle changes the bound vortex. The trailed vortex is moving at a finite velocity; the "new" and "old" vortices are mixed. Consequently, the induced velocity was influenced by both vortices (see figure 2.5).

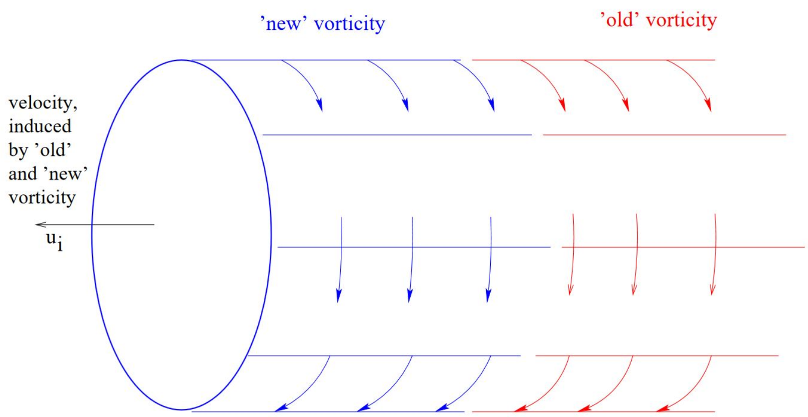

Figure 2.5: Wake mixing [47]

As stated above, the assumption of stationary conditions and instantaneous responses in momentum theory is not entirely true. It takes some time before a new equilibrium state is reached. Investigations have been done into dynamic inflow conditions, such as the research of H. Snel [51] and J.G. Schepers and H. Snel [17]. Several models have been investigated to simulate dynamic inflow [51]. In the experiments, the effects of changes in blade root flapping movement, root shaft torque, and blade pitch angle were analyzed. The first effect is that a change in blade pitch angle results in a change in angle of attack which results in a change in torque. This effect is due to unsteady airfoil aerodynamics. The second effect is the change in torque due to the new equilibrium state of the induced velocity. If the induced velocity is larger than the axial velocity, the torque decreases, and the first effect also decreases.

2.2.1. Modelling dynamic inflow

Several models have been developed for dynamic inflow conditions behind an unsteady actuator disc. Blade Element Momentum (BEM) theory gives good results in uniform load conditions; it assumes the equilibrium assumptions of the momentum theory. Two of these models are the Stig Øye dynamic inflow model and the Pit-Peters-type dynamic inflow model. These two models were analyzed in a study by J. De Vaal [53]. In this simulation, the effect of wind turbine surge motion is investigated on rotor thrust and induced velocity. The conclusion is that all methods are close on thrust, but that the induced velocity has large differences between the models.

A third dynamic inflow model is the ECN model. The ECN model is developed by Energieonderzoek Centrum Nederland (ECN), nowadays part of the Nederlandse Organisatie voor toegepast-natuurwetenschappelijk onderzoek (TNO).

2.2.2. Stig Øye dynamic inflow model

The Stig Øye model calculates the induced velocity using a quasi-steady induced velocity in two first-order linear differential equations [35]. The induced velocity is given by the following formula:

$$V_{int} + \tau_1 \frac{dV_{int}}{dt} = V_{qs} + k\tau_1 \frac{dV_{qs}}{dt} \tag{2.26}$$

$$V + \tau_2 \frac{dV_{int}}{dt} = V_{int} \tag{2.27}$$

where V_{qs} is the quasi-steady velocity, V_{int} is the intermediate value of the induced velocity and V is the induced velocity. For vortex rings, $k = 0.6$. τ_1 and τ_2 are determined by the following two formulas in which r is the radial distance and R is the rotor radius:

$$\tau_1 = \frac{1.1}{1 - 1.3a} \frac{R}{V_o} \tag{2.28}$$

$$\tau_2 = \left[0.39 - 0.26 \left(\frac{r}{R}\right)^2\right] \tau_1 \tag{2.29}$$

As the formulas for the induced velocities are first-order ordinary differential equations, they could be solved using a central, forward or backward differentiation method. For the forward and central differentiation methods, information of the next time step is required and, therefore, it is more time-consuming than the backward differentiation method.

The time derivatives using backward difference method are shown below:

$$\frac{dV_{qs}}{dt} = \frac{V_{qs}^1 - V_{qs}^{i-1}}{\Delta t} \tag{2.30}$$

$$\frac{dV_{int}}{dt} = \frac{V_{int}^1 - V_{int}^{i-1}}{\Delta t} \tag{2.31}$$

$$\frac{dV}{dt} = \frac{V^i - V^{i-1}}{\Delta t} \tag{2.32}$$

Substituting these into the equations gives:

$$V_{int}^i + \tau_1 \frac{V_{int}^1 - V_{int}^{i-1}}{\Delta t} = V_{qs}^i + k\tau_1 \frac{V_{qs}^1 - V_{qs}^{i-1}}{\Delta t} \tag{2.33}$$

$$V^i + \tau_2 \frac{V_{int}^1 - V_{int}^{i-1}}{\Delta t} = V_{int} \tag{2.34}$$

Both equations above can be rewritten into

$$V_{int}^i = \frac{V_{qs}^i + k\tau_1 \frac{V_{qs}^1 - V_{qs}^{i-1}}{\Delta t} + \frac{V_{int}^{i-1}}{\Delta t}}{1 + \frac{\tau_1}{\Delta t}} \tag{2.35}$$

$$V^i = \frac{V_{int} + \frac{V^{i-1}}{\Delta t}}{1 + \frac{\tau_2}{\Delta t}} \tag{2.36}$$

2.2.3. Pitt-Peters dynamic inflow model

The model was developed by Pitt and Peters and introduced at the Ninth European Rotorcraft forum [41]. The model was also presented in a research of H. Snel and J.G. Schepers [17]. The model is based on the actuator disc model. The Pitt-Peters model allows for radial variations of the force and induced velocity and is therefore considered to be more realistic. J. de Vall [53] describes the thrust of the rotor with the following formula:

$$T = \frac{8}{3\pi} \rho A_k r_k \frac{dV_{i,k}}{dt} + 2\rho A_k V_{i,k} V_{z,k} \tag{2.37}$$

Where the rotor is divided into k independent annular rings, $V_{i,k}$ is the induced velocity, $V_{z,k}$ is the axial velocity in annulus ring k which is located at radius r with an area A_k. Also, this model can be evaluated using a backward difference method.

$$T = Dynamic\ term + Steady\ term = \frac{8}{3\pi} \rho A r \frac{W^i - W^{i-1}}{\Delta t} + 2\rho A W^i V_\infty^i \tag{2.38}$$

Rewriting this equation leads to the following expression:

$$W^i = \frac{1}{2} \left[V_o + \frac{4r}{3\pi\Delta t} - \sqrt{\left(\frac{4r}{3\pi\Delta t} + V_o \right)^2 - \frac{16r}{e\pi\Delta t} W^{i-1} - C_{T,qs} V_o^2} \right] \tag{2.39}$$

2.2.4. ECN dynamic inflow model

The engineering model for dynamic inflow, which was developed by ECN, is used in the PHATAS program [17]. PHATAS, which stands for Program for Horizontal Axis wind Turbine Analysis and Simulation, is an aero-elastic code developed by ECN. The model is based on Blade Element Momentum Theory. The model has a structural model and has various generator and control models. The wind field can be prescribed by a constant and/or uniform wind speed with or without yaw misalignment and wind shear.

The engineering dynamic inflow model is derived from an integral relationship. The relationship is extracted from the simplified cylindrical vortex wake sheet model. If the situation is not in equilibrium, a time-dependent integral relation is used. The wind speed is constant and can be written as a first order differential equation in time:

$$\frac{R}{V_w} f_a \frac{da}{dt} + a\,(1-a) = \frac{C_{tj}}{4} \tag{2.40}$$

Where C_{tj} is the axial force coefficient on the rotor annulus j. The term f_a is a function of the radial position.

$$f_a = \frac{2\pi}{\int_0^{2\pi} \frac{[1-(r/R)\cos(\Phi_r)]}{[1+(r/R)^2 - 2(r/R)\cos(\Phi_r)]^3/2} d\Phi_r} \tag{2.41}$$

2.3. The wake of the wind turbine

The wake of a wind turbine is highly complex. The area is influenced by various factors, such as operating conditions and the number of blades. The wind turbine extracts energy from the incoming air flow, which indicates that the wake downstream of it has a lower momentum and velocity. After a certain point, the wakes start to recover back to freestream conditions. This process depends on turbulent eddies and shear layers in the wake. The wake of the wind turbine can be divided into two parts, a near wake region and a far wake region [46] [23]. Figure 2.6 gives an indication of the near and far wake behind the rotor. The near wake is discussed in subsection 2.3.1 and the far wake is discussed in subsection 2.3.2.

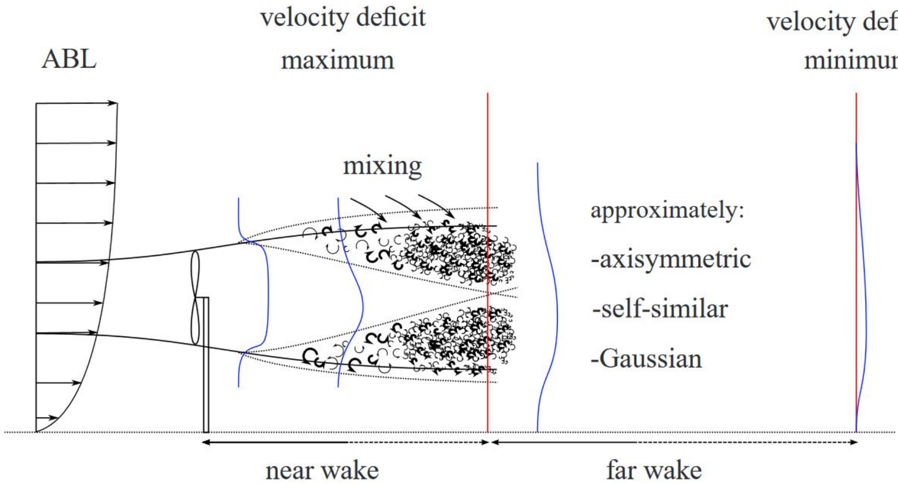

Figure 2.6: Wake of wind turbine [46]

2.3.1. Near wake

The near wake region is the region just behind the wind turbine. The length of the near wake region depends on various parameters such as the blade geometry, and the operating conditions. However, the standard definition for the length of the near wake is the point where the shear layer expansion touches the turbine axis.

Normally, the near wake length is 1-2 rotor diameters [3], but it can extend up to 10 rotor diameters [36]. According to C. Ferreira et al. [13] the wake has expanded over 90% of its expansion at one rotor diameter. Besides shear layer expansion, the tip vortex is the second phenomenon in the near wake region. Like 3D wing aerodynamics, a bound and tip vorticity formation exists due to the difference in loading along the span and the difference in pressure on both sides. The pressure on the pressure side of the airfoil is higher than the pressure on the suction side of the airfoil. However, in the wake of a wind turbine it is even more complex due to rotational effects. Due to blade rotation, a helical structured tip vortex occurs.

At the boundary of the wake, high velocity gradients occur due to the large velocity difference inside and outside the wake. The velocity inside the wake is reduced by energy extraction from the rotor. The wake is receiving energy to return to its original, freestream, state. This re-energization is through mixing. The mixing happens in two ways; mixing due to atmospheric turbulence and wake-induced mixing (see figure 2.7). The wake-induced mixing has hereby a certain interest because the tip vorticity, its instability and its breakdown play a major role in this process. The atmospheric conditions play a large role in onshore wind farms and less in offshore wind farms [26].

Wake-induced mixing is due to the helical structure of the tip, its instability, and its breakdown. As already mentioned, a bound and tip vortex is formed due to higher pressure on the pressure side and a lower pressure on the suction side of the airfoil. Due to rotation, a helical structure downstream of the rotor occurs. The tip vortices decrease in size as there is vortex shedding. As the wake expands, the tip vortices are pushed outwards in a radial direction. After this, the vortices increased due to viscous effects before they, in the end, broke down.

At different azimuthal angles, the tip vortices are shed. A so-called tubular vortex sheet is formed when the rotational speed of the wind turbine is increased, because the tip vortices are formed closer together. The same effect occurs if the number of blades is increased [23].

Wind turbines operate in ambient turbulence and wind shear due to the ground effect. According to V. Hong [21], for lower ambient turbulence the shear layer would be almost stable over a longer distance. This means that there are larger velocity deficits in the wake and, therefore, there is less turbulence in the flow to induce momentum mixing.

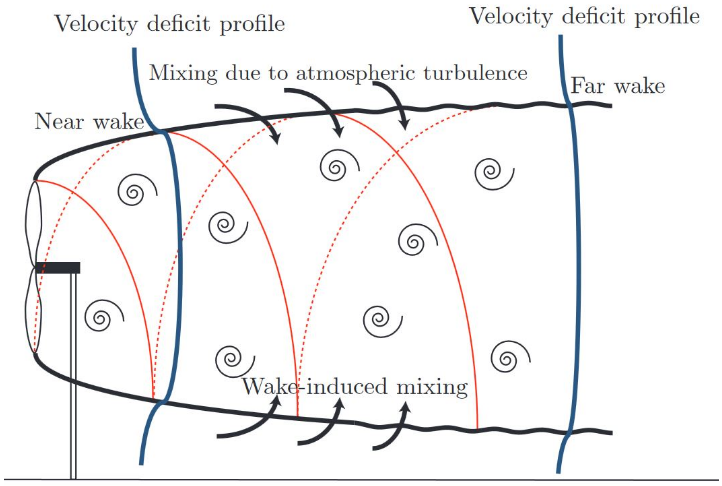

Figure 2.7: Wake of wind turbine [26]

The term momentum mixing stands for the following. A study of the vorticity of a wind turbine wake was made by L. Lignarolo [31] using Stereoscopic Particle Image Velocimetry. Vortex pairing or leap-frogging phenomena were the result of this investigation. The phenomenon, where the vortex catches up with the others. This shows that instabilities play an important role in the diffusion of the shear layer. According to Task 30 of the International Energy Agency [1] the vortex pairing happens due to flow perturbations. These perturbations are caused by ambient turbulence and different blade pitch settings. Depending on the rotor velocity, vortex pairing occurs earlier or later.

2.3.2. Far wake

In the far wake, the flow starts recovering back towards freestream conditions. The far wake is assumed to be fully developed and therefore, there are no more velocity deficits. The exact length is hard to define, but C. Ferreira et al. [13] defines the far wake at five rotor diameters. This length accounts for 99% of the induction on the actuator disc.

The shear layer is diffused due to momentum mixing and leapfrogging; the velocity field starts recovering. This happens mainly by atmospheric turbulence and wake-induced mixing. The pressure and velocity gradients are less important [46] and the focus is more on the velocity profiles. The wake is generally assumed to be axisymmetric, i.e. $\frac{dp}{dx}$ and $\frac{d^2u^2}{dx^2} = 0$. Furthermore, it can be assumed that the velocity profile and turbulence intensities are self-similar. A note should be made, because it is not exactly true, as there is still the presence of ambient shear due to the ground effect.

2.4. Flow phenomena

This section introduces some flow phenomena of actuator discs and/or wind turbines. In subsection 2.4.1, the so-called vortex ring system is discussed. Subsection 2.4.2 is about wake meandering.

2.4.1. Vortex ring system

A special flow phenomenon in the wake of a wind turbine or actuator disc is the so-called vortex ring system.

At every azimuthal angle, the blade tip produces a vortex. Due to wind turbine rotation, the position of the vortex production travels along with the rotating blade. Besides the wind turbine rotation, the downstream movement of the flow ensures that the tip vortex is rotating and moving downstream. A so-called helical vortex ring arises. An example of a helical vortex structure is visible in figure 2.8.

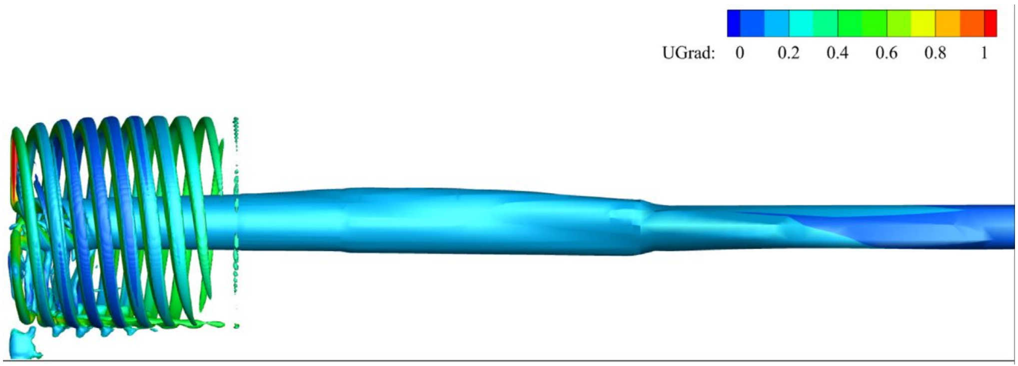

Figure 2.8: Side view of a vortex ring [4]

2.4.2. Wake meandering

This subsection describes another flow phenomenon in the wake of actuator discs, namely wake meandering.

Wake meandering is the oscillation of the wake behind the actuator disc. This phenomenon can happen due to a yawed inflow condition. The yawed inflow condition leads to a periodic variation of angle of attack on the wind turbine blade. This variation leads to load fluctuations [21]. In figure 2.9 wake meandering is visible in the top part of the figure.

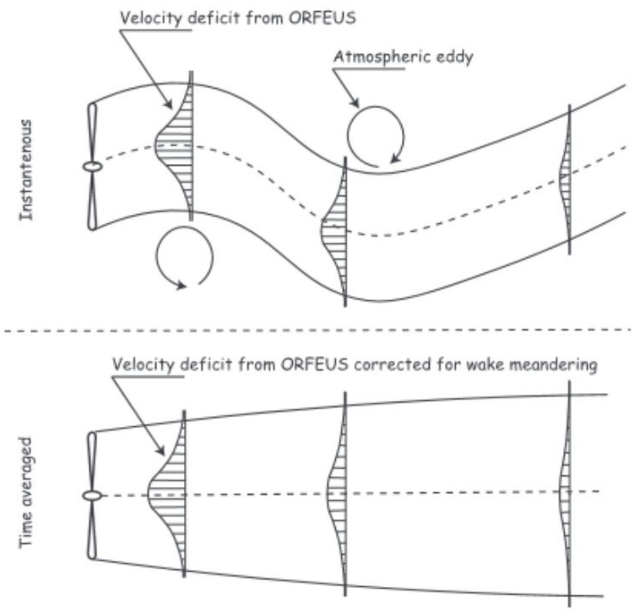

Figure 2.9: Wake of a wind turbine [9]

Zhoabin Li et al. [30] investigated both uniform inflow conditions and full turbulent inflow conditions. In figure 2.10, the result of the full turbulent inflow is visible. Wake meandering is visible. In the figure, the wake first moves a bit down before it moves a bit up.

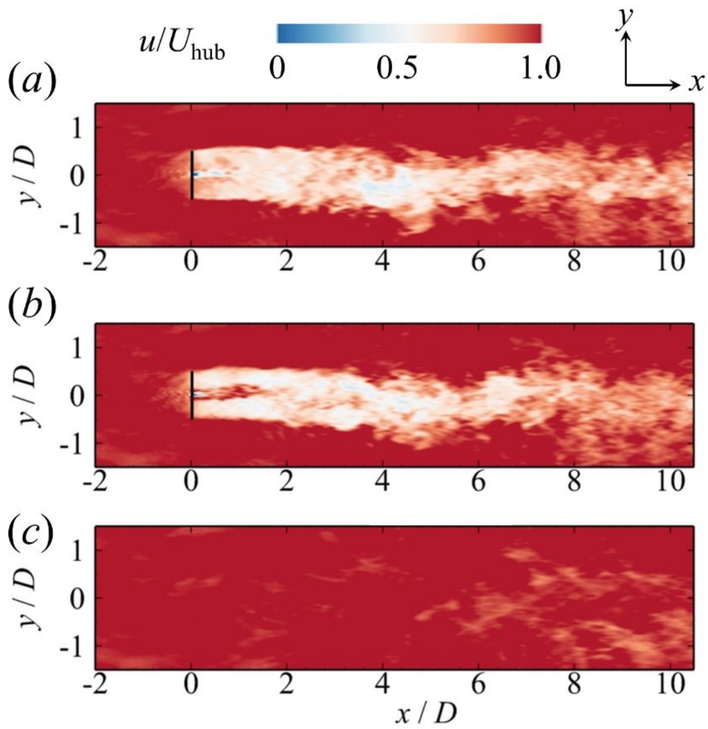

Figure 2.10: Turbulent inflow: contours of the instantaneous velocity field behind the wind turbine on the horizontal plane at hub height. (a) streamwise velocity using AD; (b) streamwise velocity using AS; The solid black line at x = 0 illustrates the location and the diameter of the wind turbine; (c) streamwise velocity of the turbulent inflow without wind turbine [30]

2.5. Particle Image Velocimetry

In this section, Particle Image Velocimetry is introduced. Particle Image Velocimetry (PIV) is an optical method of flow visualization. The method is used both for education and research. Two advantages of PIV are:

- PIV is a non-intrusive method; in other words, the method does not immerse itself in the flow.
- The other advantage is that a whole flow field is captured. Besides, depending on the type of PIV, the flow field could be captured both two-dimensional and three-dimensional. In this report, a two-dimensional analysis is used in combination with the assumption of axisymmetric flow.

PIV also has some disadvantages.

- It is difficult to setup due to complexity.
- The particle size is important such that the particles only follow the flow and not change the flow.
- The amount of particles is important, because for a very low number of particles the flow field is not captured correctly. If there are too many particles, the flow field can not be analysed due to overlapping particles.
- Post-processing is time-consuming.

PIV determines the velocity field using particles carried by the fluid over a short time interval. Hereby, it is assumed that the particles follow the flow dynamics. However, the particles should be small enough to not disturb the flow and the particles should be able to scatter light. This scattered light is captured by a camera. The camera is placed perpendicular to the measurement plane [44]. Figure 2.11 shows an example of an PIV set-up.

As already mentioned, the particles should be able to scatter light. Therefore, a light source is required. In Particle Image Velocimetry, lasers are the most commonly used light sources. Lasers are able to omit high intensity monochromatic light. The laser sheets should be thin so that only the particles in the measurement field are captured by the cameras. For the optimal thickness of the laser sheet, optics is used. Besides, the pulse time, or in other words, the duration of the illumination should be such that the particles are dots in the images and not lines. The light source should be able to illuminate the flow field twice by separation in a short time, the separation time.

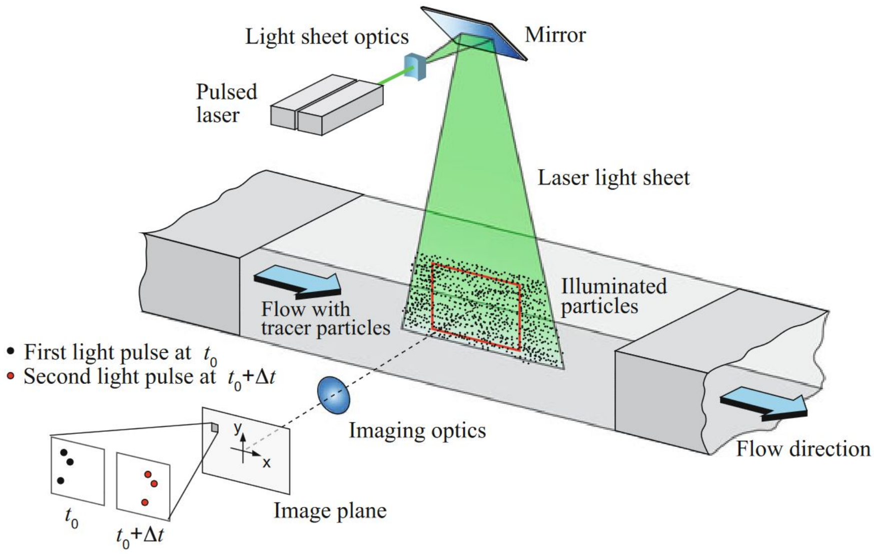

Figure 2.11: Experimental arrangement of PIV in a wind tunnel [44]

Cross-correlation is the similarities between two separate measurements. The cross-correlation value is found and placed where the average displacement of the particles in a specific window. This process is done for every interrogated window. Ideally, the windows should overlap, because the particles at the edges might have moved out of the window in two different frames.

3

Experimental and numerical work on Actuator Discs

Chapter 2 was about the Actuator Disc model; Dynamic inflow conditions, and the description of the wake of an actuator disc. This chapter introduces state-of-the-art numerical (see section 3.1) and experimental (see section 3.2) work. The last section is about actuator disc design for experimental work (see section 3.3).

3.1. Numerical work dynamic inflow conditions

This section describes numerical work of actuator discs under dynamic inflow conditions.

C. Ferreira et al. [13] tried to derive and apply dynamic inflow conditions as a correction for the effect of surge motion on the estimation of the induction on the actuator disc. Therefore, the Blade Element Momentum theory should not break down. The vorticity-velocity system uses a linear superposition of a previously released wake and a newly released wake, related to a reduced timestep.

W. Yu et al [59] derived a new dynamic inflow model for the time scale of dynamic induction using vortex models. A model for both a linear actuator disc vortex model and a nonlinear actuator disc vortex model have been proposed. The linear model predicts results close to the Øye dynamic inflow model. The nonlinear model predicts results better than all engineering models (Øye, Pitt-Peters, and the ECN model (see section 2.2). Especially at higher thrust, the results for phase delay and amplitude are better.

W. Yu et al. [58] compared the well-known dynamic inflow models of Øye, Pitt-Peters and the ECN model to numerical and experimental methods. The dynamic inflow models of Øye, Pitt-Peters and the ECN model have a much faster decay of induction. The decay of induction is also much faster than in the experiments. Therefore, a more advanced engineering inflow model is required for flow prediction. From this, the following can be concluded. If new models are proposed, a model should not only be compared to engineering models of Øye, Pitt-Peters, and the ECN model, but also to experiments.

In another experimental analysis into the dynamic wake of an actuator disc, W. Yu et al. [57] concluded that both the local turbulence intensity and the convection velocity of the wake are key factors to determine the total transient time from one steady state to another steady state.

A simple vortex model is compared to the unsteady NADA Ames Phase VI experiments and corresponding high-fidelity simulations. The main research question of G. Raimund Pirrung and H. Aagaard Madsen [43] is why both methods (the simple vortex model and the unsteady NADA Ames Phase VI experiments) do not show the expected radial dependence of the dynamic inflow time constant.

Initially, the results showed strong radial dependence, but a short time step after, the time constants for the different stations became similar. This suggests that the two time constants are necessary for accurate modelling of dynamic inflow effects. The time constants can only be analysed shortly after the pitch step when the forces are decaying. However, this delays the analysis of fast induction development, which can lead to decreased or reversed radial dependence. Thus, it is difficult to obtain time constants for dynamic inflow models based only on force time series.

Huilan Ren et al. [45] did a CFD simulation of the wind turbine wake. The k-ϵ-model was used. The main observation in the simulation is the necessity of the source term in the k-ϵ-model. If the source term is added to the model, the coordination of the generation and dissipation of turbulent kinetic energy is better. Therefore, the prediction of the wake distribution is better.

3.2. Experimental work dynamic inflow conditions

In comparison to the previous section (section 3.1), this section is about experimental work on actuator discs under dynamic inflow conditions. First, an active grid is discussed (see subsection 3.2.1). Subsection 3.2.2 is about experimental work done with an active grid.

3.2.1. Active grid

Since wind tunnels are designed to have uniform flow in the test section, a so-called active grid was designed to have repeatable dynamic inflow conditions in a wind tunnel.

The design of active grids started in 1991 by H. Makita [33]. An active grid manufactured from fifteen vertically and horizontally oscillating rods with many attached wings. Each rod is independently driven by a stepping motor. The stepping motors are mounted outside the wind tunnel test section (see figure 3.1).

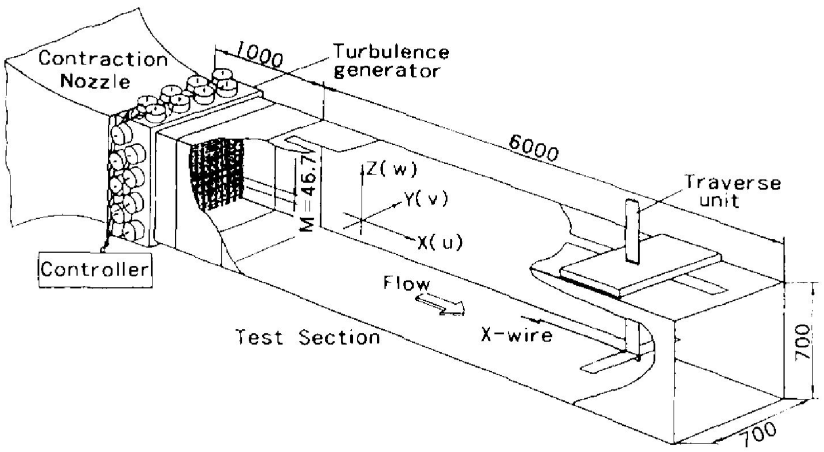

Figure 3.1: Experimental set up, units in mm. [33]

In comparison to H. Makita [33]., P. Knebel et al. [24] used a slightly different grid. The active grid of P. Knebel et al. consists of nine vertically and seven horizontally rotatable axes with 10 x 10 cm square-shaped aluminum vanes. Each axis can be rotated independently. This active grid is rather popular. Similar grids were used by Qing'an Li et al. [28]; L. Neuhaus et al.[39], and R. J. Hearst et al. [19].

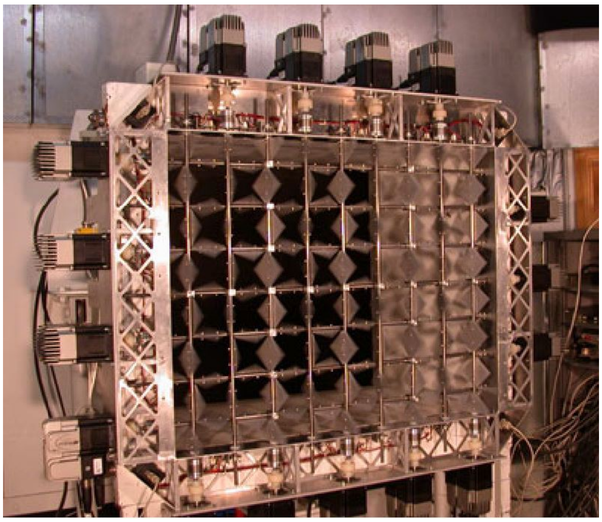

Figure 3.2: Active grid [24]

In comparison to the grid of H. Makita [33], T. T. B. Wester used only vertically placed rods in the two designed active grids. The two active grids are different in size and were used for the experimental analysis of an airfoil. The two active grids have several configurations. The first configuration consists of 9 vertical shafts, which were $S_{shaft} = 800mm$ and $g_{shaft} = 110mm$ (see figure 3.3). The shafts are controlled by their own stepper motor. In the analysis of the best 2D active grid, three different shaft types were analysed. The first shaft type is a flat plate with a chord length of 90mm and a thickness of 5mm. The other two types are symmetrical NACA airfoils. The second shaft type is a NACA0018 airfoil with a chord length of 71mm, while the third shaft type is a NACA0009 airfoil with a chord length of 180mm. In figure 3.5, the three different shafts are shown.

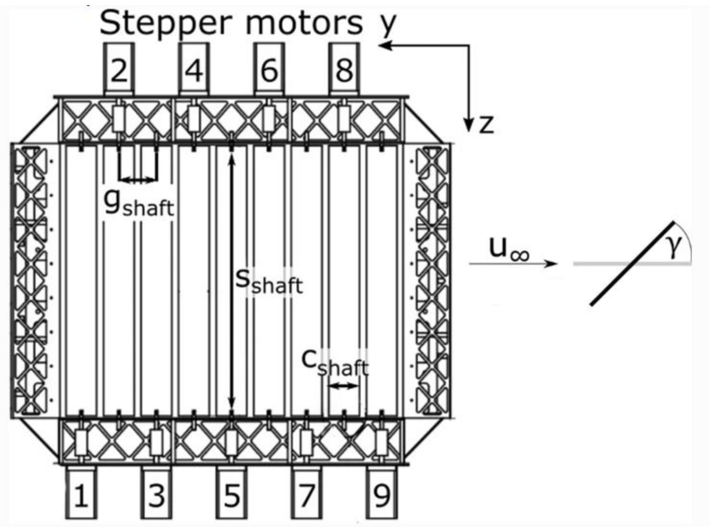

Figure 3.3: Technical drawing of the 2D active grid containing the stepper motors (1–9), the gauge of the shafts gshaft, the span of the shafts sshaft and the chord length of the shafts cshaft. At the right side, the definition of shaft angle γ is shown (top view onto the shaft) [25]

Besides, the analysis of different shaft types, also the number of shafts in the wind tunnel was analysed. The first configuration has all nine shafts in use; the second configuration has the three middle shafts removed. In this second configuration, only the NACA0018 shafts were used. The final configuration is with only two shaft positions, where the shaft type of the NACA0009 airfoil is used. In figure 3.4, the different active grids are shown.

As already mentioned, two different 2D active grids were used. The second active grid is a smaller replica of the first active grid. The second active grid fits into a 0.25m x 0.25m wind tunnel. In comparison to the previous grid, this grid has only five shafts. The following dimensions are used: $g_{shaft} = 50mm$ and $s_{shaft} = 245mm$.

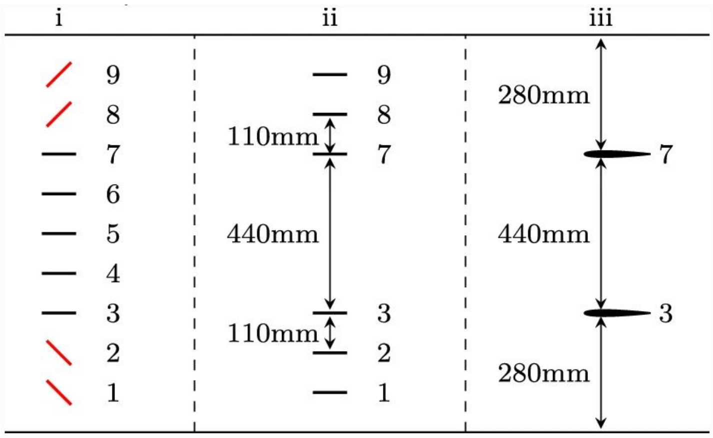

Figure 3.4: Shafts for the 2D active grid. I: Flat plates with a chord length of 90 mm. II: NACA0018 airfoils with a chord length of 71 mm. III: NACA0009 with a chord length of 180 mm. The red mark indicates the pivot point. [25]

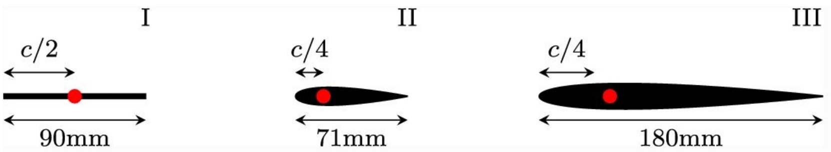

Figure 3.5: Shaft setups of the 2D active grid as top view on the shafts. i shows a setup with nine shafts, ii uses six shafts and in iii only two shafts of type NACA0009 are installed. [25]

The main conclusion of the analysis of the best active grid is that for longitudinal gusts, only the blockage is decisive for the gust amplitude. Regarding the transversal gusts, various conclusions can be drawn. The position of the shafts is crucial for the transversal gust amplitude. For large amplitude, the shafts should be distributed over the entire domain. The more shafts used, the higher the blockage effect, and therefore the variations in longitudinal velocity component. The flow quality is improved using aerodynamically shaped shafts. The lowest longitudinal fluctuations are when there is no shaft in the wind tunnel center line.

For the so-called W-Tunnel wind tunnel at Delft's University of Technology, a special gust generator was developed during a Master's thesis of Mechanical Engineering at the Institute of Fluid Dynamics at ETH Zürich. The development was done by J. Geertsen [16]. This gust generator uses only two shaft positions, just like the third configuration of T. T. B. Wester et al. The gust generator designed for the W-Tunnel consists of two NACA0018 airfoils. These are thicker airfoils than the NACA0009 airfoils used by T. T. B. Wester et al.

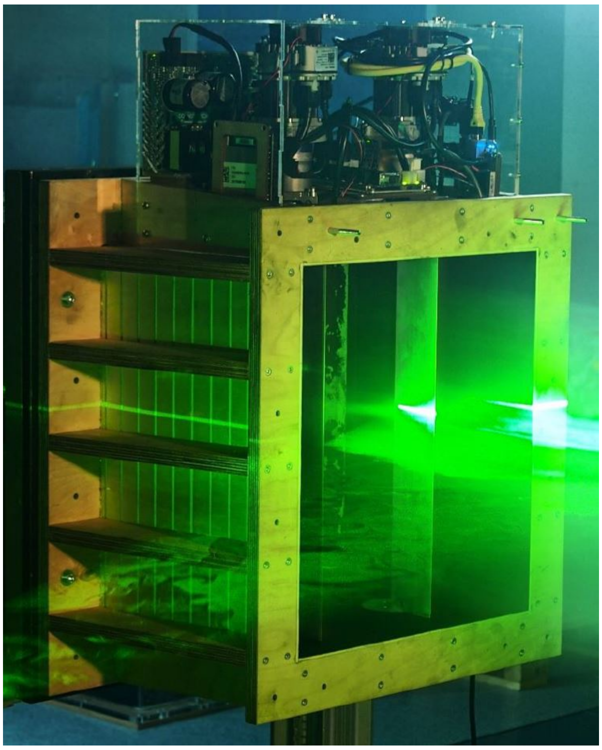

Figure 3.6: Gust generator with laser light [16]

The gust is generated by rotating the two symmetrical airfoil profiles. Since the airfoils are symmetrical, the disturbance is equal in each direction. The two NACA0018 profiles have a chord length of 80mm, which is much smaller than the 180mm chord of T. T. B. Wester et al. However, the cross-section of the wind tunnel of T. T. B. Wester et al. is much larger. The dimensions are 1.0 x 0.8m, while the W-Tunnel cross-section for the gust generator is 0.4 x 0.4m.

The gust generator is a wooden box which can be mounted to the 40 x 40cm W-Tunnel exit. Inside the wooden box, the two vertical vanes are located. The wooden box contracts a little. Therefore, the width of the gust generator contracts from 40cm to 36cm, while the height is maintained at 40cm. The two NACA0018 shaped gust vanes are mounted 16cm from each other. The maximum deflection angle of the gust vanes is $15°$, and the maximum frequency at which the gust vanes can move is 12.5Hz.

3.2.2. Experimental work with active grids

The previous subsection (subsection 3.2.1) describes what an active grid is. This subsection introduces experimental work with active grids.

S. Gambuzza [15] used various inflow models to analyse wake recovery. The various inflow models were done using a grid designed by H. Makita. M. Gambuzza experienced that wake recovery is linearly dependent on freestream turbulence intensity.

The same idea of an active grid is visible in the experiments of F. Berger et al.[8]. His experimental set-up is visible in figure 3.7. F. Berger et al. did an experimental analysis of the dynamic inflow effect due to coherent gusts. The active grid was attached to the wind tunnel nozzle. The grid consists of 80 individual controllable shafts with rectangular flaps. The flaps can be controlled to increase or decrease the wind tunnel nozzle area.

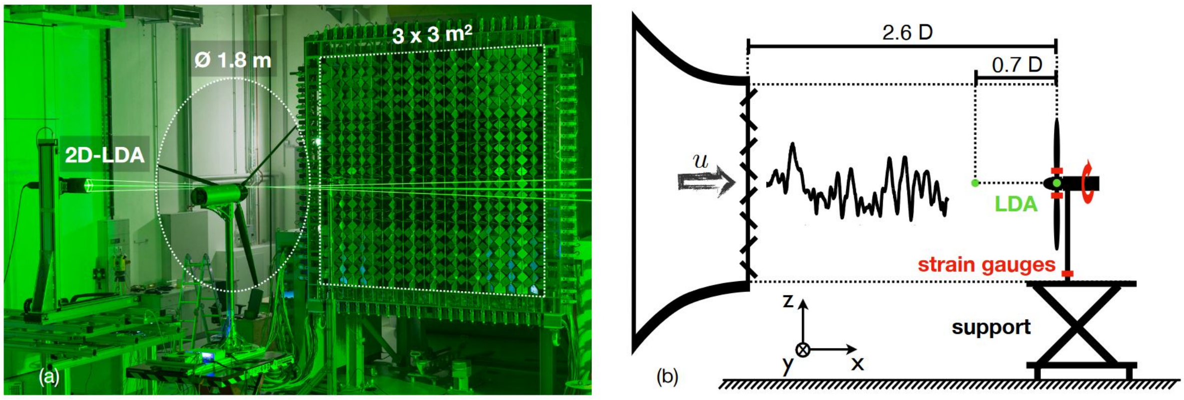

Figure 3.7: Experimental set-up (a) and Schematic set-up (b) [8]

Several conditions were tested in the experiments of F. Berger et al. In comparison to the standard dynamic inflow conditions (see section 2.2), the experiments show that the amplification of induced velocities has not such a high effect on the fatigue loads as the models are predicting. A change in the filter of the Stig-Øye model was made. This change reduces load amplitudes without changing the pitch performance of the blades. However, more work has to be done to validate dynamic inflow conditions for gusts.

Just as F. Berger et al., Zhenlong Wu et al. [55] used an active grid for the analysis of an airfoil. The active grid is able to generate an unsteady periodic inflow condition. The active grid has, in comparison to the active grid of T. T. B. Wester et al., only six independent vanes. All six vanes have an NACA0016 profile with a chord length of 0.071m.

An active grid was also used in the analysis of wind turbine blade torque [7]. The most important thing mentioned about the active grid is that the active grid is able to reproduce a turbulent pattern in a controlled manner.

Also, Qing'an Li et al. used an active grid to investigate the boundary layer of a horizontal axis wind turbine. The set-up of Qing'an Li et al. is shown in figure 3.8.

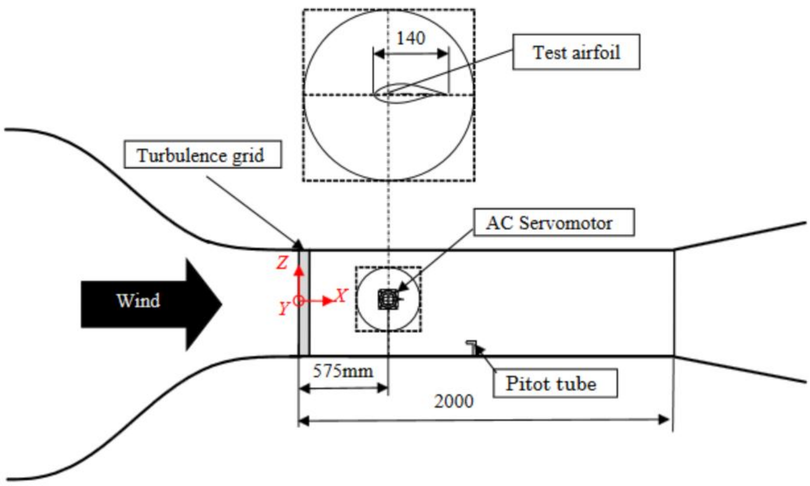

Figure 3.8: Set-up [29]

S. E. Smith et al. [50] used a passive grid in a closed loop wind tunnel to analyse a 12cm large wind turbine. In front of the passive grid, a water droplet spray generator. The wake width and velocity profile have a significant dependence on inflow velocity. Besides, the inflow velocity, also, the particles have an influence on the behavior of the flow. High inflow velocities show a greater dependence on injection flow rates. This results in diverging wakes with larger low-velocity regions.

In comparison to the previously mentioned active grids of T.T.B. Wester et al. [25]; Zhenlong Wu et al.[55]; Qing'an Li et al. [29], and S. E. Smith et al.[50], F. Campagnolo et al.[10] had a different approach to have dynamic inflow conditions in a wind tunnel. Three wind turbine rotors were placed at a large table. This table is able to rotate. In comparison to an active grid, which destabilizes the incoming flow, the large turn table rotates during the experiment and therefore creates an unstable airflow at the three wind turbine rotors. The large turn table is visible in figure 3.9.

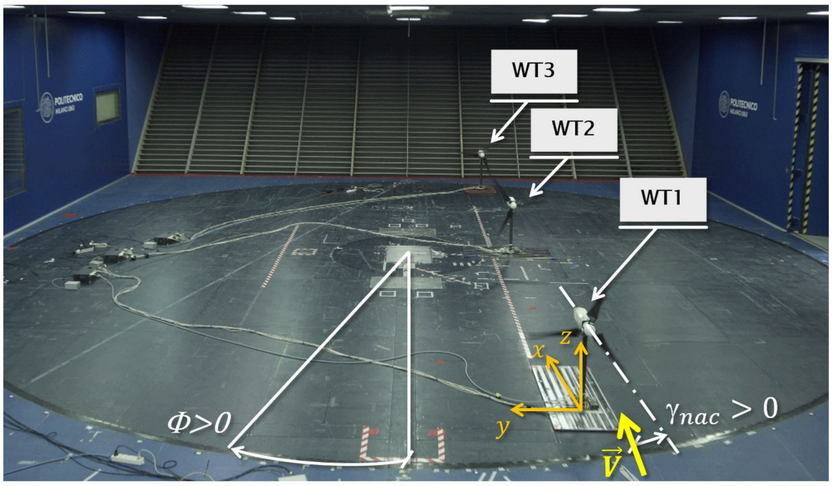

Figure 3.9: Experimental setup, showing the three model turbines mounted on the wind tunnel turntable. The x–y–z frame is fixed with respect to the tunnel and does not rotate with the turntable. [10]

3.3. Actuator disc design for experimental work

The previous section was about experimental work with dynamic inflow conditions. In this section, the design of an actuator disc for experimental work is discussed.

In the past, some experimental work has been done on actuator disc models. The design of an actuator disc has three main design drivers; the structural stiffness, the porosity, and the wake flow uniformity. Structural stiffness is important to avoid vibrations on the disc's edge. The porosity is the ratio between the open area of the actuator disc and the total area of the same actuator disc. The wake flow uniformity is important to make assumptions; for example, axisymmetric flow.

M. Huang et al. [22] have designed various porous actuator discs. The porosity of the three discs is at 44.44%. The first disc is a round disc with a diameter of 200 mm. The second disc measures 200 x 200 mm. The last disc is also rectangular and measures 100 x 300 mm. All three porous plates are made from 2 millimeter thick porous metal plates with square holes of 8 x 8 mm, while the pitch is 12 mm. In another piece of research, M. Huang et al. used a 3D-printer to print a 300 x 300 mm square plate with a thickness of 4 mm. The aperture of the plate was 4 mm; the pitch was 5 mm, which results in a porosity of 64%.

An important figure is the graph of the C_T versus the porosity. In figure 3.10, the results of various experiments are found in the wind energy literature [22]. The graph makes clear that a more porous disc generates less thrust than a solid disc.

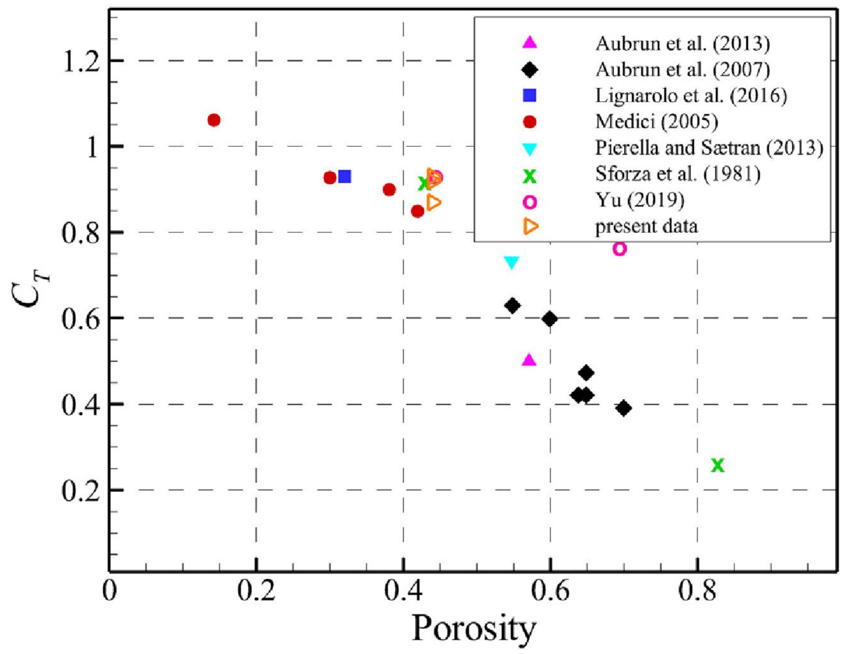

Figure 3.10: C_T versus porosity [22]

The described design of the actuator disc was used in an experiment where the flow field was analysed. The velocity field in streamwise direction of M. Huang (see figure 3.11) takes quit some time before it starts recovering. M. Huang [22] used the W-Tunnel wind tunnel at Delft's University of Technology to analyse actuator disc wake scaling for different aspect ratios. Therefore, M. Huang designed three different discs. All discs have the same porosity of 44%. The first disc has a circular shape with a diameter of 200 mm; the second disk has a square shape with dimensions of 200 x 200 mm, and the last disc has a rectangular shape with dimensions 300 x 100 mm. M. Huang used Particle Image Velocimetry (PIV) to analyse the wake of the actuator discs. The normalised freestream velocity is shown in figure 3.11. It is visible that the shape of the actuator discs influences the wake of the actuator discs.

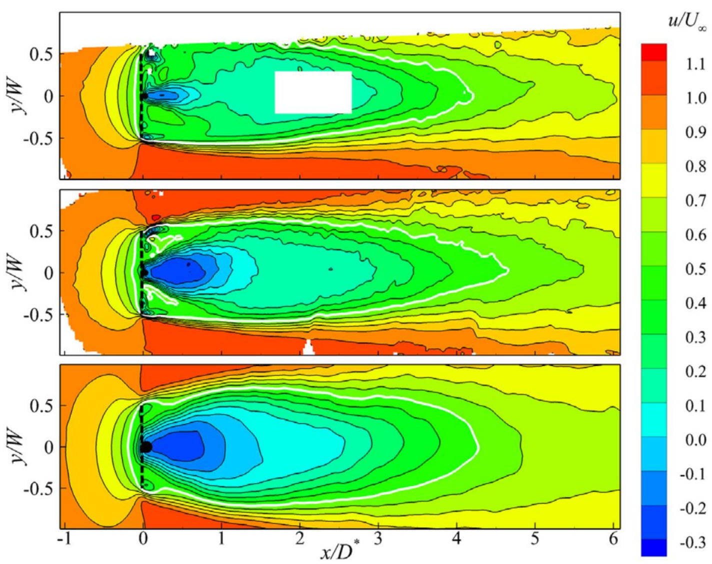

Figure 3.11: Normalised streamwise velocity. Circular (top), square (middle), rectangular (bottom) actuator. The white contour line represents the location where the wake attains 50% of the free-stream-value. The white patch is placed in an area with high uncertainty, due to an accidently increased background reflection. [22]

4

Experimental set-up and test cases

This chapter details the actuator disc model used in the experimental set-up used to capture the velocity field upstream and downstream of the actuator disc under both uniform and dynamic inflow conditions (see section 4.1). Furthermore, the same section (section 4.1), explains the used wind tunnel and gust generator. In the second section, the experimental test cases are explained (see section 4.2). The third section (section 4.3) is about the image processing of PIV images. The last section defines the positive and negative gust vane angles (see section 4.4).

4.1. Experimental set-up

The experimental set-up is introduced in this section. The set-up includes various parts, such as the wind tunnel (introduced in section 4.1.1), the PIV system (see section 4.1.3), and the gust generator (see section 4.1.2). In section 4.1.4, the actuator disc design is explained. The mounting of the actuator disc is described in section 4.1.5. An overview of the final set-up is given in section 4.1.6.

4.1.1. Wind tunnel

The W-Tunnel at the Technical University of Delft was used for the experiments of dynamic inflow conditions on an actuator disc. The W-Tunnel is an open jet wind tunnel at the TU Delft high speed lab. The W-Tunnel has three test sections. The test sections have a size of 0.4m x 0.4m; 0.5m x 0.5m, or 0.6m x 0.6m. The revolution per minute of the centrifugal fan is variable, whereby the maximum velocity in the tunnel is 35m/s. The minimum achievable turbulence level can be 0.5 percent, but it depends on flow velocity [12].

The W-tunnel has a simple set-up. Behind the plenum and the fan, the air flow passes through a diffuser. Then the air flow enters the settling chamber and the contraction before a small tunnel nozzle and tunnel exit are passed. Particles could be used in the tunnel and therefore an external ventilation system could be used to filter the added particles.

From the three available test sections, the smallest test section is selected for the experiments. The gust generator can only be connected to the smallest test section. The W-Tunnel with the smallest tunnel exit is visible in figure 4.1.

Figure 4.1: W-Tunnel

4.1.2. Gust generator

The gust generator was already introduced in section 3.2.1. The gust generator is used to generate gusts in the test section of the W-Tunnel. In the results of this report, the gust generator is used to simulate dynamic inflow conditions.

Especially for this experiment, two new scripts were written by the owner of the gust generator. The original scripts for the $1 - cosine$-script and the $sine$-script were changed with respect to the deflection angle. In the original files, the gust vanes would move in the same direction; in the new scripts, the gust vanes operate in opposite directions. An idea of the movement of the two gust vanes is visible in figure 4.2. In this figure, the black gust vane is the vane in the rest position. The red vanes show the maximum angles of the gust vanes in both scripts. Note that in the $1 - cosine$-script only one red vane is visible. The vane in this script can be at any position between the black and red vane. In figures 4.4 and 4.5, the movement of the blades is visible. The angle for the cosine (figure 4.4) is clearly visible; the amplitude of the sine a bit less, due to the smaller angle (see figure 4.5). Figure 4.3 gives an indication of the movement of the gust vane for both scripts.

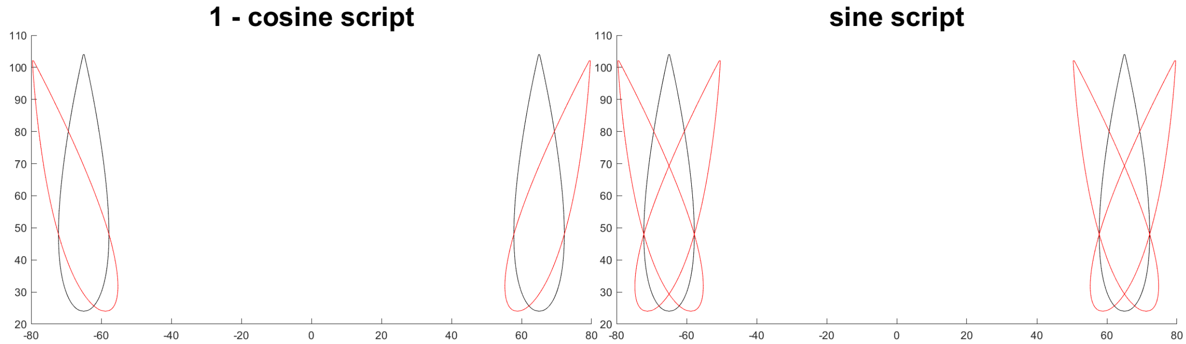

Figure 4.2: Gust vane generator

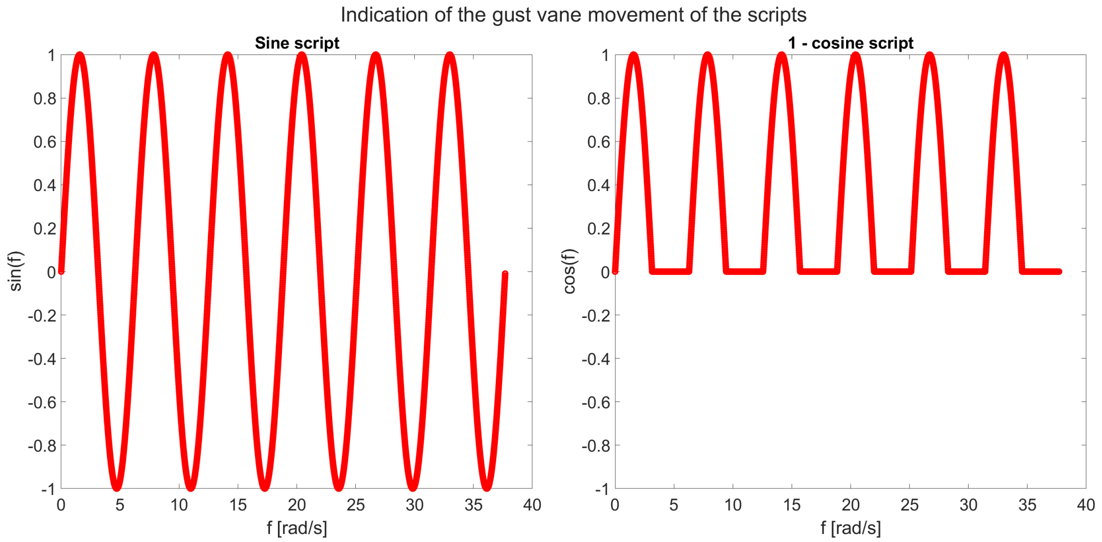

Figure 4.3: Indication of the movement of the gust vanes

Figure 4.4: Gust generator cosine

Figure 4.5: Gust generator sine

4.1.3. Particle Image Velocimetry

For flow analysis, Particle Image Velocimetry was used. This method is already discussed in section 2.5. In this section, the PIV set-up of the experiment is introduced. Two cameras were used during the experiments. Both cameras are Photron SA1.1 cameras. These cameras have various settings to take photos. An example of these settings is the number of frames which should be captured per second. The number of frames per second is dependent on the photo resolution. The higher the resolution, the lower the framerate will be, and vice versa [52]. An example of the camera is shown in figure 4.6. As a light source, a laser was used. This laser was a Quantronix Darwin Duo 527-80-M. This laser has a wavelength of 527nm, whereby the pulse repetition rate is 0.1-10kHz. The beam diameter is 3.0mm, but lenses can be used to have a different laser beam diameter. For the experiments, the laser beam will be around 3.5 disc diameters in width. Hereby, the flow field is captured from one disc diameter upstream to 2.5 disc diameters downstream.

There are in total four parts required for the PIV set-up. These four parts are: the cameras; the laser; the acquisition PC, and the PTU. The cameras and the laser are already discussed. The acquisition PC is a LaVision PTU X-2015 Serial: VX15-0294. On this computer, the DaVis program is installed. DaVis is software for intelligent imaging, as described on the website of the producer [27]. The DaVis program is able to analyse the photos of the flow field. The program analyses the particles in the flow and calculates various things from it, such as the velocity or the vorticity. The calculations are done using two images with a known time between them. The small particles in the flow have moved a certain distance between the two captured images. The velocity is then calculated by dividing the distance by the time step, which gives the velocity.

The last part of the PIV system is the PTU. The PTU or High Speed Controller is used to synchronize the camera system with the laser light. In this case, the gust vane generator was also connected to the PTU. Therefore, the gust generator was able to give a trigger input signal to the camera and laser. An example of the High Speed Controller is visible in figure 4.7.

In figure 4.8, a schematic drawing of the complete set-up is visible. Figure 4.9 also shows a complete drawing of the set-up, but now including the shifted camera. The shifted camera extends the flow field in some cases, from $x = 2.5D$ downstream up to $x = 4.7D$ downstream.

Figure 4.6: PIV Camera [38]

Figure 4.7: PTU [38]

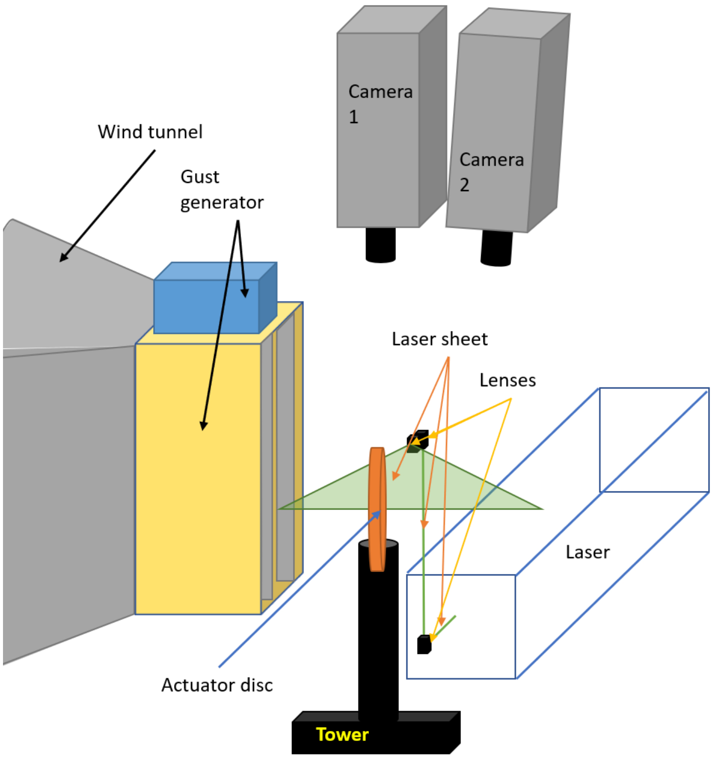

Figure 4.8: Schematic set-up with camera two in original position

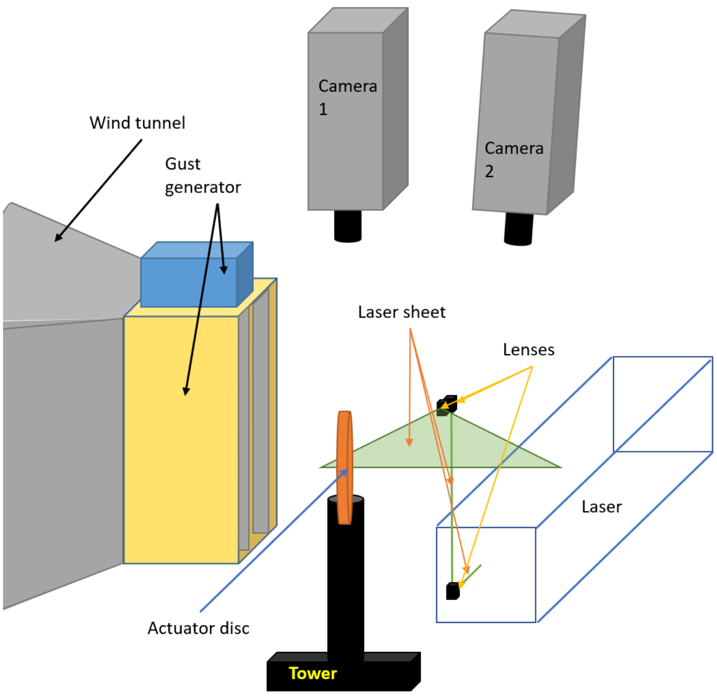

Figure 4.9: Schematic set-up with camera two in shifted position

4.1.4. Actuator disc design

The actuator discs are made of a 1mm thick aluminum sheet from the Dutch construction market, Gamma. Two different aluminum sheets were brought in. The first sheet has a mesh with 5x5 millimeter square holes. The material between the holes is 2 mm wide. The second aluminum sheet has three-millimeter round holes.

The actuator discs were made by drawing a cylinder on the aluminum sheet with black marker. A manual angle shear was used to cut the discs out of the aluminum sheet. For one set of discs, additional work was done. The 5x5 millimeter holes were enlarged using a manual punching machine. The holes were increased to 12x12 millimeters. The three designed discs to be used in the experiments are shown in figure 4.10. Hereby has Disc 3 a porosity of 73.47%; Disc 2 a porosity of 51.02%, and Disc 1 a porosity of 32.52%.

The decision that was made to use three separate actuator discs with different porosities is that it is less complex than using an actuator disc with a variable porosity. Besides, the discs are small, which increases the complexity of a variable porous disc. The distance for changing the porosity becomes very small.

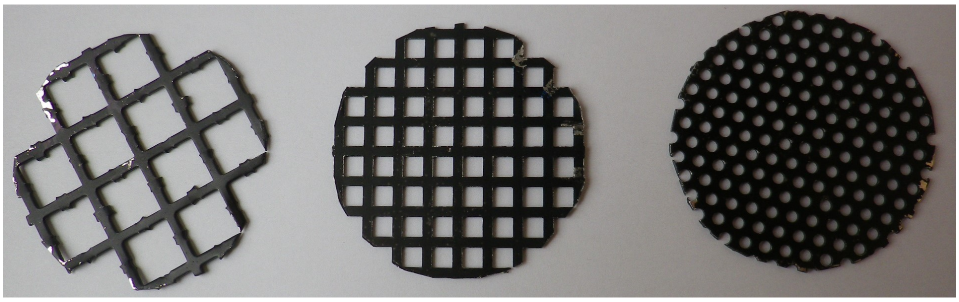

Figure 4.10: Designed actuator discs. From left to right: Disc 3; Disc 2, and Disc 1.

4.1.5. Actuator disc mounting

In the previous section, the design of the actuator discs was explained. This section is about the mounting of the actuator disc.

The actuator discs are mounted on a tower. This tower is 3D-printed. The tower was designed according to an earlier used example. The designed tower (see figure 4.11) has four holes at the bottom. With screws, washers and bolts, the tower can be mounted to an existing tool. The tower was printed in a gray color, and mounted to the tool. At the end, the tower was sprayed black to reduce the effect of reflections.

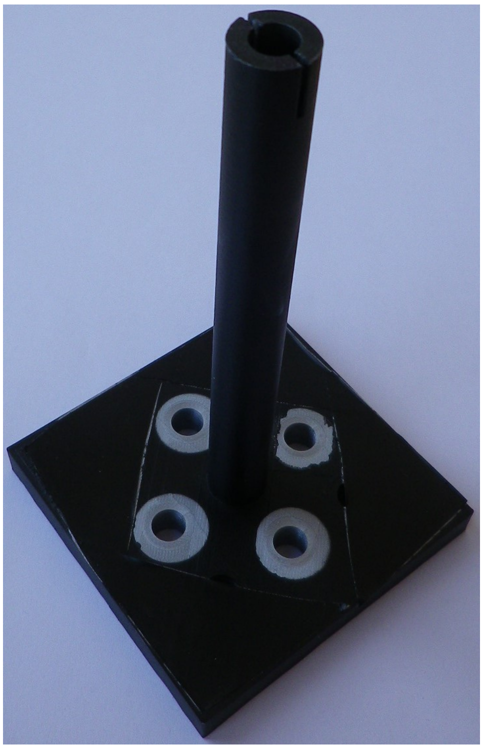

Figure 4.11: Tower

4.1.6. Final set-up

The experimental set-up is shown in figure 4.12. This set-up is called the original set-up. In this set-up, the first camera captures the bottom part of the vanes plus the three rotor diameters between the vanes and the actuator disc. Additionally, the first camera also captures up to one rotor diameter downstream. The second camera is positioned next to the first camera (see the camera on top of figure 4.12). The second camera captures the flow field from the actuator disc up to two disc diameters downstream.

In the description above, the word original is mentioned. The original set-up was used for the first round of experiments. After the first round of experiments, the second camera together with the laser were shifted around 2.5 actuator disc diameters downstream. The first camera is still in its original position (see figure 4.13). Therefore, downstream visibility was extended for certain experiments by approximately 2.25 actuator disc diameters. The shifted camera view still has some overlap with the original captured view of the second camera.

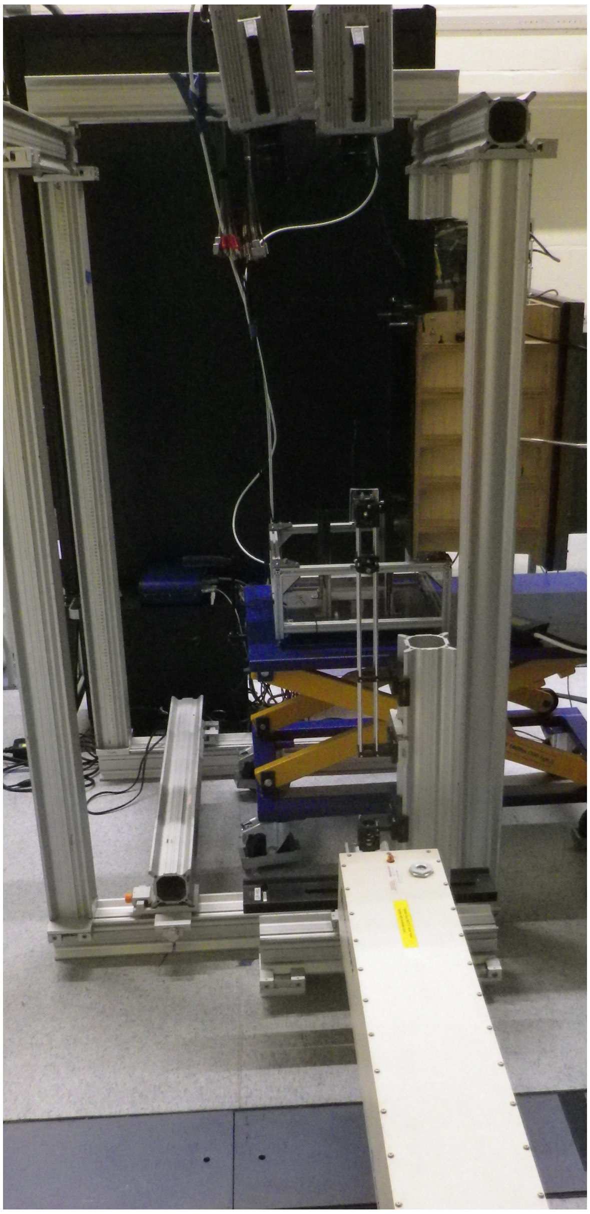

Figure 4.12: Original set-up

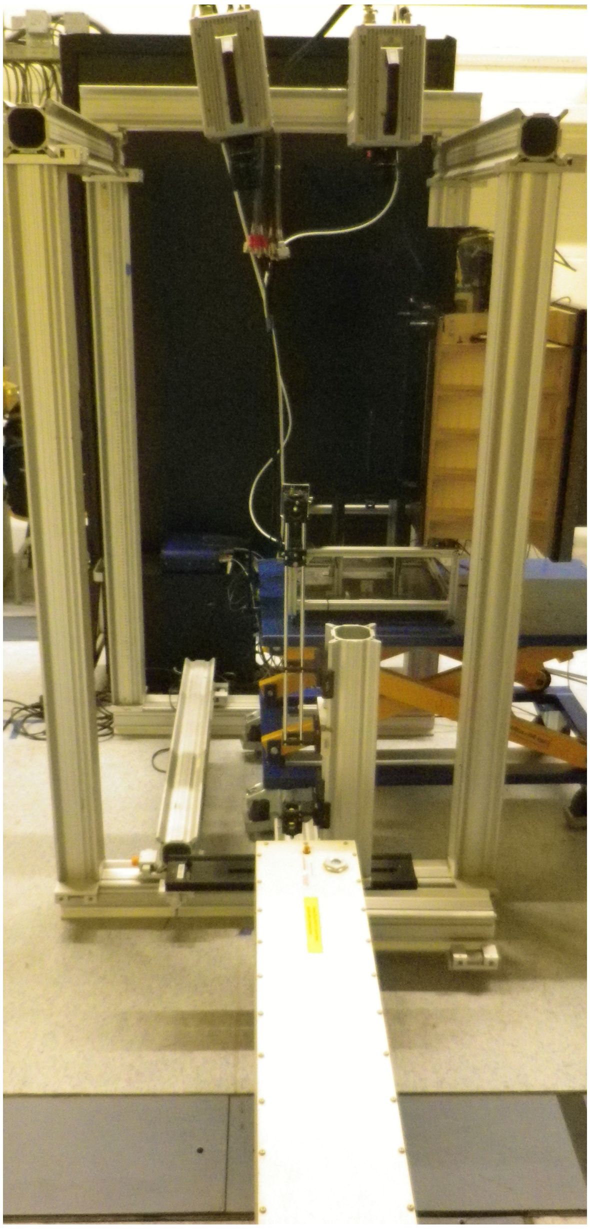

Figure 4.13: Set-up with shifted camera and laser

4.2. Test cases

In the previous section, the experimental set-up was introduced. This section is about the test cases.

Before the actual experiments started, the workings of the gust generator were checked. The first idea was to operate the two gust vanes in the opposite direction and only outboard. This should be the $1 - cosine$-script (see section 4.1.2). However, there was a small time delay between the cycles. The two vanes start at the selected frequency and move towards their maximum selected amplitude before turning back to the zero-degree deflection angle. Before the new cycle started, the vanes had a time delay of a minimum of 500ms. This time delay results in a not preferable dynamic inflow condition. The sine-script did not have a time delay between the cycles. Therefore, the sine-script was used for the experiments. However, the gust vane frequency and the gust vane amplitude are still required to be set at a certain value.

In total, there were three variables during the experiments. Two variables were obtained from the gust vane generator, namely the vane frequency and the vane amplitude. The last variable was the porosity of the actuator disc. The actuator discs were changed between the various test cases. It was most useful to keep the same disc at the test location or to use the same settings for the gust generator. The first cases made are the steady cases. An overview of the steady cases is given in table 4.1.

The tests started without a disc, because the wake of the gust vanes required some analysis. The gust should not be too strong, because then the actuator disc is in the wake of the gust vanes. However, if the gust is too weak, then there is no influence on the actuator disc.

Some tests with the gust generator led to the conclusion that a gust amplitude of 5 degrees is good for the first unsteady cases. At a 5 degree gust amplitude, the wake of the vanes seems not to merge with each other. Besides, the wake seems to be strong enough to withstand the wake of an actuator disc. Therefore, the first tests were all done with a gust amplitude of 5 degrees. During these tests, the gust frequency was changed from 12Hz at the start to 6Hz later on.

Several tests were done with the three actuator discs and without the actuator disc at a gust amplitude of 5 degrees. Although the gust frequency is expected to have a larger effect on the wake of the actuator disc, the gust amplitude was changed. The gust frequency is expected to have a large effect, because the gust frequency is a variable in the reduced frequency:

$$k = \frac{\omega D}{U_\infty} \tag{4.1}$$

In this formula, k is the reduced frequency; ω is the gust frequency in [rad/s]; D is the diameter of the actuator disc, and U_∞ is the freestream velocity. Table 4.1 shows the cases with a 5 degree gust amplitude.

Several tests were done to find a combination of gust vane amplitude in combination with gust vane frequency. The main issue is that the wake of the gust vane should not merge with the wake of the actuator disc. If this happens, the analysis is very hard, because it is unknown what wake is responsible for downstream flow. Two selections were made, a 6.5 degree amplitude with a 12Hz frequency. This selection was done for the three actuator discs and the case without the actuator disc. Besides, Disc 2 and the case without an actuator disc were also tested with the same gust amplitude, but at 6Hz gust frequency. These two last tests were selected to see the effect of a lower frequency. Disc 2 was selected, because it seemed to be a good compromise between the two other discs.

The second selection was a gust amplitude of 10 degrees with a gust frequency of 6Hz. These gust generator settings were tested with the three actuator discs and the case without an actuator disc. In table 4.1, an overview of these cases is visible.

Finally, the second camera was shifted (see section 4.1.6). At that moment, there was not much wind tunnel time left. Therefore, a critical selection has been made to see the effect more downstream. Four tests were done without gust. These four tests were for the three actuator discs and a test without the actuator disc. The last tests were done for a 5-degree gust amplitude and gust frequency of both 6 and 12Hz. These tests with shifted second camera and gust amplitude were only done for the case without a disc and for the case with Disc 2. Disc 2 was chosen, because it seemed to be a compromise between the two other discs. Table 4.1 shows the cases with the second camera in a downwind position; in other words, the shifted camera.

For the experiments, the wind tunnel was set at 420rpm, which corresponds to 4.0 m/s. However, the gust generator contracts a bit. The contraction ratio is about 1.1. So, the freestream velocity on the actuator disc is slightly above 4.0 m/s. The freestream velocity was set at 4.0 m/s, because the reduced frequency, k, is around 1 for a gust vane frequency of 12Hz.

Figure 4.14 shows the overlap of the first and second camera for the original set-up. Afterwards, the second camera was shifted in a downstream direction. The overlap of this additional area in combination with the original flow field is shown in figure 4.15.

DaVis Case	Steady / Unsteady	Shifted camera	Disc	Gust vane frequency [Hz]	Gust vane amplitude [°]	Images taken	Image capture frequency [Hz]
12	Steady	Yes	none	0	0	432	432
13			1				
15			2				
17			3				
11	Unsteady		none	12	5	2728	432
14		No	1				
16		Yes	2				
18		No	3				
19		Yes	none	6	5		216
20		No	1				
21		Yes	2				
22		No	3				
32			2	12	6.5		432
33			3				
34			1				
35			none				
36			2	6	10		216
37			3				
38			1				
39			none				

Table 4.1: Test cases

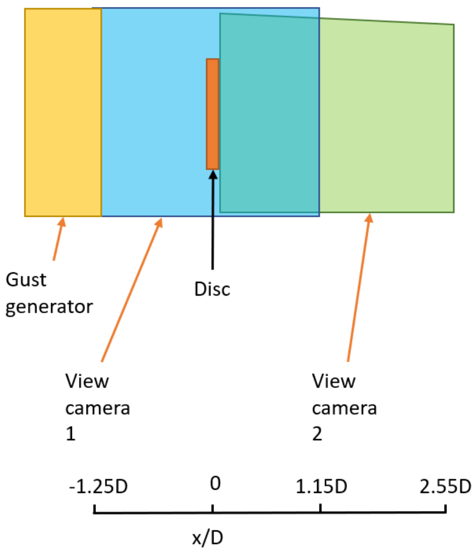

Figure 4.14: Flow field camera two in upwind position

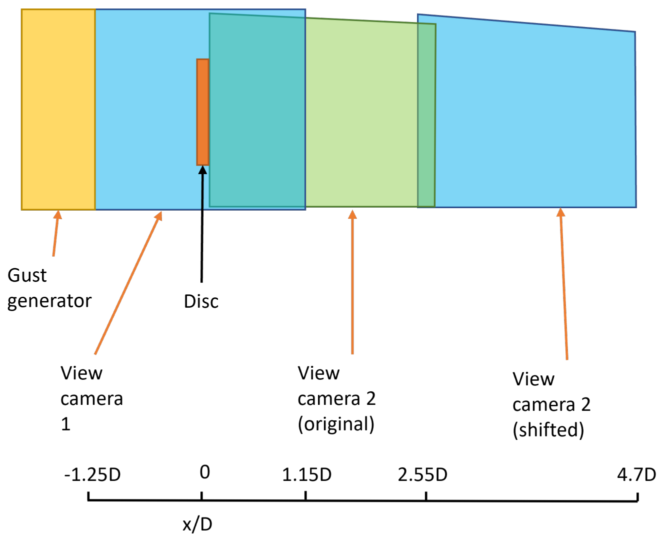

Figure 4.15: Flow field camera two in downstream position

4.3. Image processing

In the previous subsections, the experimental set-up and the test cases were introduced. This section is about image processing.

During the experiments, all images were captured by the two cameras, and saved on the acquisition PC. After the experiments, the post-processing started. DaVis 10.0.5 was used to analyse the captured images. Table 4.2 shows the parameters used for the PIV analysis. Several steps have to be taken for post-processing.

Parameters	Value
Field of View	$161 \times 205mm^2$ (camera 1); $170 \times 180mm^2$ (camera 2)
Ensemble size (images)	2728
Digital resolution	5.44 pixel/mm
Type of image processing	Sequential cross-correlation
Overlap	50%
Interrogation window size (pixels)	16 x 16

Table 4.2: PIV parameters

4.4. Gust vane amplitude

This section is about the gust amplitude and the gust frequency. The gust vane amplitude is the maximum angle, both in the positive and negative direction, to which gust vanes are moving during one cycle. The camera image capture frequency was set such that in most cases there were 36 images per cycle. A positive gust vane angle is defined as the leading edges of the two gust vanes are closer together than the trailing edges. This is visible in figure 4.16.

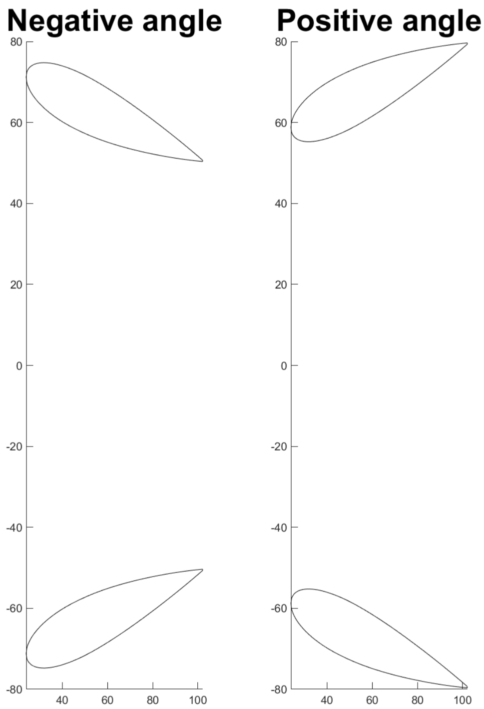

Figure 4.16: Gust vane positive and negative angle

5
Results and discussion of steady cases

In the previous chapter, the experimental set-up, and the experimental test cases were introduced. The chapter also introduced the definition of the positive, and negative gust vane angles. This chapter introduces the investigation of the experiments for steady cases.

The steady cases have been done with the second camera in upstream and in downstream position. Thus, the flow field is extended from $x = 2.5D$ up to $x = 4.7D$ downstream. In total, there are four steady cases. Namely, the three different actuator discs (see section 4.1.4), and a case without an actuator disc. Despite a large number of fluctuations in the flow field (see appendix C), the results converge to a single value (see appendix C).

Since the velocity is converged to a single value, the flow field can be analysed for steady cases. Figure 5.1 shows the non-dimensional velocity field for the four different cases. At the top left of figure 5.1, it is visible that the velocity in the wake of the gust vanes is lower than the velocity in the freestream. In the flow field of this no actuator disc case, a blue area is visible at $x = 0D$. This is at the location of the tower (see section 4.1.5). The higher velocity can be explained as follows: The tower is below the laser sheet, and the camera is focused around 2 centimeters above the tower. However, due to the fact that the tower is in freestream, the airflow is blocked by the tower. So, the flow should go around it and there are two options for the flow. The first option is to go around the tower, but this is a little difficult, due to the blocking effects of the wake of the gust vanes. Besides, this option cannot be checked, because the tower is below the camera focus. The other option is to go over the tower. Due to a decrease in flow area, the velocity can only increase to have the same mass flow. The velocity of the flow increases, and moves partly over the tower.

At the top right of figure 5.1, the non-dimensional velocity field is visible with actuator disc 1 mounted on the tower. In comparison to the case without an actuator disc, the velocity in the wake of the gust vanes is the same. The actuator disc shows a high velocity at the start of the domain. Then the velocity is decreased towards the actuator disc. Behind the actuator disc, the velocity is reduced even further. Due to the reduced velocity upstream of the actuator disc, the velocity in the region between the wake of the actuator disc and the wake of the gust vanes is increased. At the boundary of the wake, large velocity gradients exist due to the large velocity difference between the inside and outside of the wake.

The wake of the actuator disc expands up to one disc diameter downstream. From one-diameter downstream, the wake seems to be compressed. However, the wake seems not to recover to its original freestream conditions. The recovery starts only at $x = 2.5D$ downstream. The flow receives energy due to mixing. There are two reasons for the mixing. The first one is atmospheric turbulence . The second one is wake-induced mixing due to the instabilities and breakdown of the tip vortices.

Actuator disc 2 shows similar behavior as disc 1. The porosity of the second actuator disc is higher than the first disc. This results in a slightly less expanded wake of the actuator disc. As a result, the velocity is increased less in the region between the wake of the actuator disc, and the wake of the gust vane (see figure 5.1 bottom left). From $x = 2.5D$ to $x = 4.7D$, an additional wake is visible in between the wake of the actuator disc and the wake of the bottom gust vane. A reason could be an almost empty smoke machine. This was discovered after the shift of the second camera (see section 4.1.6). The smoke machine is responsible for adding particles to the airflow. An empty or almost empty smoke machine does not spread the particles properly over the flow.

Disc 3 shows a different behavior (see figure 5.1 bottom right). Immediately behind the actuator discs,the effect of the large holes in the disc is visible. In comparison to the other two actuator discs, two large areas with increased velocity are visible. The velocity is increased in this region due to a smaller area in combination with an equal mass flow. So, the velocity has to increase.

Two notes should be made about figure 5.1: The shadow region of the actuator disc is visible. The other note is the black area at the top of the image. In this area, the velocity field is not calculated correctly due to too high illumination. Another option could be that the number of particles is not set at the right setting.

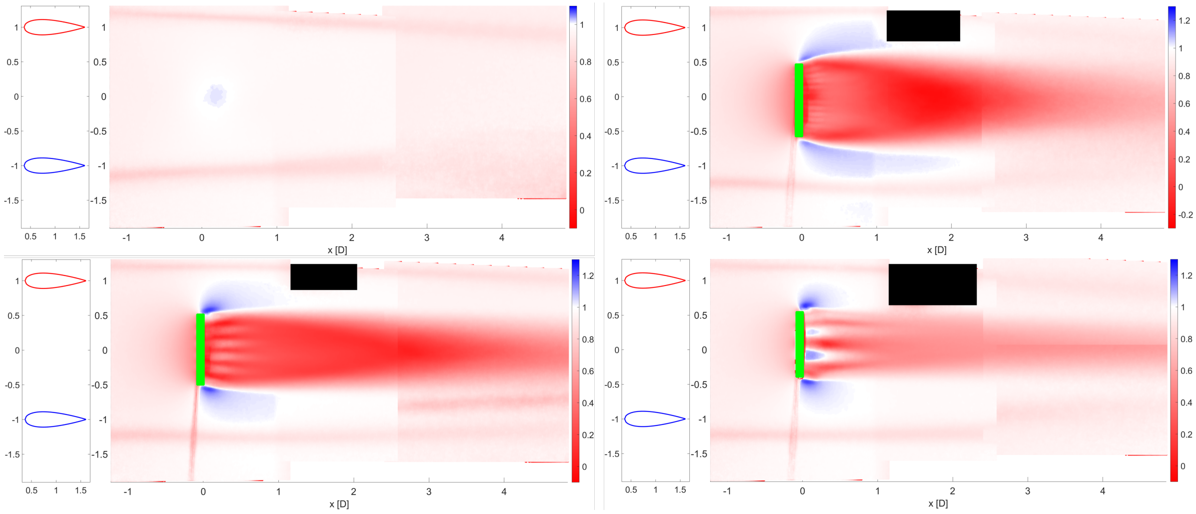

Figure 5.1: Combined non-dimensional velocity field steady cases; top left no disc; top right disc 1; bottom left disc 2; bottom right disc 3

The non-dimensional vorticity plot (see figure 5.2 top left) shows the vorticity in the wake of the gust vanes. This seems logic, because the air should move around the gust vanes, and thereby, the gust vanes are creating vorticity in the wake of the vanes. At the top left of figure 5.2, a lot of vorticity is visible at the lower part of the figure, from $x = 2.5D$ to the downstream boundary of the domain. This is due to the fact that the smoke machine for the creation of particles was empty.

Vortices are created at the gust vanes and detach from the body to move downstream in the flow. This process is called vortex shedding. The periodic detachment of these vortices results in a so-called Von Kármän vortex street. This Von Kármän vortex street is visible in figure 5.2 top left.

The non-dimensional vorticity field for the three cases with an actuator disc (see figure 5.2 top right; bottom left, and bottom right) shows large vorticity at the disc's wake boundary. This vorticity is created by the disc edge. Depending on the actuator disc, the vortex street on the wake boundaries diffuses into a broader region from $x = 0.3D$ (disc 1); $x = 0.5D$ (disc 2). For disc 3, the diffusion is harder to see. Besides, vorticity is also visible immediately behind the actuator disc. In the wake of the actuator disc, the vorticity dissipates quickly for disc 1. For the two other actuator discs (2 and 3), it takes longer before the vorticity behind the disc dissipates.

In comparison to the recovery in the non-dimensional velocity field (see figure 5.1), the vorticity field shows no recovery. And just like the non-dimensional velocity field of disc 2 (see figure 5.1 bottom left), the non-dimensional vorticity field of disc 2 (see figure 5.2 bottom left) shows the same wake in between the actuator disc's wake and the wake of the bottom gust vane. As already mentioned, this additional wake could come from the empty smoke machine.

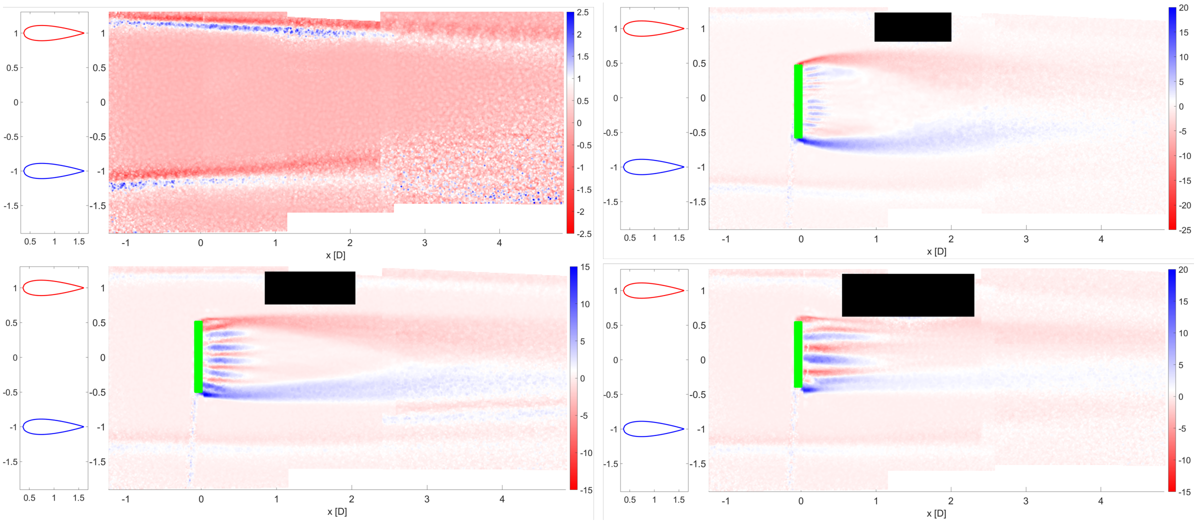

Figure 5.2: Combined non-dimensional vorticity field steady cases; top left no disc; top right disc 1; bottom left disc 2; bottom right disc 3

6

Results and discussion of unsteady cases

The previous chapter described the investigation of the steady cases. This chapter investigates unsteady cases. As already mentioned before, some unsteady cases have been done with a shifted second camera. The cases with a shifted second camera in the unsteady cases are for 5 degree gust amplitude, with 6Hz or 12Hz gust frequency. These cases are done for both actuator disc 2, and a case without an actuator disc.

Section 6.1 is about the gust. In section 6.2, the flow field is investigated. In section 6.3, the Pearson correlation coefficient is analysed. A Proper Orthogonal Decomposition analysis is given in section 6.4. The wake expansion and compression is discussed in section 6.5. The induction field upstream of the actuator disc is analysed in section 6.6. The thrust coefficients are calculated and compared to the literature in section 6.7.

6.1. Gust

This section is about the gust of the gust vanes, and its influence on the flow field.

The velocity at several locations is compared between a case without gust and a case with gust (see figure 6.1). It is visible that the velocity is fluctuating around a steady velocity. However, in some cases the velocity of the steady non-moving gust vane is higher or lower at a certain location. The velocity fields are captured most of the time, around fifteen to twenty minutes apart, due to the long saving time of the images. During this saving time, the wind tunnel is turned off. For a new measurement, the wind tunnel is turned on again, but small changes in wind tunnel settings, or measurements could be the case.

If the velocity of the case with a disc is compared to a case without a disc, it is rather difficult to draw a conclusion (see figure 6.2). Outside the wake of the actuator disc, the velocity of the case with disc is sometimes higher than the case without an actuator disc. The velocity in the wake of the actuator disc is always lower than the velocity of the case without an actuator disc.

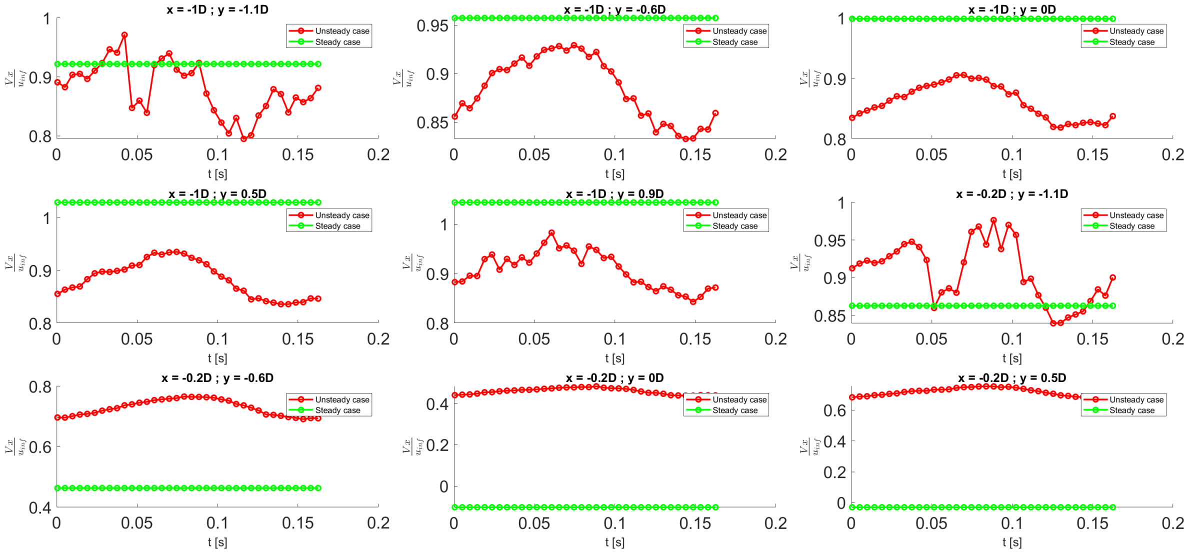

Figure 6.1: Comparison gust of steady case versus unsteady case; disc 1; 5 degree amplitude; 6Hz

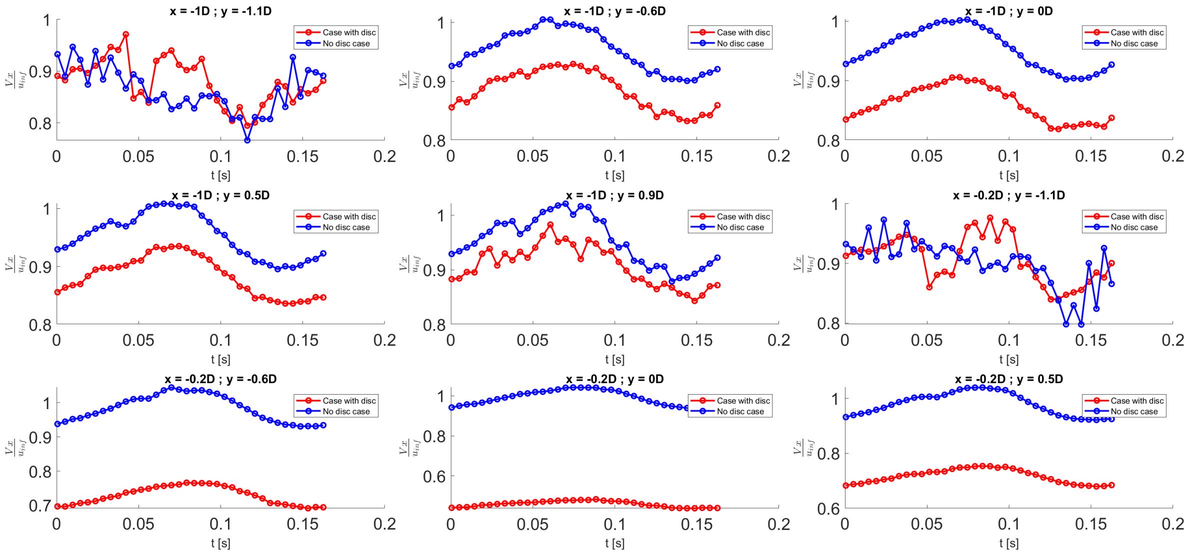

Figure 6.2: Comparison gust of case with disc versus case without disc; disc 1; 5 degree amplitude; 6Hz

An increase in gust vane frequency shows almost no changes in cases with lower gust frequency. If the steady case is compared to the unsteady case, there is almost no difference between a high and low gust frequency (compare figures 6.1 and 6.3). If a case with an actuator disc is compared to a case without an actuator disc, it is visible that upstream of the disc, the influence of the actuator disc is quite low. On the disc, or further downstream, it shows a much lower velocity in the wake of the actuator disc due to the extraction of energy by the actuator disc (see figures 6.2 and 6.4).

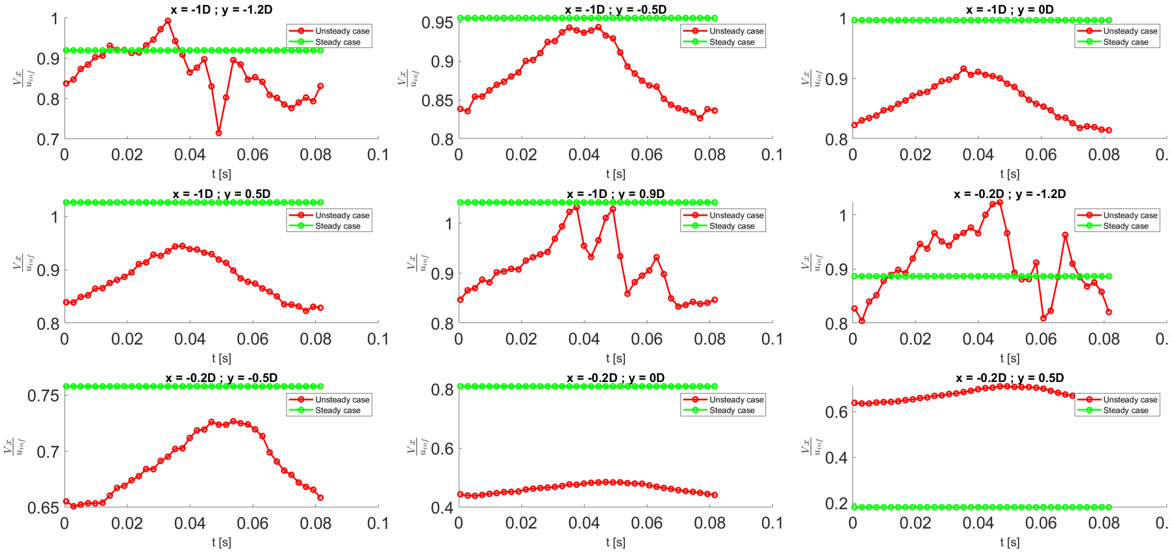

Figure 6.3: Comparison gust of steady case versus unsteady case; disc 1; 5 degree amplitude; 12Hz

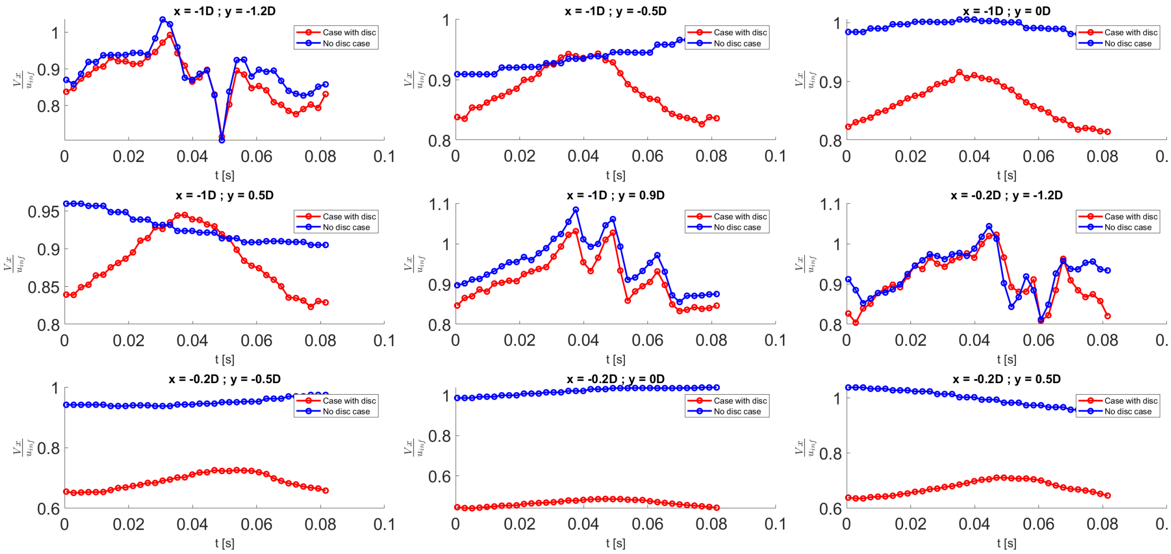

Figure 6.4: Comparison gust of case with disc versus case without disc; disc 1; 5 degree amplitude; 12Hz

A gust vane amplitude change does not show a large influence on the velocity profile in comparison to previous cases at lower gust amplitudes (compare figures 6.3 and 6.5 or figures 6.4 and 6.6).

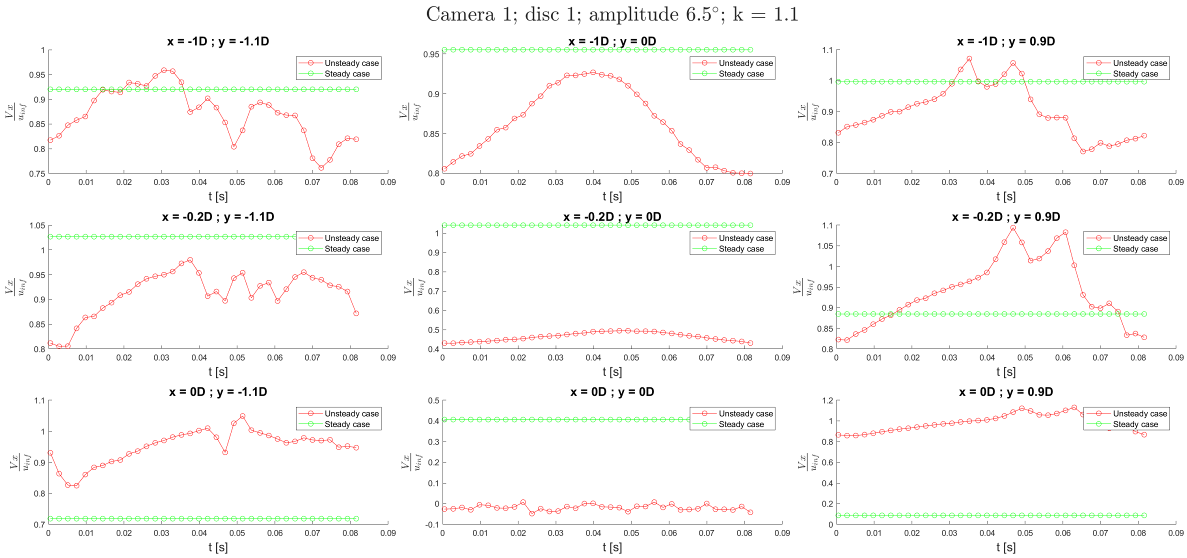

Figure 6.5: Comparison gust of steady case versus unsteady case; disc 1; 6.5 degree amplitude, 12Hz

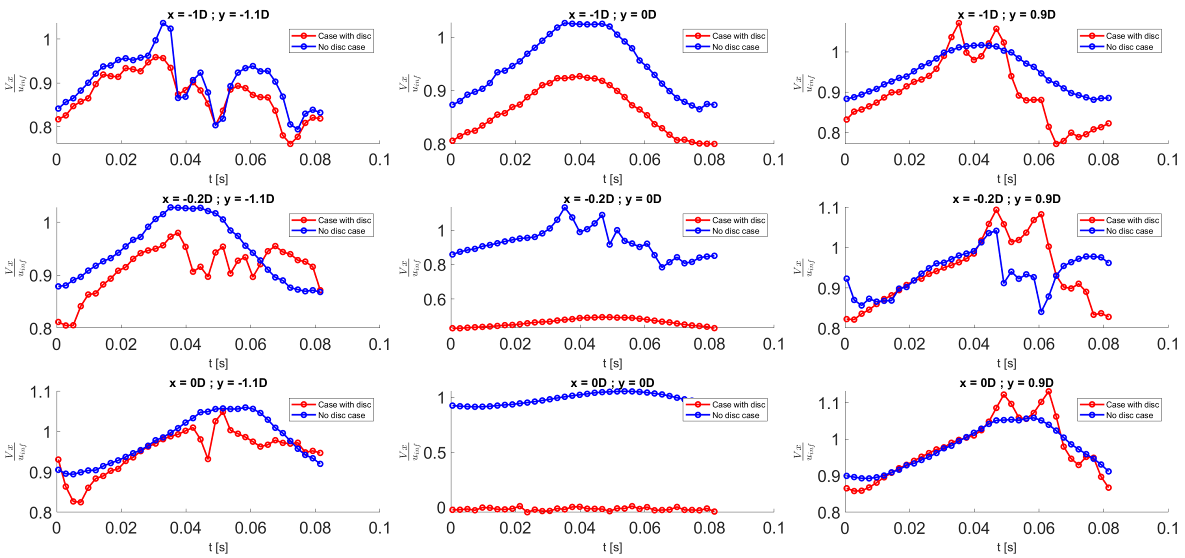

Figure 6.6: Comparison gust of case with disc versus case without disc; disc 1; 6.5 degree amplitude, 12Hz

6.2. Flow field

The previous section was about the gust; this section is about the analysis of the flow field itself.
In comparison to the cases without gusts (see chapter 5), the wake of the gust vanes moves closer together for the case without a disc. Between the two wakes of the two gust vanes, the velocity increases or decreases depending on the gust vane angle and, thereby, the area between the two gust vanes becomes smaller or wider. If the velocity is decreased between the two gust vanes, the velocity at the outside of the domain is increased and vice versa (see figures 6.7).

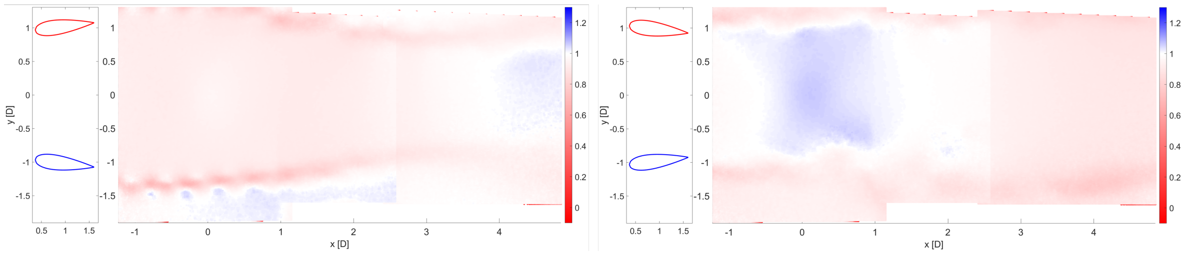

Figure 6.7: No disc; non-dimensional velocity field; 5 degree amplitude; 6Hz; left positive gust vane angle; right negative gust vane angle

The behavior of the non-dimensional velocity of cases with low frequency is the same as the steady cases. The velocity is increased or decreased due to the gust phase angle. Since there is a wake of the actuator discs, the velocity increases in between the wake of the actuator disc and the wake of the gust vanes (see figure 6.8). Also, in figure 6.8 the wake expansion and compression is visible. The wake is expanded more for negative gust vane angles, while for positive gust vane angles, the wake is compressed at $x = 2.5D$ downstream (see figure 6.8 and 6.9). The total wake expansion is dependent on the porosity of the actuator disc. The wake is expanded the most for the least porous disc, while the most porous disc has the lowest wake expansion (see figure 6.10). For wake compression, the same phenomenon is visible as for wake expansion.

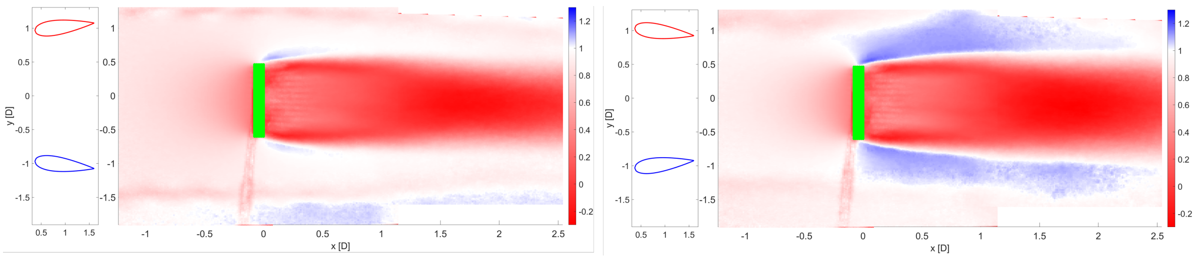

Figure 6.8: Disc 1; non-dimensional velocity field; 5 degree amplitude; 6Hz; left positive gust vane angle; right negative gust vane angle

If actuator disc 2 is mounted to the tower, a strange phenomenon happens in the far wake ($x > 2.5D$) (see figure 6.9). For positive gust vane angles, the wake in the third camera shows the wake meandering because the wake is closer to the bottom of the domain at $x = 2.5D$ and $x = 4.7D$, while at $x = 3.5D$ the wake is closer to the top of the domain. This is in contrast to the negative angles where the wake continues without movement. Since the gust vanes seem to operate normally. That means both gust vanes are moving at the same frequency and amplitude.

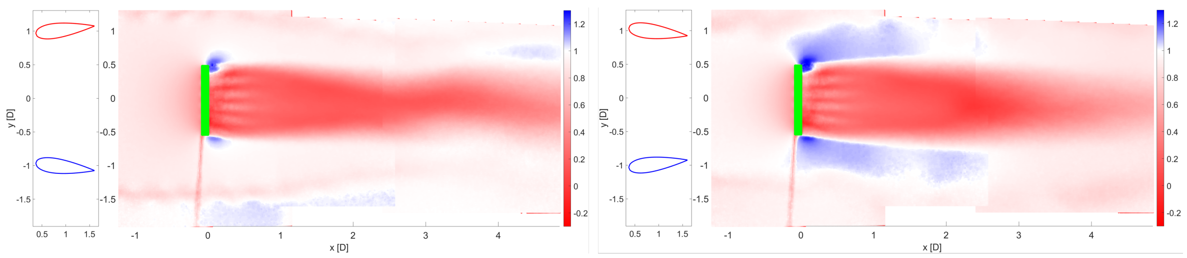

Figure 6.9: Disc 2; non-dimensional velocity field; 5 degree amplitude; 6Hz; left positive gust vane angle; right negative gust vane angle

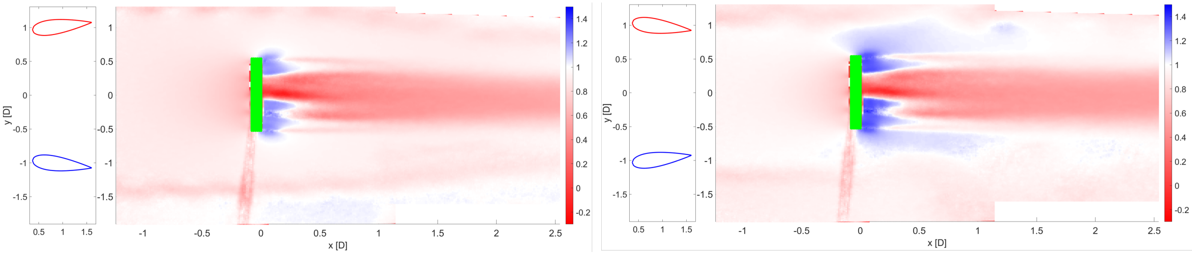

Figure 6.10: Disc 3; non-dimensional velocity field; 5 degree amplitude; 6Hz; left positive gust vane angle; right negative gust vane angle

The non-dimensional vorticity plot shows negative and positive vorticity “dots” in the wake of the gust vanes. These positive and negative ”dots” are due to the fact that the gust vanes are fluctuating. The flow starts to oscillate. Vortices are created at the gust vanes and detach periodically from the gust vanes to form a so-called Von Kárman vortex street. This phenomenon of creating vortices and the detachment of these vortices is called vortex shedding (see figure 6.11).

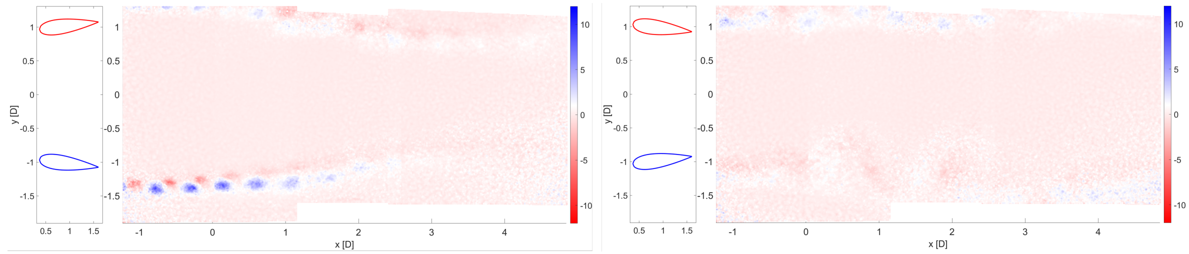

Figure 6.11: No disc; non-dimensional vorticity field; 5 degree amplitude; 6Hz; left positive gust vane angle; right negative gust vane angle

The non-dimensional vorticity is a slightly different story for cases with actuator discs. It seems that in the case of disc 1, the gust touches the wake of the actuator disc. The case with actuator disc 1 has the disc with the lowest porosity, which results in the largest wake expansion. Therefore, it is easier for the gust vane wake to touch the wake of the actuator disc. Both wakes are strong enough to withstand each other, while the wake of the gust vanes ensures a wake meandering of the actuator disc’ wake (see figures 6.12; 6.13, and 6.14).

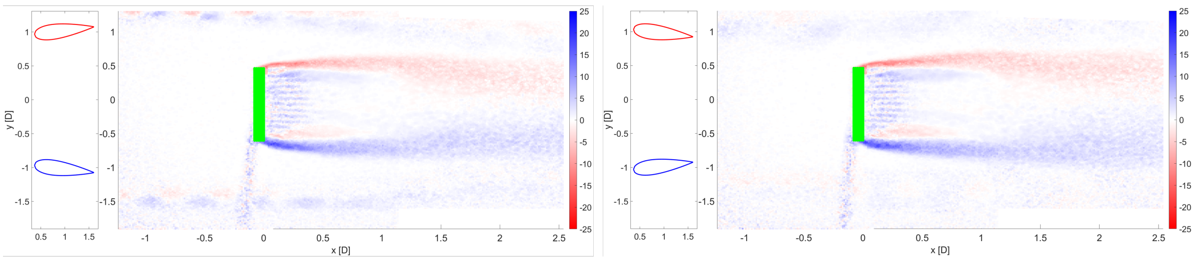

Figure 6.12: Disc 1 non-dimensional vorticity field; 5 degree amplitude; 6Hz; left positive gust vane angle; right negative gust vane angle

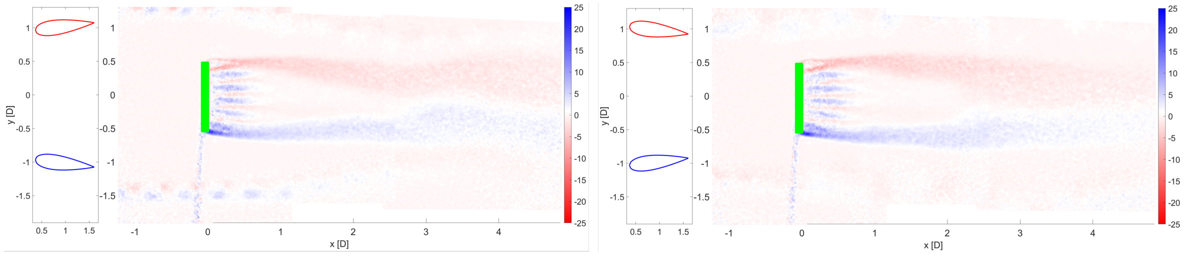

Figure 6.13: Disc 2; non-dimensional vorticity field; 5 degree amplitude; 6Hz; left positive gust vane angle; right negative gust vane angle

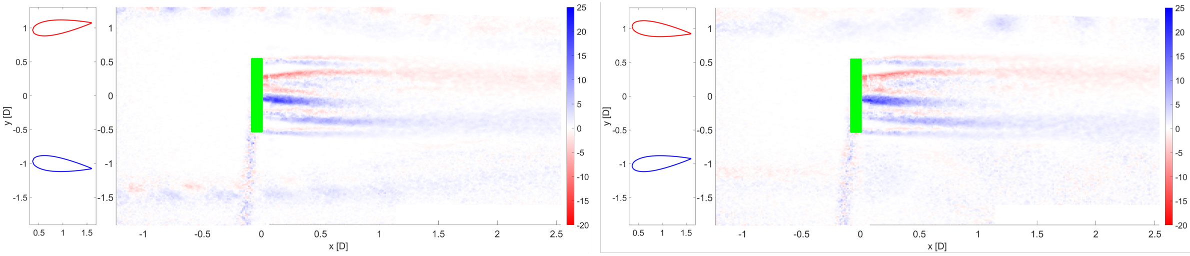

Figure 6.14: Disc 3 non-dimensional vorticity field; 5 degree amplitude; 6Hz; left positive gust vane angle; right negative gust vane angle

If the gust frequency is increased to 12Hz, the two wakes of the two gust vanes come closer together. Besides, the high velocity region appears for both negative and positive gust vane angles (see figure 6.15). From the negative gust vane angles, it can seem that the velocity in the region between the two gust vane wakes is fluctuating due to the gust vane movement. If the trailing edges of the gust vanes are closer together, the velocity increases. If the angle of the gust vane turns to a positive angle, the velocity decreases in the area between the two gust vane wakes. Due to the high gust frequency, two higher velocity regions can be seen for negative gust vane angles (see figure 6.15 right side) because the vanes are oscillating at a higher frequency. In combination with the relative low freestream velocity, the increased velocity area moves slowly downstream. Therefore, two increased velocity areas are visible for negative gust vane angles.

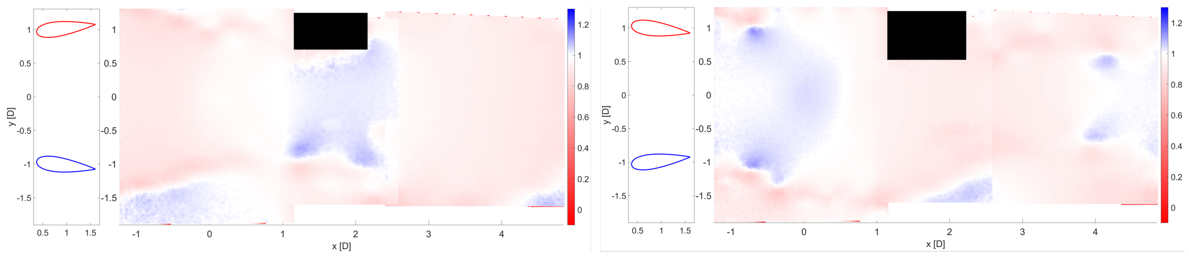

Figure 6.15: No disc; non-dimensional velocity field; 5 degree amplitude; 12Hz; left positive gust vane angle; right negative gust vane angle

In comparison to the lower gust frequency, the wake of the actuators is expanded and compressed to opposite gust phase angles (see figures 6.8 and 6.16). So, for positive gust vane angles in cases with high frequency, the wake expands, while for negative gust vane angles the wake is compressed. For cases with low frequency, it is exactly the opposite. For the other two actuator discs (disc 2, and disc 3; see figures 6.17 and 6.18), the wake expands less in these cases. As already mentioned before, the wake expansion is dependent on the actuator disc's porosity. The wake compression is stronger for higher gust frequency (compare figures 6.8 and 6.16).

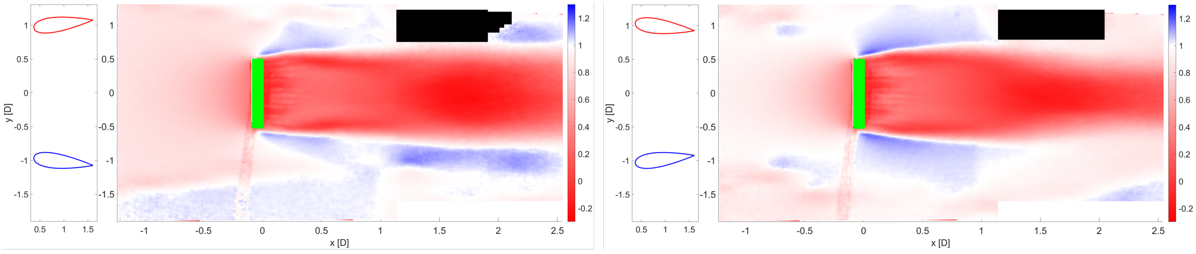

Figure 6.16: Disc 1 non-dimensional velocity field; 5 degree amplitude; 12Hz; left positive gust vane angle; right negative gust vane angle

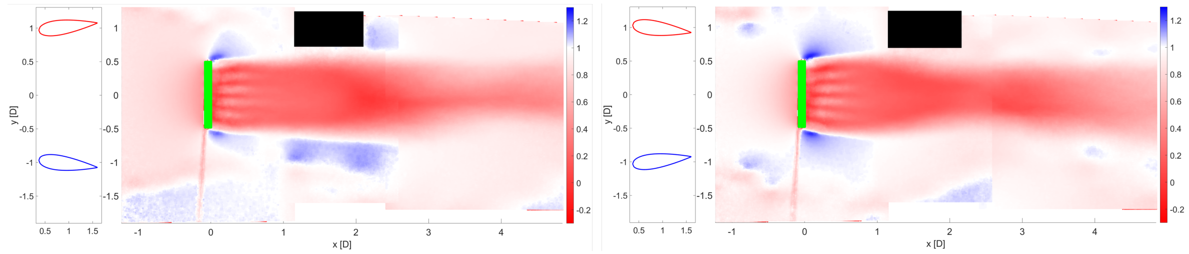

Figure 6.17: Disc 2; non-dimensional velocity field; 5 degree amplitude; 12Hz; left positive gust vane angle; right negative gust vane angle

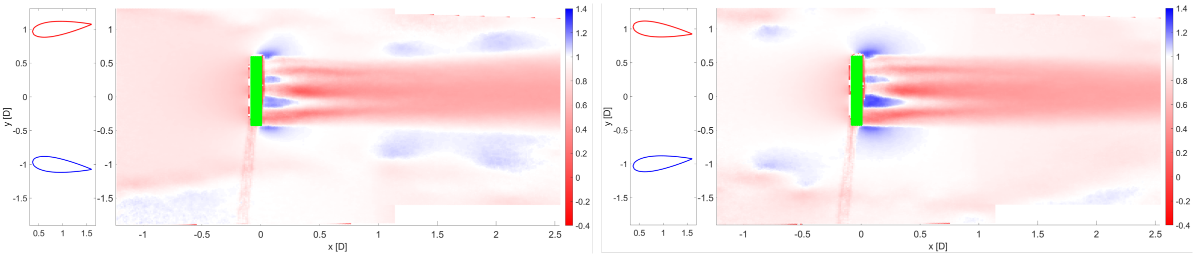

Figure 6.18: Disc 3 non-dimensional velocity field; 5 degree amplitude; 12Hz; left positive gust vane angle; right negative gust vane angle

In the vorticity plot, the sinusoidal form of the wake of the gust vane is visible. The sinusoidal form of the wake comes from the sinusoidal movement of the gust vanes. As already mentioned, this is an oscillating Von Kármán vortex street.

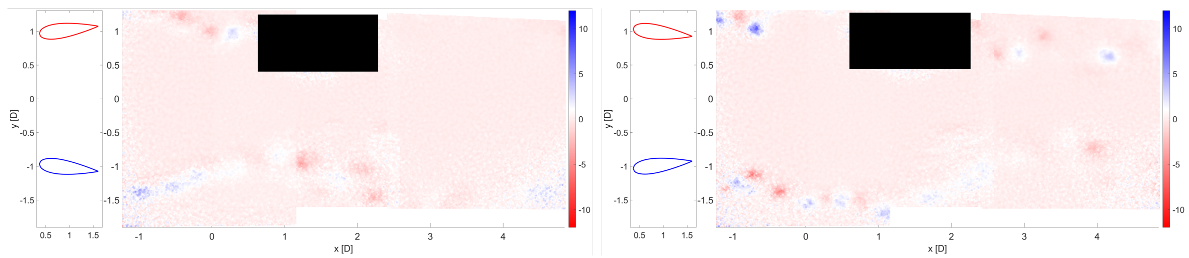

Figure 6.19: No disc; non-dimensional vorticity field; 5 degree amplitude; 12Hz; left positive gust vane angle; right negative gust vane angle

In the non-dimensional vorticity plots (see figures 6.20; 6.21, and 6.22) of the cases with double gust frequency, the wake of the gust vanes seems to touch the wake of the actuator discs. This is in comparison to lower frequency cases, where only the wake of the gust vanes of a case with actuator disc 1 is touching the wake of the actuator disc. So, a higher frequency has an influence on wake expansion and compression. At higher frequencies, the wake is expanded for positive gust vane angles. Besides, the gust frequency has an influence on the wake of the gust vanes. For higher frequnecies, the wake of the gust vane touches the wake of the actuator discs.

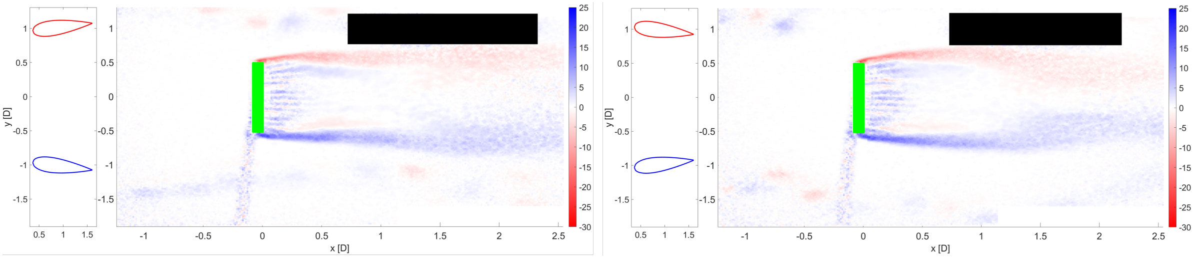

Figure 6.20: Disc 1 non-dimensional vorticity field; 5 degree amplitude; 12Hz; left positive gust vane angle; right negative gust vane angle

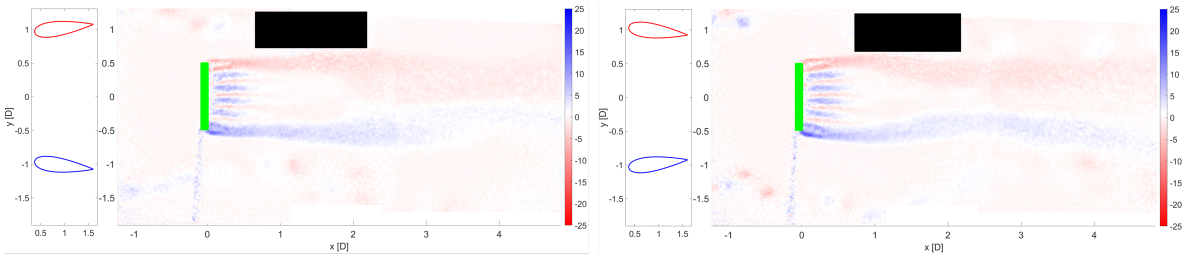

Figure 6.21: Disc 2; non-dimensional vorticity field; 5 degree amplitude; 12Hz; left positive gust vane angle; right negative gust vane angle

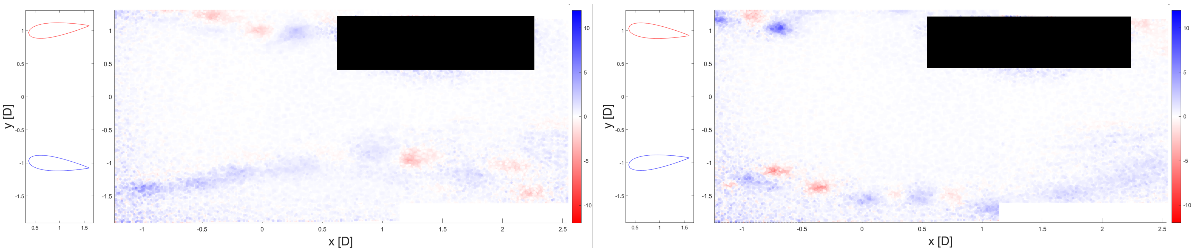

Figure 6.22: Disc 3 non-dimensional vorticity field; 5 degree amplitude; 12Hz; left positive gust vane angle; right negative gust vane angle

An increase in gust frequency, or gust amplitude, does show a similar flow in the flow field (see figures 6.23; 6.24; 6.25, and 6.26). In comparison to previous cases with lower gust vane amplitudes, the area with higher velocity seems a little larger than for the lower gust vane amplitude cases (compare figures 6.15 and 6.23).

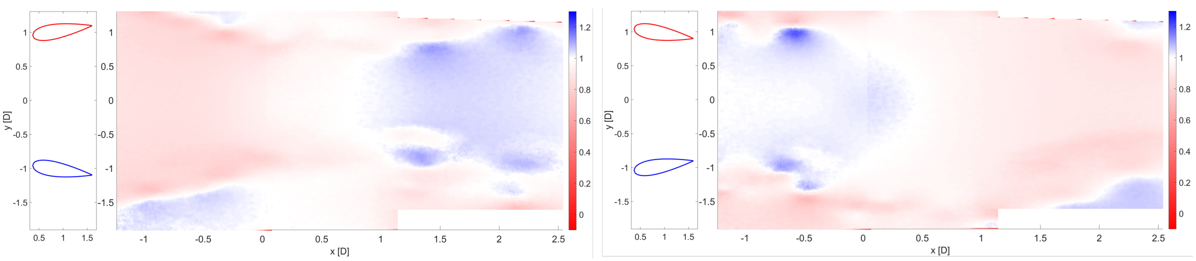

Figure 6.23: No disc; non-dimensional velocity field; 6.5 degree amplitude; 12Hz; left positive gust vane angle; right negative gust vane angle

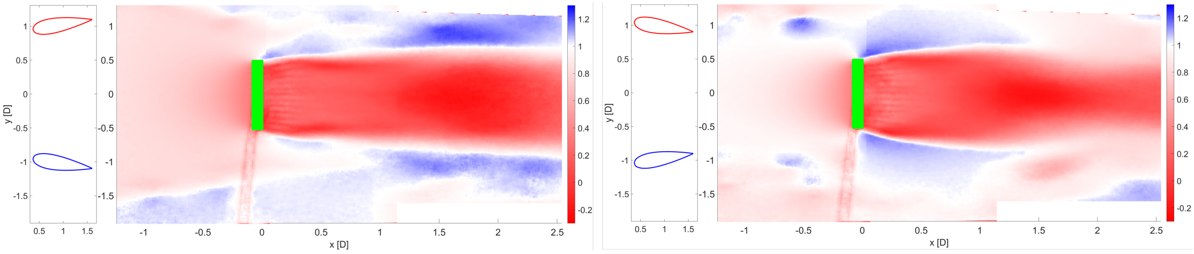

Figure 6.24: Disc 1; non-dimensional velocity field; 6.5 degree amplitude 12Hz; left positive gust vane angle; right negative gust vane angle

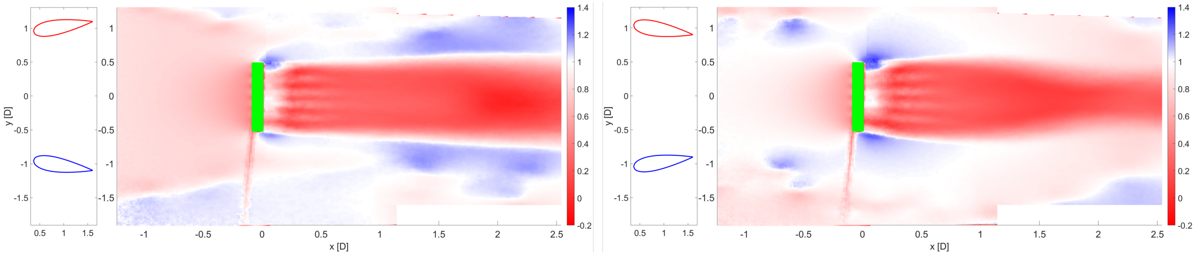

Figure 6.25: Disc 2; non-dimensional velocity field; 6.5 degree amplitude; 12Hz; left positive gust vane angle; right negative gust vane angle

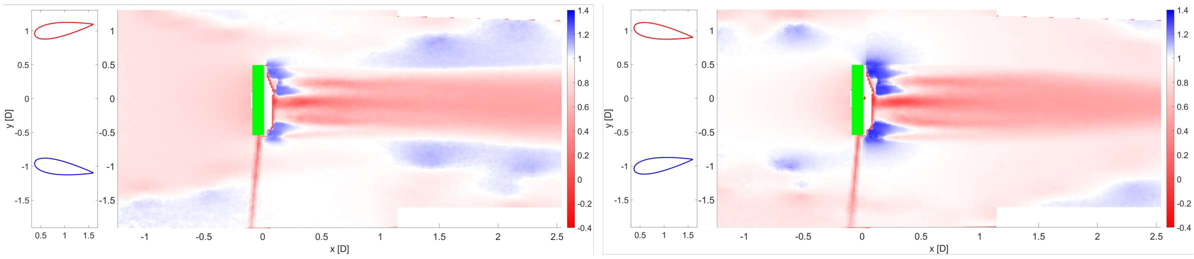

Figure 6.26: Disc 3; non-dimensional velocity field; 6.5 degree amplitude 12Hz; left positive gust vane angle; right negative gust vane angle

The wake of the gust vane seems to come closer together for the 6.5 degree amplitude case in comparison to the 5 degree amplitude case (compare figure 6.27 with figure 6.19).

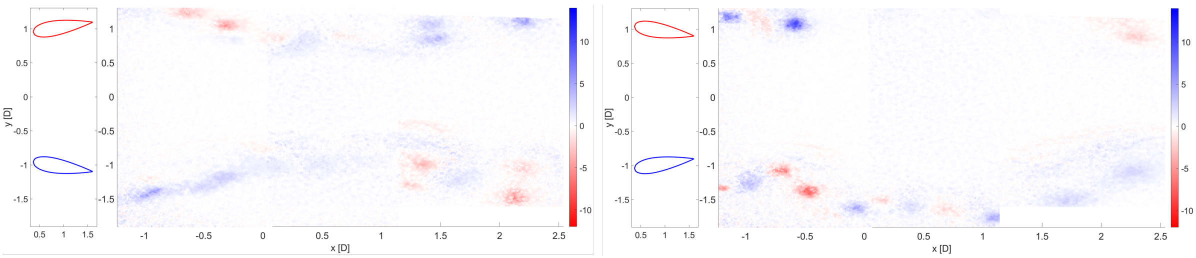

Figure 6.27: No disc; non-dimensional vorticity field; 6.5 degree amplitude; 12Hz; left positive gust vane angle; right negative gust vane angle

The non-dimensional vorticity cases with an actuator disc are similar to the cases with a slighly lower gust amplitude (compare figures 6.20 and 6.28; 6.21 and 6.29; 6.22 and 6.30)

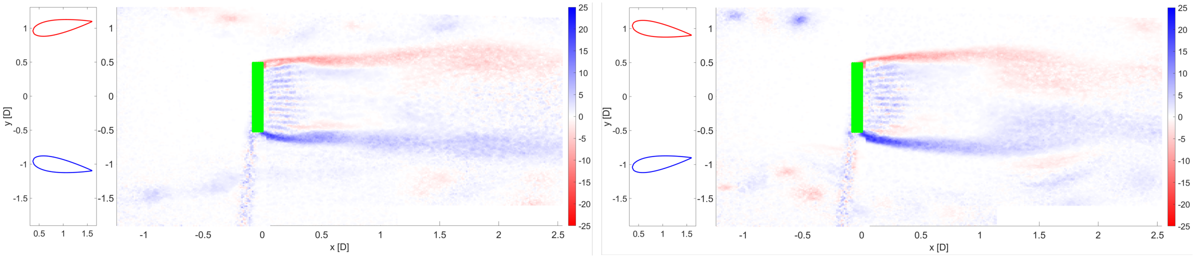

Figure 6.28: Disc 1; non-dimensional vorticity field; 6.5 degree amplitude; 12Hz; left positive gust vane angle; right negative gust vane angle

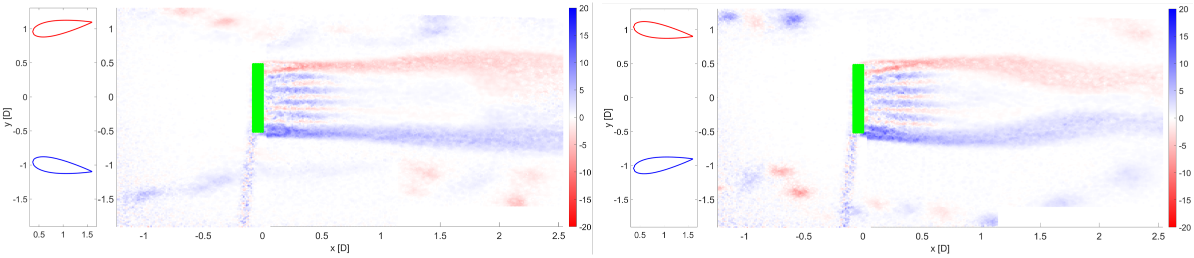

Figure 6.29: Disc 2; non-dimensional vorticity field; 6.5 degree amplitude; 12Hz; left positive gust vane angle; right negative gust vane angle

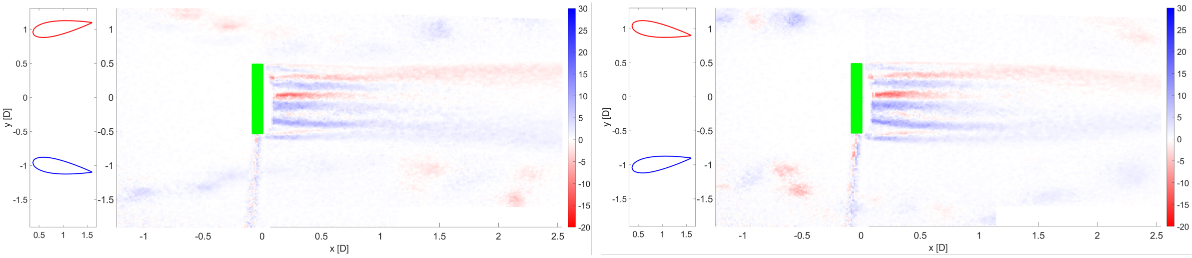

Figure 6.30: Disc 3; non-dimensional vorticity field; 6.5 degree amplitude; 12Hz; left positive gust vane angle; right negative gust vane angle

If the reduced frequency is halved, the high velocity area between the two gust vane wakes becomes very large (see figure 6.31). Next to the larger area, this area also appears at the opposite gust vane angle for the lower frequency. The case with the actuator disc shows the same opposite behavior in comparison to the high gust frequency case (see figure 6.32).

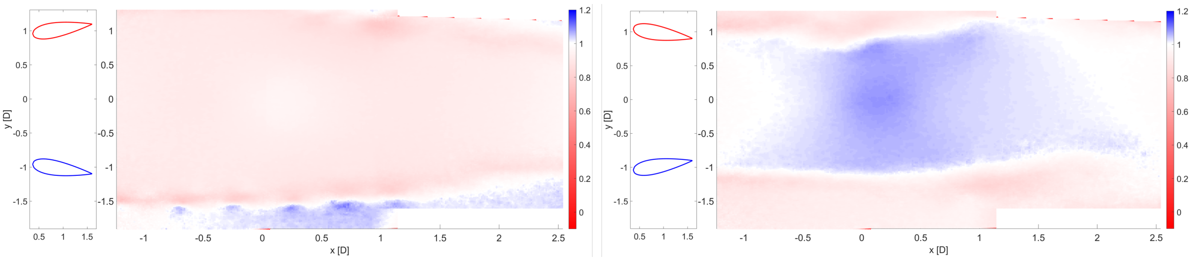

Figure 6.31: No disc; non-dimensional velocity field; 6.5 degree amplitude; 6Hz; left positive gust vane angle; right negative gust vane angle

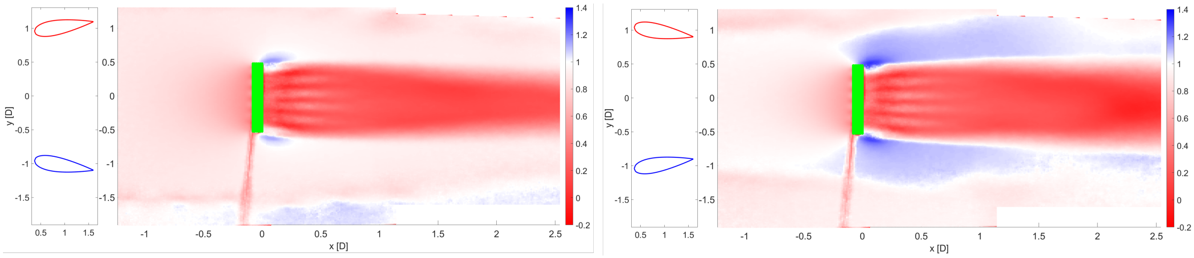

Figure 6.32: Disc 2; non-dimensional velocity field; 6.5 degree amplitude; 6Hz; left positive gust vane angle; right negative gust vane angle

The non-dimensional vorticity field shows similar changes as the velocity field (see figures 6.27 and 6.33). Also, in the case of an added actuator disc, the wake expansion and compression at opposite gust vane angles is visible in the figures 6.29 and 6.34.

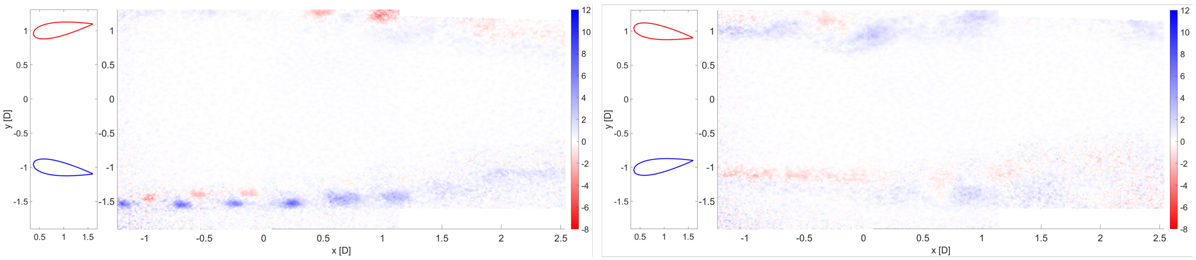

Figure 6.33: No disc; non-dimensional vorticity field; 6.5 degree amplitude; 6Hz; left positive gust vane angle; right negative gust vane angle

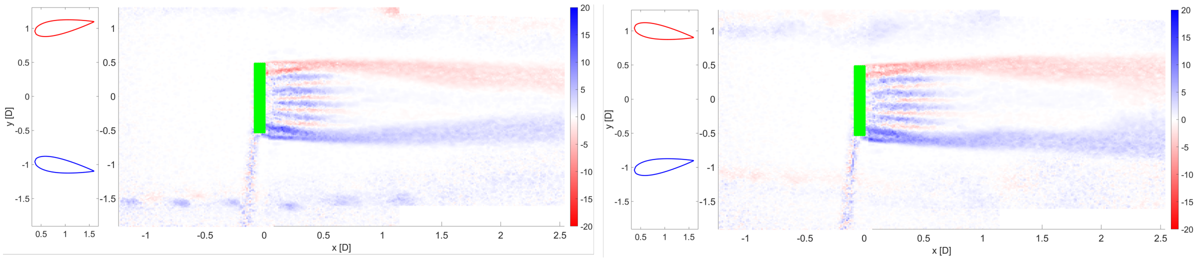

Figure 6.34: Disc 2; non-dimensional vorticity field; 6.5 degree amplitude; 6Hz; left positive gust vane angle; right negative gust vane angle

An even larger gust amplitude increases the area of higher velocity even further (see figure 6.35). The area between the wake of the actuator disc and the wake of the gust vane is small in comparison to other cases. Therefore, the velocity in this area between the wakes is increased for a larger distance than for cases with a lower gust amplitude.

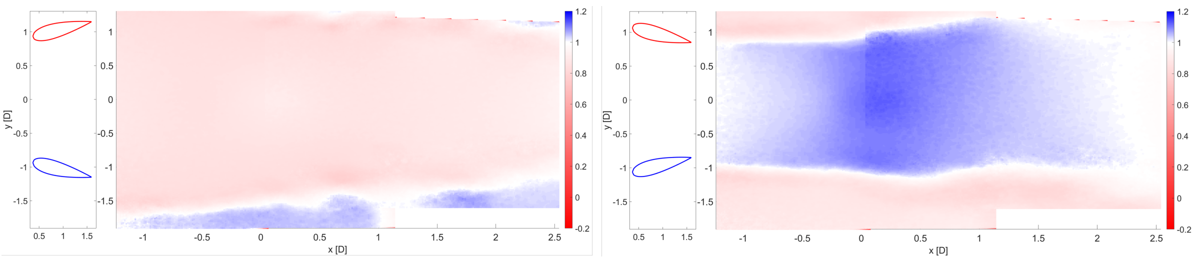

Figure 6.35: No disc; non-dimensional velocity field; 10 degree amplitude; 6Hz; left positive gust vane angle; right negative gust vane angle

The velocity increase in between the wake of the gust vanes and the wake of the actuator disc is quite high. Besides the area of this increased velocity is large in comparison to the smaller gust amplitude cases (compare figures 6.8 and 6.36; 6.9 and 6.37; 6.10 and 6.38).

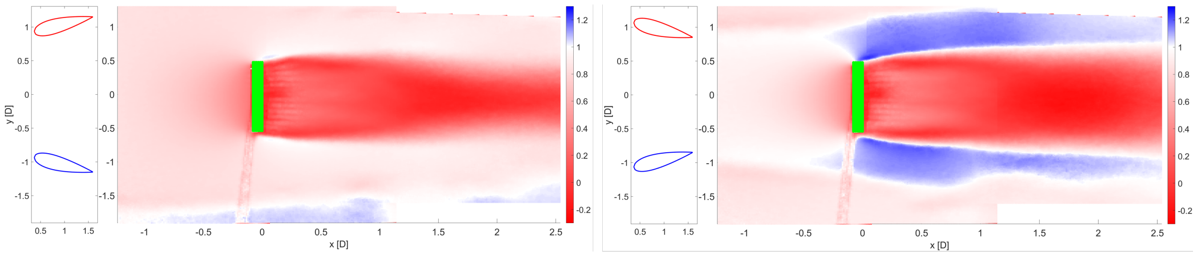

Figure 6.36: Disc 1; non-dimensional velocity field; 10 degree amplitude; 6Hz; left positive gust vane angle; right negative gust vane angle

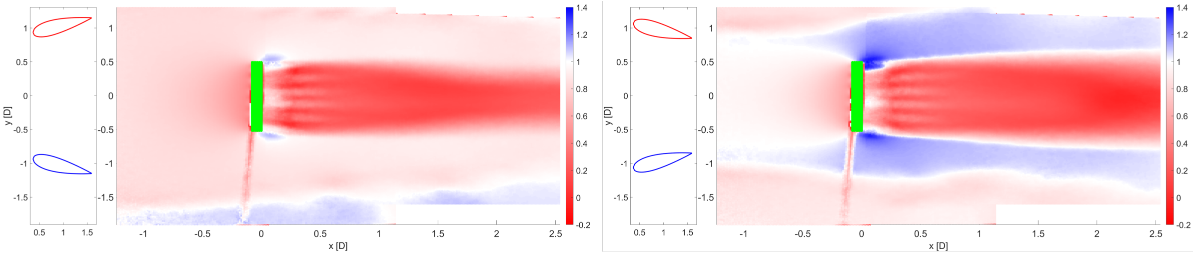

Figure 6.37: Disc 2; non-dimensional velocity field; 10 degree amplitude; 6Hz; left positive gust vane angle; right negative gust vane angle

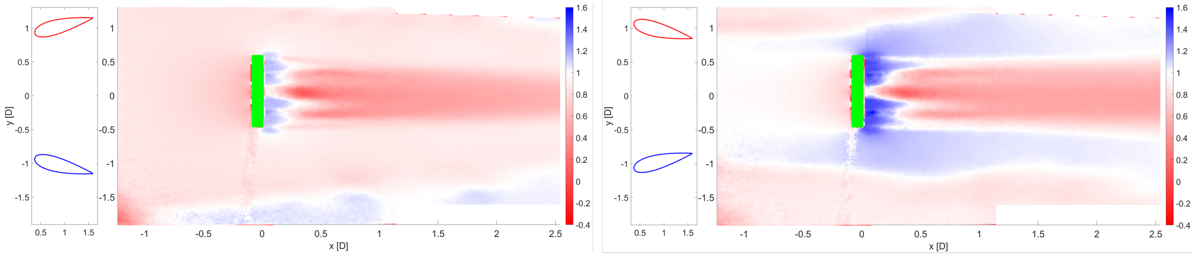

Figure 6.38: Disc 3; non-dimensional velocity field; 10 degree amplitude; 6Hz; left positive gust vane angle; right negative gust vane angle

The non-dimensional vorticity field is similar to the lower gust amplitude cases (see figures 6.11 and 6.39; 6.12 and 6.40; 6.13 and 6.41; 6.14 and 6.42).

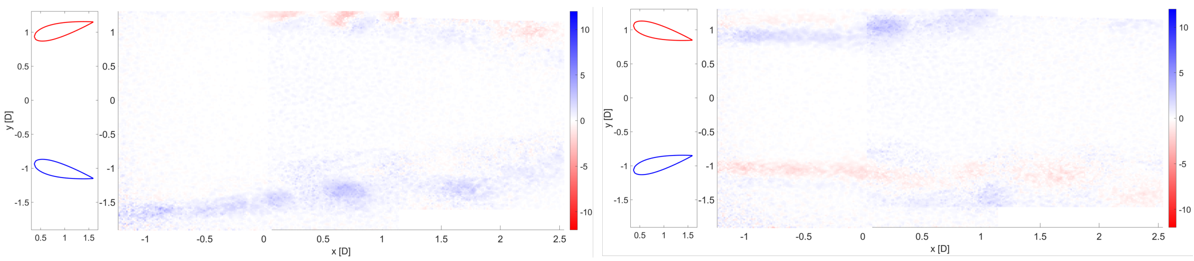

Figure 6.39: No disc; non-dimensional vorticity field; 10 degree amplitude; 6Hz; left positive gust vane angle; right negative gust vane angle

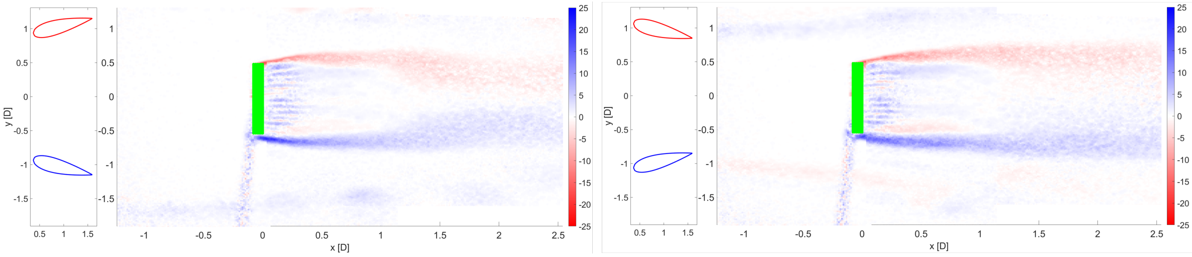

Figure 6.40: Disc 1; non-dimensional vorticity field; 10 degree amplitude; 6Hz; left positive gust vane angle; right negative gust vane angle

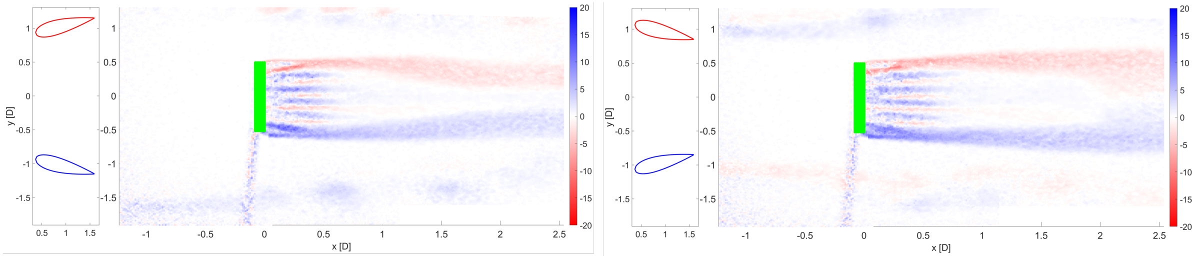

Figure 6.41: Disc 2; non-dimensional vorticity field; 10 degree amplitude; 6Hz; left positive gust vane angle; right negative gust vane angle

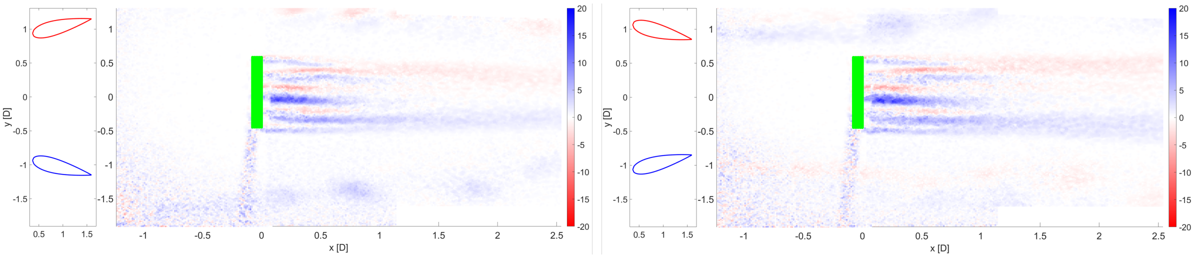

Figure 6.42: Disc 3; non-dimensional vorticity field; 10 degree amplitude; 6Hz; left positive gust vane angle; right negative gust vane angle

6.3. Pearson correlation coefficient

The Pearson correlation coefficient describes the linear correlation between two data sets. In this correlation analysis, the correlation of the velocity at the start of the flow field is checked with the velocity in x-direction in the flow field itself. The incoming velocity is taken and not the velocity given by the wind tunnel. The freestream velocity of the wind tunnel would give a zero real part in combination with a complex part. The following formula is used to calculate the Pearson correlation coefficient in the flow field:

$$r_{xy} = \frac{n\Sigma x_i y_i - \Sigma x_i \Sigma y_i}{\sqrt{n\Sigma x_i^2 - (\Sigma x_i)^2} * \sqrt{n\Sigma y_i^2 - (\Sigma y_i)^2}} \tag{6.1}$$

The correlation is strong in the region between the wake of the two gust vanes, and between $x = -1.3D$ to around $x = -0.8D$ (see figure 6.43). Afterwards, the correlation decreases. This may have to do with the increased velocity region moving downstream in the domain (see figure 6.7). The velocity is increased due to the airflow passing the gust vanes. For some angles, the area in between the two gust vanes is smaller and, therefore, the velocity is increased, while for other angles, the area between the gust vanes is larger and, therefore, the velocity is lower. However, a strong correlation is still visible around the wake of the gust vanes up to $x = 1D$. Further downstream, the correlation becomes negative, which indicates that there is no correlation.

At the outside of the domain (both on top and bottom), there is a negative value for the correlation coefficient. This means that the flow field here is not correlated with the flow field at the center of the domain. At the corners of the far end of the domain, at $x = 4.5D$, the correlation is strong between this region and the inflow condition. The correlation is strong here, because the gust has oscillated upwards, such that the freestream is able to move into this region.

If an actuator disc is added, the correlation is different (see figure 6.45). The boundary of the wake of the actuator discs has a large negative correlation with the incoming flow. The center of the wake of the actuator disc shows a partly positive and a partly negative correlation with the incoming flow. For actuator disc 1, the largest negative correlation is reached at $x = 1.2D$, After this point, the flow is slowly correlating more with the incoming flow.

For the other two actuator discs, those with higher porosity than disc 1, have a slightly different result. The largest negative point is reached further downstream in the wake, before the flow starts correlating with the incoming flow. Actuator disc 2 also shows the large correlating part further downstream in the shifted second camera region: $x > 2.5D$ (see figure 6.44). Disc 3 does only show a negative correlating part from $x > 1D$ (see figure 6.46).

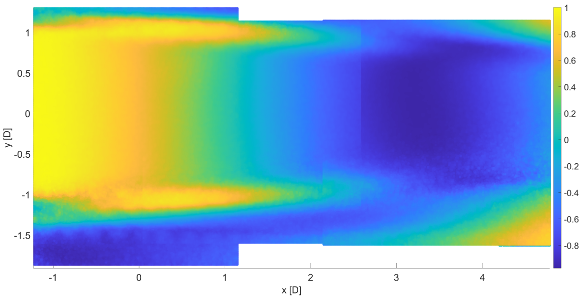

Figure 6.43: Pearson correlation coefficient; no disc; 5 degree amplitude; 6Hz

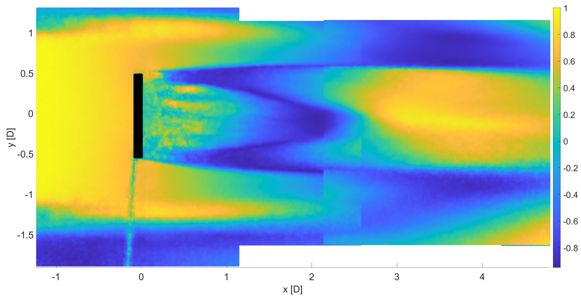

Figure 6.44: Pearson correlation coefficient; disc 2; 5 degree amplitude; 6Hz

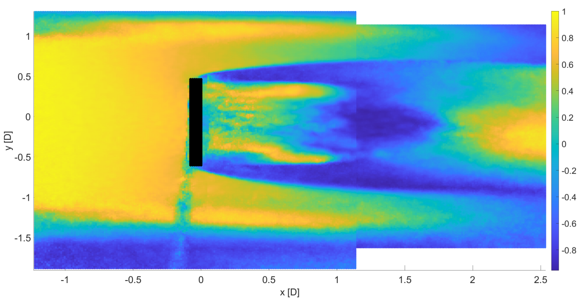

Figure 6.45: Pearson correlation coefficient; disc 1; 5 degree amplitude; 6Hz

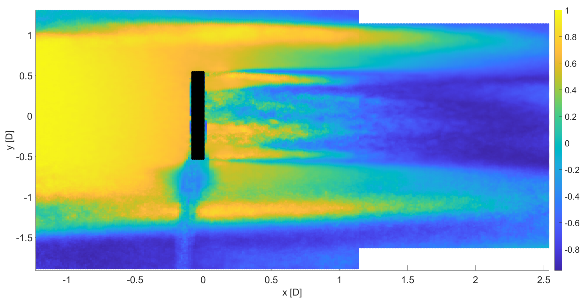

Figure 6.46: Pearson correlation coefficient; disc 3; 5 degree amplitude; 6Hz

If the gust vane frequency is doubled from 6Hz to 12Hz, or in other words, the reduced frequency is increased to 1.1, the Pearson Correlation coefficient changes slightly (see figures 6.47; 6.48; 6.49, and 6.50). The negative correlation is reached more upstream in the domain. That also means that the strong correlation further downstream in the domain happens earlier. In the case of actuator disc 2, the flow is oscillating and the wake of the disc is first correlated with the incoming flow. Then the flow is negatively correlated before it correlates at the end of the domain. Afterwards, the flow is not correlated, before it correlates again.

The faster (more upstream in the domain) correlation is also visible at the lower and upper boundaries of the domain. The flow is correlated earlier (more upstream in the domain) than for low frequency cases.

Thereafter, the flow is not correlated anymore. This is also due to the oscillating gust.

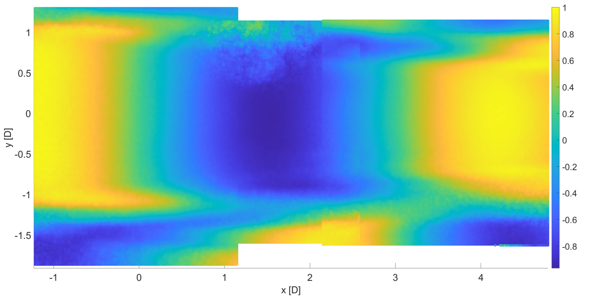

Figure 6.47: Pearson correlation coefficient; no disc; 5 degree amplitude; 12Hz

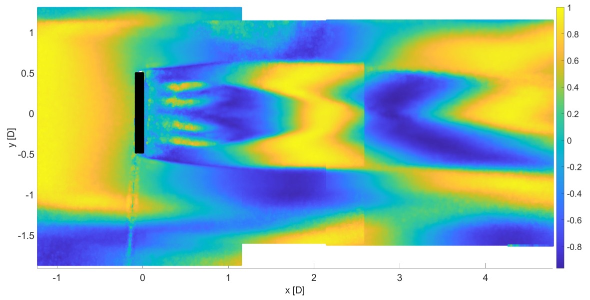

Figure 6.48: Pearson correlation coefficient; disc 2; 5 degree amplitude; 12Hz

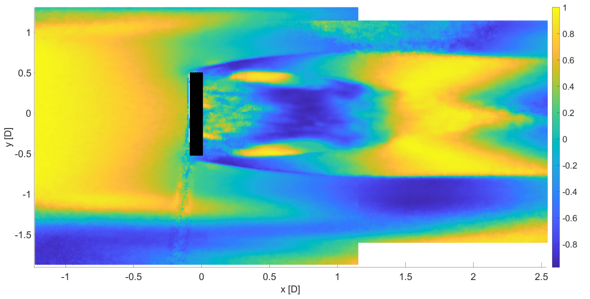

Figure 6.49: Pearson correlation coefficient; disc 1; 5 degree amplitude; 12Hz

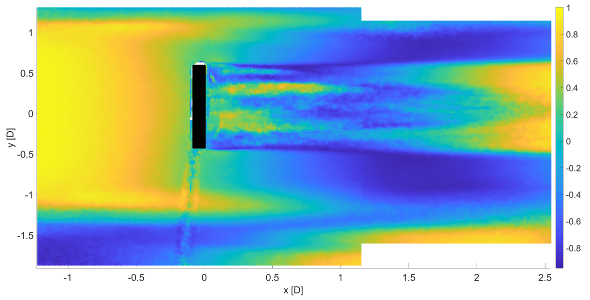

Figure 6.50: Pearson correlation coefficient; disc 3; 5 degree amplitude; 12Hz

Another gust vane amplitude does not change the correlation of the flow field. That there is no change is visible in figures 6.51; 6.52, and 6.53.

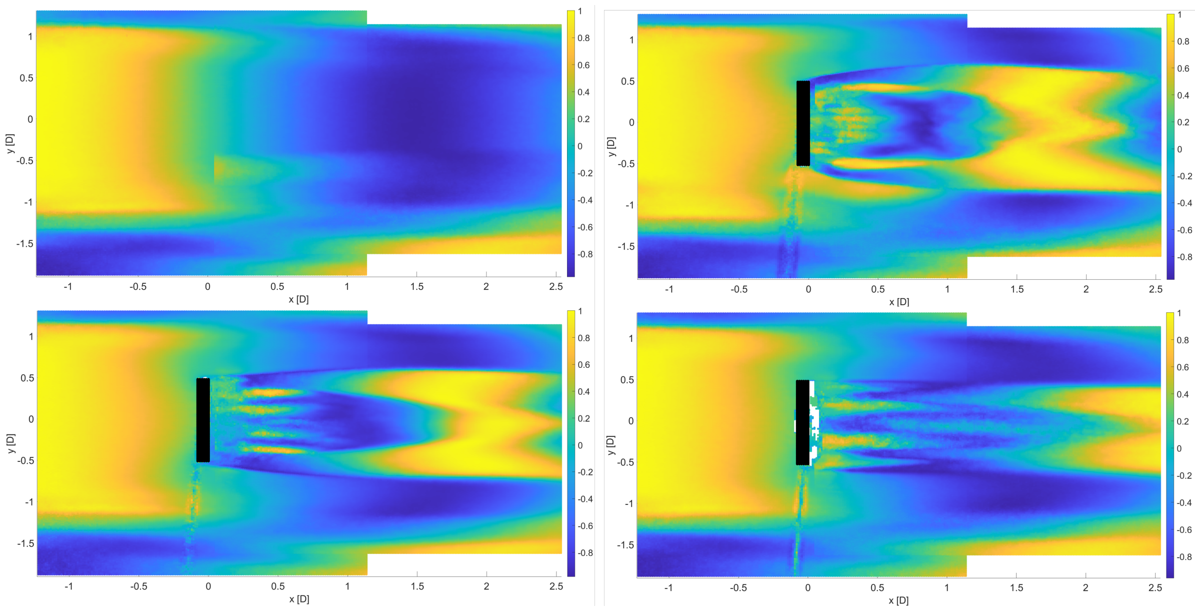

Figure 6.51: Pearson correlation coefficient; 6.5 degree amplitude; 12Hz; top left no disc; top right disc 1; bottom left disc 2; bottom right disc 3

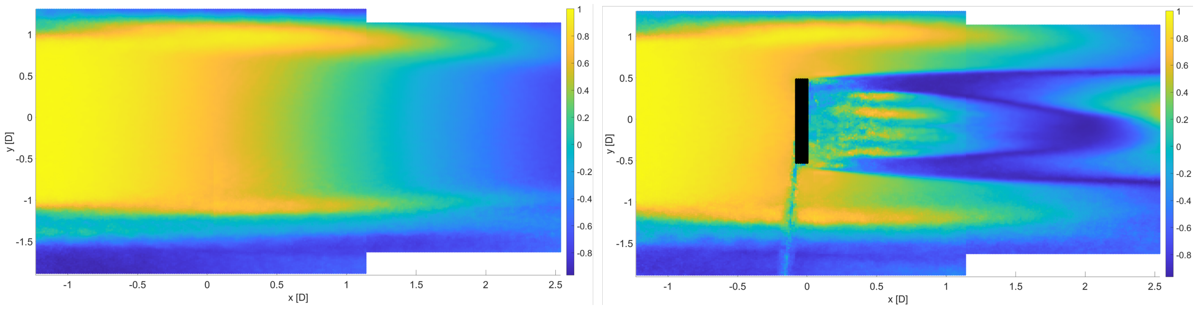

Figure 6.52: Pearson correlation coefficient; 6.5 degree amplitude; 6Hz; left no disc; right disc 2

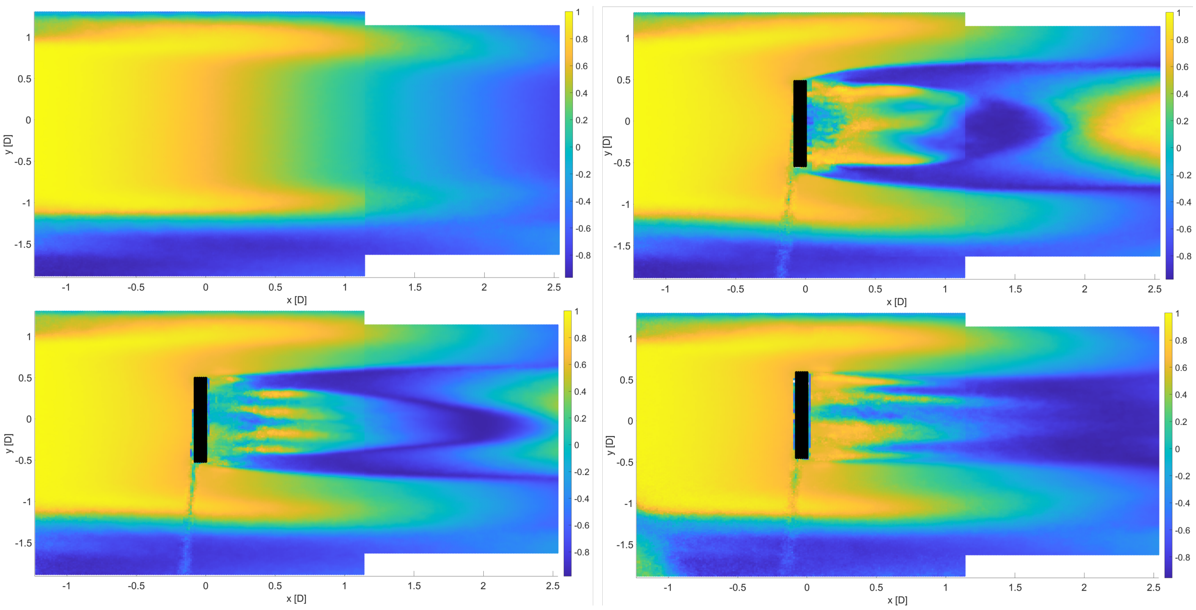

Figure 6.53: Pearson correlation coefficient; 10 degree amplitude; 6Hz; top left no disc; top right disc 1; bottom left disc 2; bottom right disc 3

6.4. Proper Orthogonal Decomposition

This subsection analyses Proper Orthogonal Decomposition (POD). POD is a numerical method that reduces the complexity of simulations. The method is typically used for fluid dynamics and turbulence analysis. The idea was that a limited number of deterministic functions could give some idea about the flow field. These deterministic functions are called POD modes.

For a POD analysis in this report, a so-called snapshot POD is used. In comparison to an n-dimensional example, the snapshot POD allows interchanging the temporal modes and spatial coefficients in the algorithm. The correlation matrix is set-up using the same $m \times n$ velocity matrix U. However, the correlation matrix for the snapshot POD is set-up as follows:

$$C_s = \frac{1}{m-1} * U * U^T \tag{6.2}$$

In this formula, $m = N_t$, which is the total number of velocity fields acquired by the PIV set-up during the experiments. $n = N_x \times N_y$, which is the number of spatial velocity points in the flow domain. Thus, C_s is built by averaging in space instead of time [54].

In figure 6.54, the eigenvalues are plotted for the disc 1 case. It is clearly visible that the first modes have the highest eigenvalues.

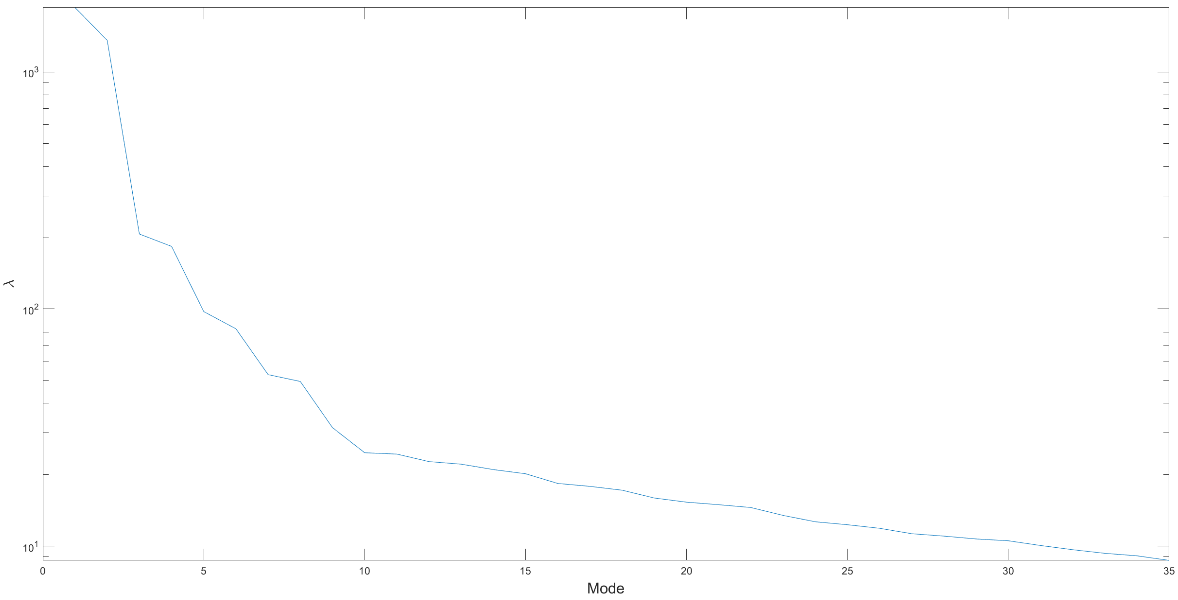

Figure 6.54: POD eigenvalues; disc 1; ; 5 degree amplitude; 6Hz

For the complexity of the flow, more snapshots are required to come to converged results [20]. That is also what is visible in these cases. The first two modes (see figures 6.55 and 6.56) have the same structure. However, the POD is not converted. The POD results are converged from the third mode. In the POD modes, the highest kinetic energy is in the wake of the gust vanes (see figure 6.57 and 6.58). These POD modes could represent the Von Karman Vortex street. The Von Karman vortex street is the result of vortex shedding. The gust vanes are creating vortices which detach from the body and move downstream to form this so-called Von Karman vortex street. In comparison to the flow field (see section 6.2), the POD shows no changes.

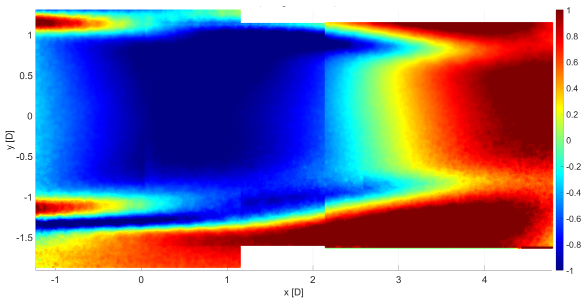

Figure 6.55: No disc, POD mode 1; 5 degree amplitude; 6Hz

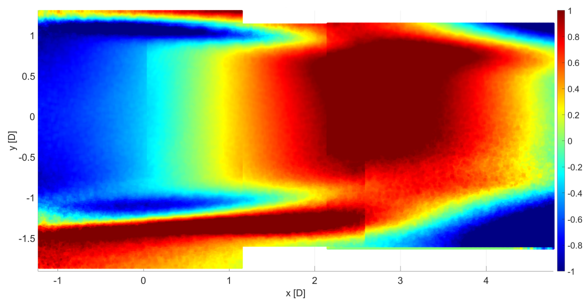

Figure 6.56: No disc, POD mode 2; 5 degree amplitude; 6Hz

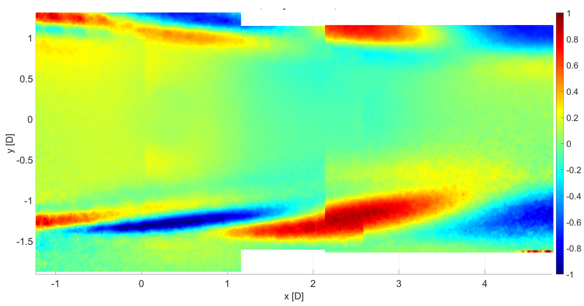

Figure 6.57: No disc, POD mode 3; 5 degree amplitude; 6Hz

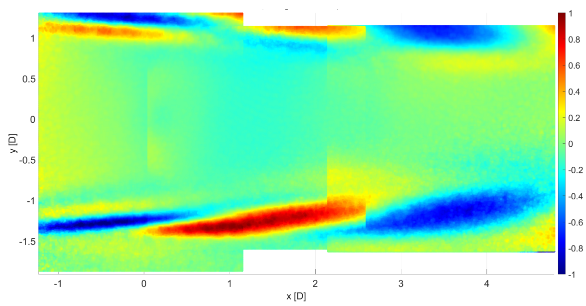

Figure 6.58: No disc, POD mode 4; 5 degree amplitude; 6Hz

Adding an actuator disc also shows the energy in the wake of the actuator disc (see figures 6.59 and 6.60).

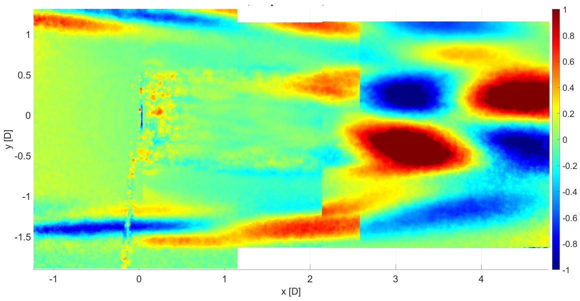

Figure 6.59: Disc 2, POD mode 3; 5 degree amplitude; 6Hz

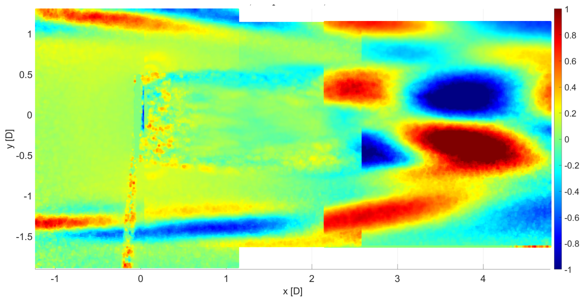

Figure 6.60: Disc 2, POD mode 4; 5 degree amplitude; 6Hz

In comparison to the low frequency cases, the POD shows nothing more in the flow field in comparison to the flow field analysis. In comparison to the lower frequency case (see figure 6.57), the 'dots' are now smaller (see figure 6.61, and 6.62), and a higher number is visible. This is due to the higher frequency. The gust is oscillating faster.

The increase of high energy regions is also visible in figures 6.63, and 6.64. The high enegry regions in the wake of the actuator disc could represent the tip vortes created by the disc edges (see figures 6.61 and 6.62).

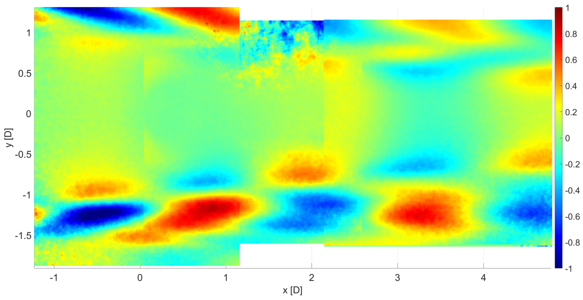

Figure 6.61: No disc, POD mode 3; 5 degree amplitude; 12Hz

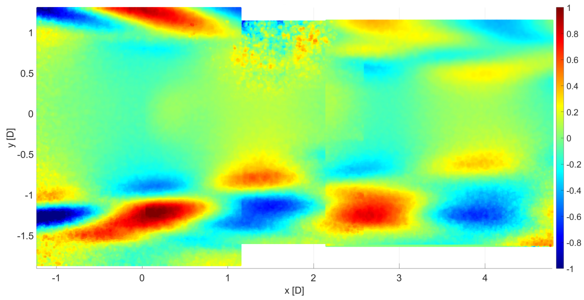

Figure 6.62: No disc, POD mode 4; 5 degree amplitude; 12Hz

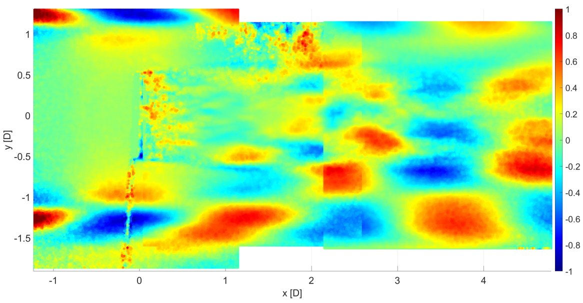

Figure 6.63: Disc 2, POD mode 3; 5 degree amplitude; 12Hz

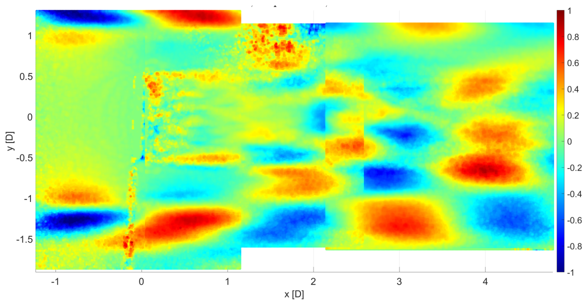

Figure 6.64: Disc 2, POD mode 4; 5 degree amplitude; 12Hz

An increase in gust amplitude increases the number of high kinetic energy regions (compare figures 6.61 and 6.65). If an actuator disc is added, the highest energy in the wake of the actuator disc is now at the wake's boundary. In the lower amplitude case, the energy was more spread over the wake (compare figures 6.63 and 6.67).

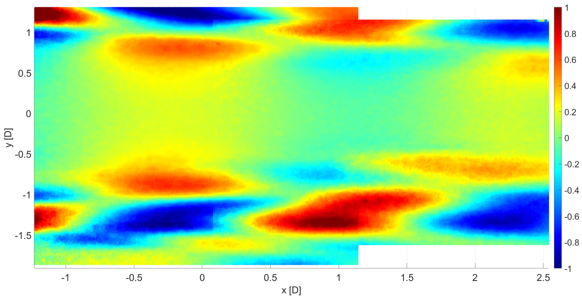

Figure 6.65: No disc, POD mode 3; 6.5 degree amplitude; 12Hz

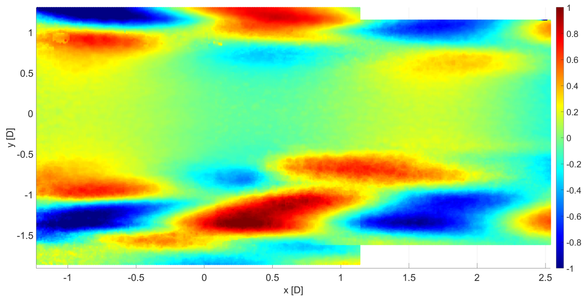

Figure 6.66: No disc, POD mode 4; 6.5 degree amplitude; 12Hz

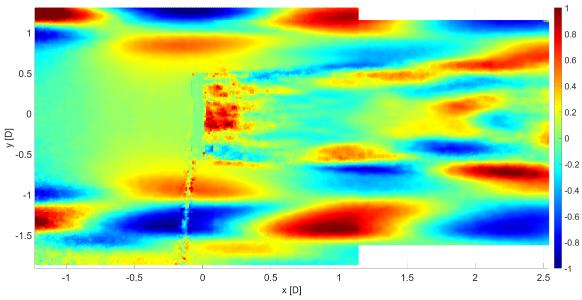

Figure 6.67: Disc 2, POD mode 3; 6.5 degree amplitude; 12Hz

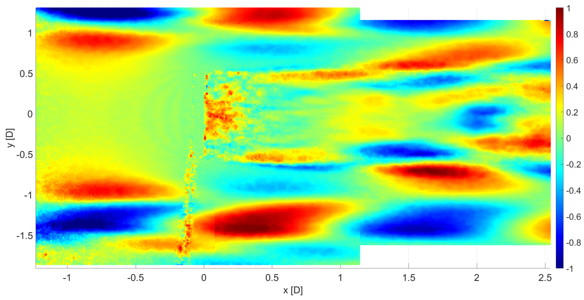

Figure 6.68: Disc 2, POD mode 4; 6.5 degree amplitude; 12Hz

A decrease in gust frequency shows similar large energy peaks in the domain as the smaller gust amplitude case with low frequency (compare figures 6.57 and 6.69). In the case of actuator disc 2, the highest kinetic energy is at the actuator disc's wake boundary (see figure 6.71).

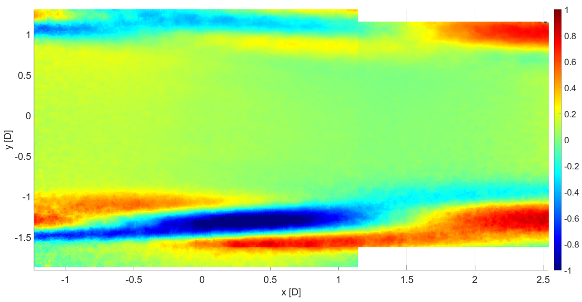

Figure 6.69: No disc, POD mode 3; 6.5 degree amplitude; 6Hz

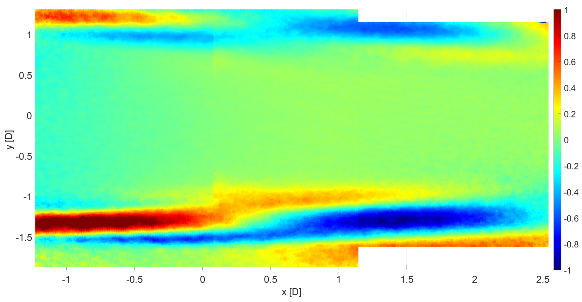

Figure 6.70: No disc, POD mode 4; 6.5 degree amplitude; 6Hz

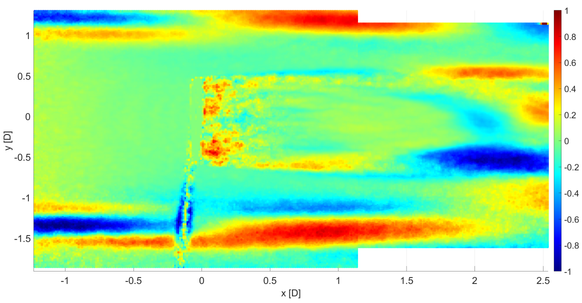

Figure 6.71: Disc 2, POD mode 3; 6.5 degree amplitude; 6Hz

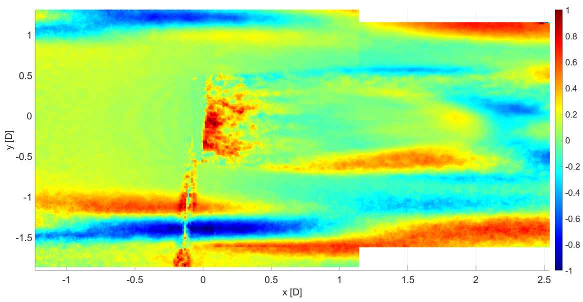

Figure 6.72: Disc 2, POD mode 4; 6.5 degree amplitude; 6Hz

An increase in gust amplitude does not show many changes in comparison to the smaller amplitude cases (compare figures 6.69 and 6.73). The same can be said about the POD with actuator disc 2 (see figures 6.71 and 6.75).

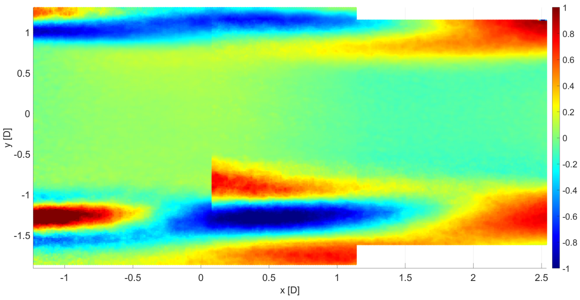

Figure 6.73: No disc, POD mode 3; 10 degree amplitude;6Hz

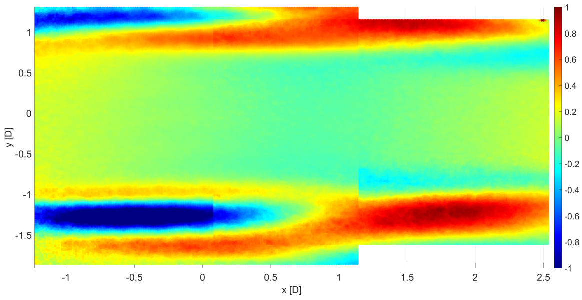

Figure 6.74: No disc, POD mode 4; 10 degree amplitude; 6Hz

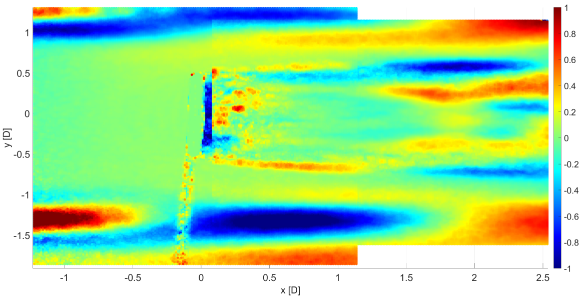

Figure 6.75: Disc 2, POD mode 3; 10 degree amplitude; 6Hz

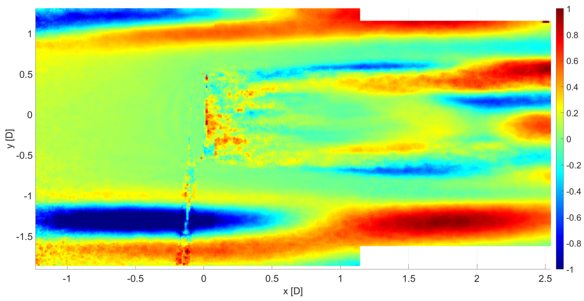

Figure 6.76: Disc 2, POD mode 4; 10 degree amplitude; 6Hz

6.5. Wake expansion and compression

The previous section was about proper orthogonal decomposition. The section investigates the already mentioned wake expansion and compression.

The wake of the actuator disc is expanded and compressed due to the oscillating wakes of the two gust vanes. The expansion and compression of the wake of the actuator disc is only visible on actuator disc 1, and actuator disc 2. The wake expansion and compression is determined at an induction factor of $a = 0.5$. The induction factor is calculated in the wake of the actuator disc. Linear interpolation was used to determine the exact locations with $a = 0.5$. These locations are plotted in figure 6.77.

Figure 6.77 shows the wake expansion and compression of the actuator discs 1 and 2 for small gust vane amplitude, and for both high and low gust frequency. As already mentioned in section 6.2, the wake expansion and compression are at opposite gust vane angles for high gust frequency in comparison to low gust frequency. This is visible if the top left and top right figures of figure 6.77 are compared. In the case of high gust frequency, wake oscillations are visible. The wake is first expanding, before it compresses, and expands again. Thus, the gust frequency has not only an effect on wake expansion at certain gust vane angles, but it also has an influence on wake oscillation. Note that the wake oscillations for low gust frequency are not visible in figure 6.77 because the domain is not large enough. In a much larger domain, wake oscillations for both gust frequencies should be visible.

In comparison to actuator disc 1, actuator disc 2 has a smaller wake expansion (compare figure 6.77 top and bottom). Despite a lower wake expansion, the wake compression is more than the case with actuator disc 1. It is hard to define, but the wake of actuator disc 2 seems to be still being compressed at two-and-a-half disc diameters downstream.

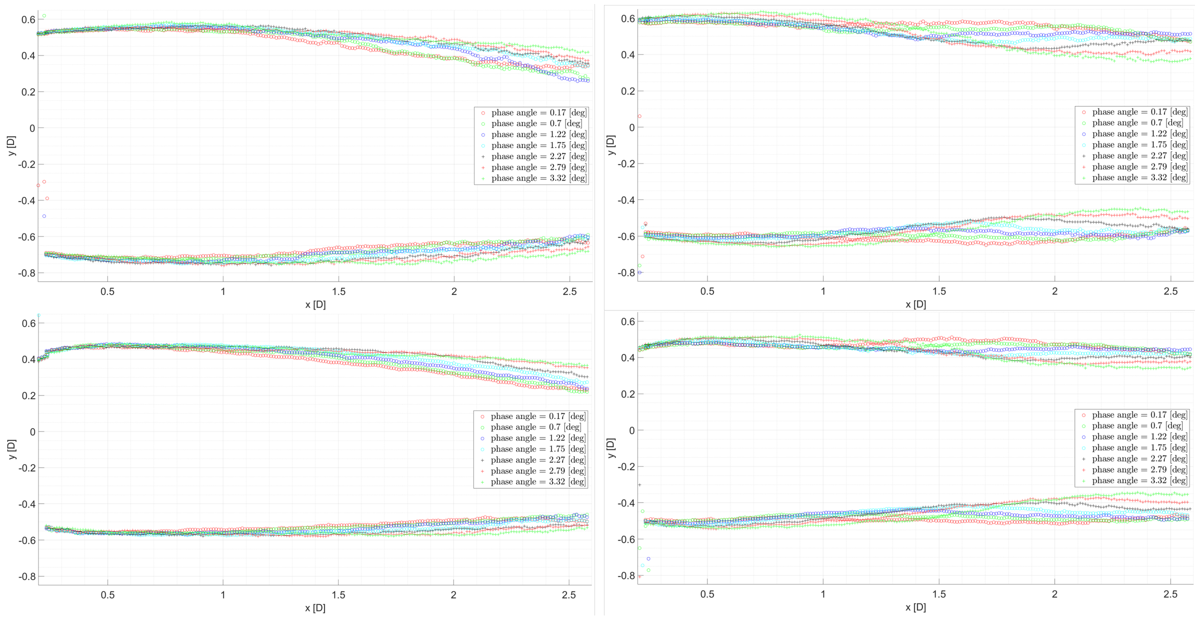

Figure 6.77: Top left disc 1, 5 degree amplitude, 6Hz; top right: disc 1, 5 degree amplitude, 12Hz; bottom left disc 2, 5 degree amplitude, 6Hz; bottom right: disc 2, 5 degree amplitude, 12Hz

The difference in wake expansion is better visible in figures 6.78 and 6.79. The wake expands more for a disc with low porosity.

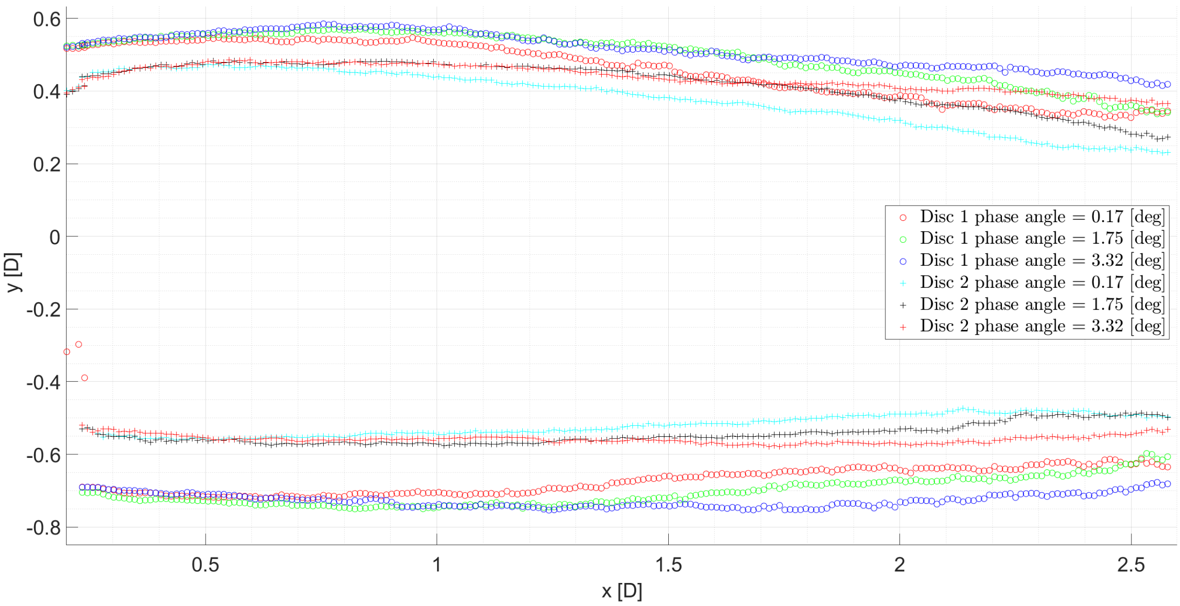

Figure 6.78: Wake expansion comparison between disc 1 and disc 2; 5 degree amplitude, 6Hz

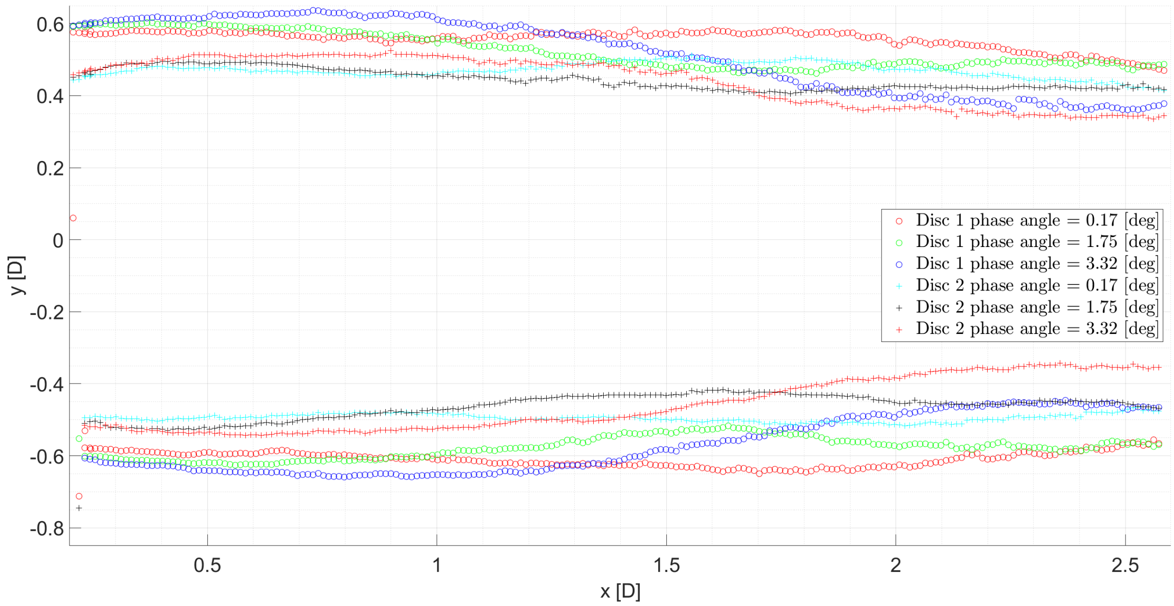

Figure 6.79: Wake expansion comparison between disc 1 and disc 2; 5 degree amplitude, 12Hz

6.6. Upstream induction field

The previous subsection investigated wake expansion and compression. This section investigates the induction field upstream of the actuator disc. As already mentioned before, the induction field upstream of the actuator is fluctuating for Disc 1. The other two discs do not show this behavior. The same procedure has been followed as for wake expansion and compression.

In contrast to wake expansion, where the gust frequency is dominant for wake expansion, the gust amplitude influences the induction field upstream of the actuator disc a lot. This is in contrast to the gust frequency, which seems to have no influence on the induction field upstream of the actuator disc. Both for the 6Hz and the 12Hz cases, the induction field upstream of the actuator disc moves around 0.05 disc diameters in the case of a 5-degree amplitude. This is visible in figure 6.80, where the location change of $a = 0.5$ is plotted in the domain. For the 6.5 degree gust vane amplitude, the induction field moved around .065 disc diameters, while for the 10-degree amplitude, the induction field moved around 0.09 disc diameters.

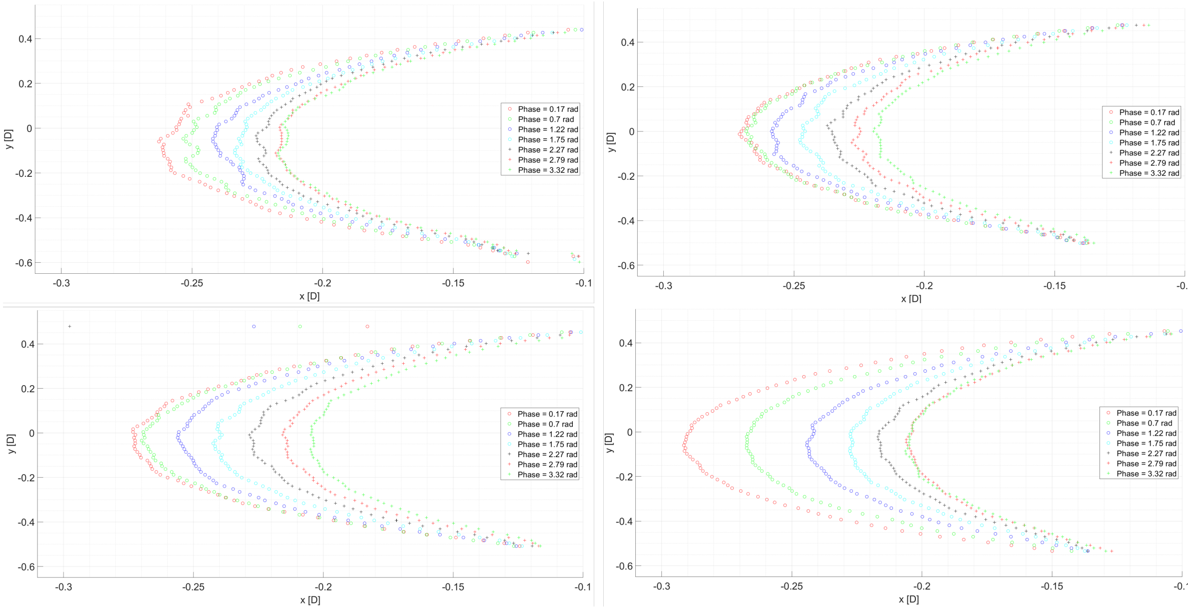

Figure 6.80: Induction changes upstream of the disc; top left: 5 degree amplitude, 6Hz; top right: 5 degree amplitude, 12Hz; bottom left: 6.5 degree amplitude, 12Hz; bottom right: 10 degree amplitude, 6Hz

6.7. Actuator disc thrust

The wake expansion and compression were investigated in the previous two sections. This section is about the calculation of the thrust coefficient. Besides, the calculated values are compared to the literature.

The thrust is calculated using a 1D actuator disc momentum model, used by Lignarolo et al. [32]. The following formulas are used:

$$A = \pi(R_{tip}^2 - R_{root}^2) \tag{6.3}$$

$$a = \frac{\pi}{A}\int_{Rroot}^{R_{tip}}(1 - \frac{u(x)}{u_\infty})rdr \tag{6.4}$$

$$C_T = 4a(1-a) \tag{6.5}$$

The data at $x/D = 0$ is not available due to reflections in the images. Therefore, a linear interpolation is used to calculate the velocity at the location of the actuator disc. Figure 6.81 shows the C_T data in comparison to literature data. It is visible that, in steady cases, the thrust coefficients of disc 1 and disc 2 are quite close to literature data. Disc 3 is a different story. The calculated thrust coefficient is much higher than the literature data. One of the reasons could be that the actuator disc was placed differently in the tower. The discs were placed by hand, which increased the uncertainty for comparison. A very small angle can lead to more or less blockage of the actuator disc. Also, a small angle change is possible in comparison to the lower porosity discs.

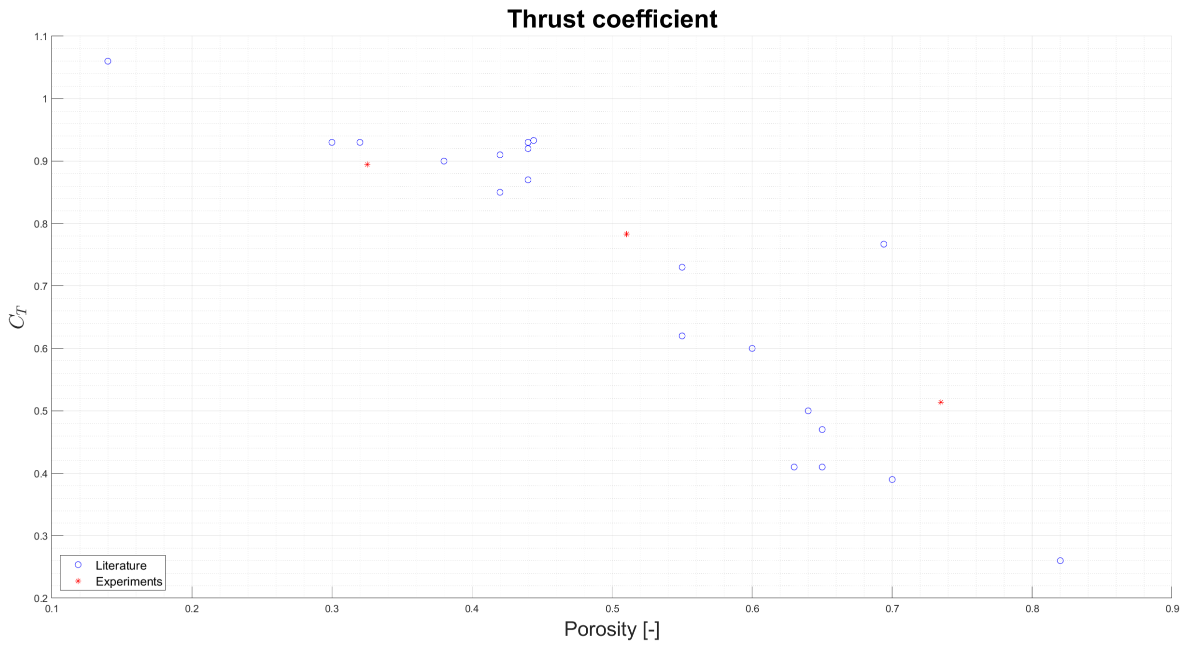

Figure 6.81: Thrust coefficient of the steady cases in comparison to literature [6] [5] [31] [37] [42] [49] [56] [22]

If the C_T-values of the unsteady cases are added, it is visible that the results of disc 1 and disc 2 are still close to the data from literature (see figure 6.82). There is some offset, but that could be due to the gust vane movement. The gust influences the flow, and therefore thrust. The influence of the gust vane movement was also visible in the previous section. Another point is that the thrust coefficient of two cases with disc 3 is relatively high in comparison to the literature, and in comparison to other cases with the same actuator disc. A reason could be the shift of the actuator disc in comparison to the other cases. As already mentioned in 4.2, the actuator disc was removed and placed back in the tower during the experiments. Although the disc was marked, small changes in rotation and/or position could lead to a different velocity field. Since the thrust coefficient depends on the velocity, a different velocity field could lead to a different thrust coefficient.

It should be noted, that the thrust is calculated with a one-dimensional actuator disc model. This model assumes incompressible, steady, one-directional inviscid flow and uniform loading on the disc. In reality, this is not true. The results of this method are not accurate enough to draw strong conclusions.

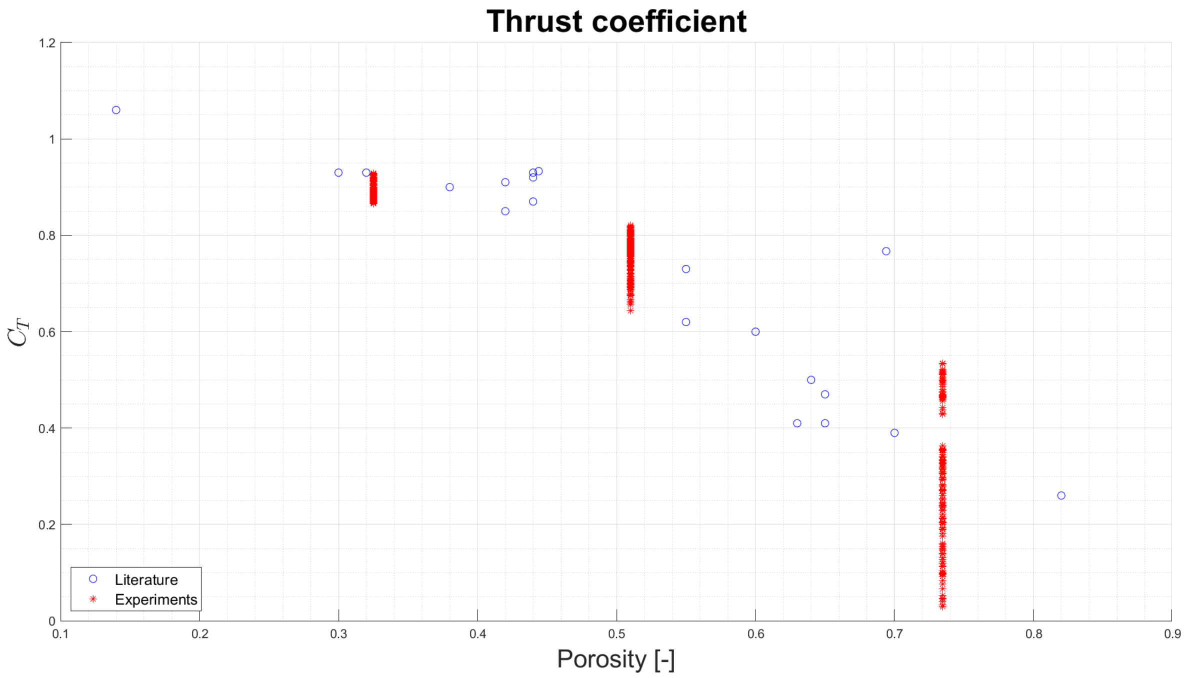

Figure 6.82: The mean thrust coefficients of the unsteady cases in comparison to literature data [6] [5] [31] [37] [42] [49] [56] [22]

In figures 6.83; 6.84, and 6.85 the thrust coefficient is visible including the area in which the thrust could be according to the standard deviation. It should be noted that the standard deviation is high, which results in large differences in calculated thrust coefficients.

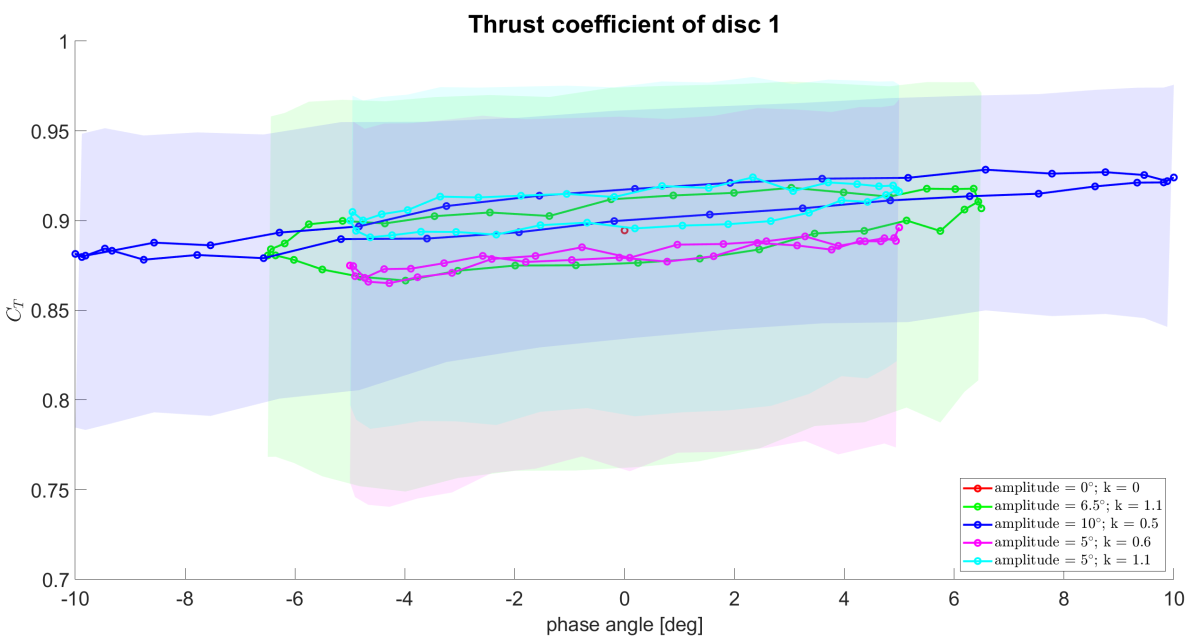

Figure 6.83: Thrust coefficient incudling standard deviation; Disc 1

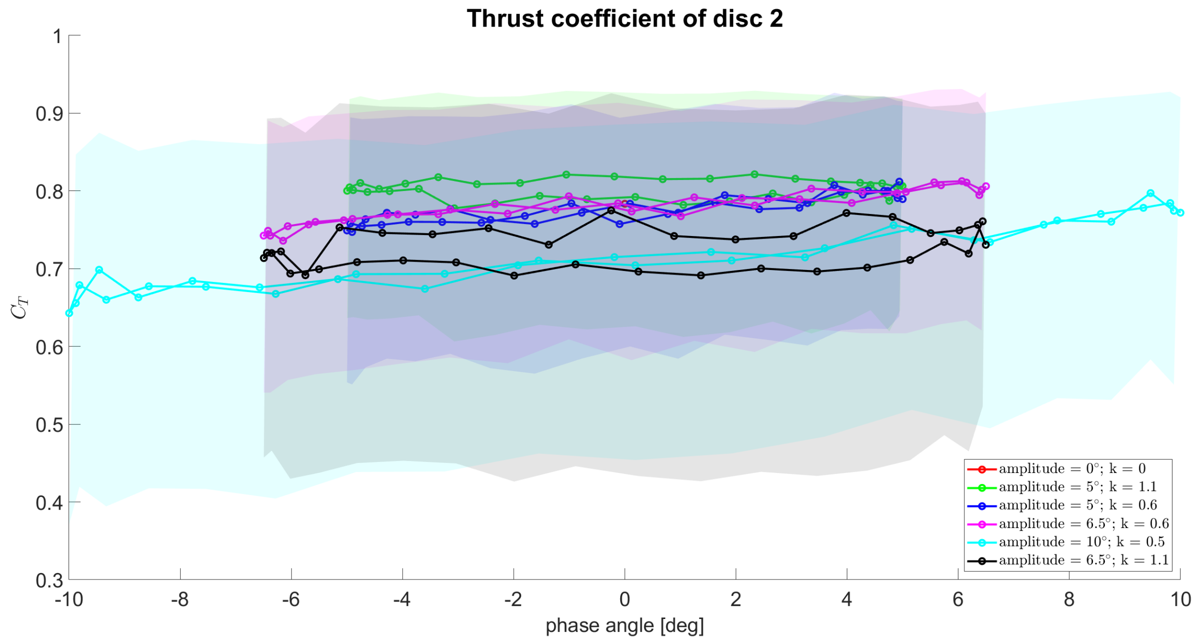

Figure 6.84: Thrust coefficient incudling standard deviation; Disc 2

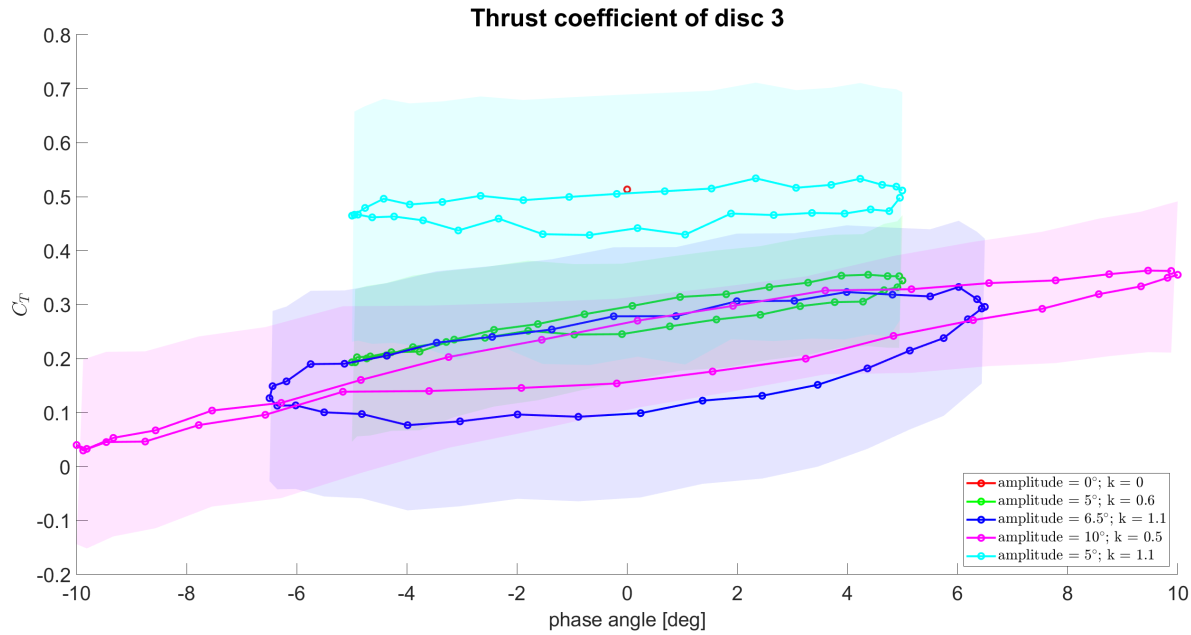

Figure 6.85: Thrust coefficient incudling standard deviation; Disc 3

7

Uncertainty estimation

The results analysed in the previous sections were influenced by experimental errors. The experimental errors were both random and systematic. It is difficult to quantify the errors; a rough estimation of the uncertainties is made in this chapter.

7.1. Uncertainties

One of the largest uncertainties is the placement of the actuator discs. Every time a new actuator disc was placed on the tower, a small uncertainty was added. To reduce the uncertainty, a mark was placed at the disc. However, small shifts of the actuator disc are possible, due to the fact that it was done by hand.

Another uncertainty is the wind tunnel operation. The W-Tunnel motor was set at 420rpm, and runs at that setting. However, changes in air temperature or air pressure have some influence on the velocity measured by the wind tunnel. Between the various runs, the measured density, and measured velocity by the W-Tunnel itself are not constant. However, the measured velocity was probably not equal during every measurement. A different velocity could explain that when the reduced frequency is calculated, four values appear in comparison to the three gust frequencies. Namely, 0; 0.5; 0.6, and 1.1 in comparison to the three gust frequencies of 0Hz; 6Hz, and 12Hz.

During the experiments, the smoke generator was almost empty. An empty smoke machine results in less smoke. Besides, the smoke is not spreading anymore in the tunnel, which results in bad results. The empty smoke machine was noted just after the downstream shift of the second camera.
Besides, the fuel of the smoke machine, the settings of the smoke machine are also an uncertainty in the experiments. The amount of particles in the fluid should be enough to have good results. If there are too many or a too low number of particles, the camera captures too many particles such that DaVis is unable to analyse the results, because the flow field is full of particles. The other option is that there are not enough particles, which results also in that DaVis is unable to calculate the flow field.

Despite the camera shift being measured, and the camera was not touched, except for the movement, the combined cases do not have good results. The flow field has some strange, and not explicable behavior. The idea of using a shifted camera seems nice, but the reality is different. Due to the already mentioned empty smoke machine, the flow was not captured right, which resulted in the flow fields not being combined. Besides the empty smoke machine, also, the already mentioned placement of the actuator discs was done by hand after every actuator disc changed. This also makes it hard to combine the different cases, because the gust vanes are in the same position, but the actuator disc can be shifted a small bit to the left or right.

The wind tunnel is able to measure various parameters, under which the pressure and the temperature. Besides the wind tunnel measurements, the contraction ratio of the gust generator should increase the velocity to a value of $1.1 * U_{W-Tunnel}$. Hereby, $U_{W-Tunnel}$ is the velocity given by the W-tunnel.

However, it seems that this is not entirely true. The non-dimensional velocity is sometimes too often below one, which indicates that the velocity measured by the PIV-system is lower than the velocity should be. However, it is hard to tell what could be the reason for this lower non-dimensional velocity in the flow field. There are several factors of uncertainty here: the measurements of the W-Tunnel; a wrong contraction ratio, or a not well calibrated PIV-system.

7.2. Uncertainty in PIV

Errors in the velocity field are both random and bias errors. Random errors are primarily due to cross-correlation uncertainty. The errors are due to flow velocity fluctuations and variability. Random errors decreased by square root of the number of samples. Uncertainty due to cross-correlation is assumed to be 0.1 pixels. This results in the following formula for the random errors for cross-correlation:

$$random\ error = \frac{\epsilon_u}{\sqrt{N}} \tag{7.1}$$

In this formula, ϵ_u is equal the uncertainty of the cross-correlation, 0.1 pixel. N is the number of samples. For steady load cases, the number of samples was 216 or 432 images. For unsteady load cases, the number of samples was 75 or 76 images. This results in an uncertainty of the mean velocity of 0.48% or 0.68% for steady loading, and 1.15% for unsteady loading.

Another PIV error is peak locking. Peak locking is when the particles are larger than the pixel size. The displacement is then rounded to the nearest integer value. Due to this, errors in velocity measurements occur. A typical displacement uncertainty is between 0.05-0.1 pixels [40]. The second uncertainty is spatial resolution. The spatial resolution is defined as the ratio of window size to spatial wavelength [48]. The value of the spatial wavelength is unknown. Therefore, this uncertainty cannot be estimated. Image matching is typically 0.1 pixel, which gives the same error as the uncertainty of the cross-correlation.

The two cameras were positioned such that there was an overlapped area. In this overlap area, data from the first and second cameras were combined. The manipulation of the data was done in Matlab. There is some uncertainty, because the cameras were not entirely aligned. The second camera was at a small angle. This can also be seen in figure 4.12. Besides, the small camera angle, the lenses were due to the angle not focused in the same way. This results in a slightly different domain size for both cameras. The different domain sizes result in not overlapping points given in the output files of DaVis.

8 Conclusion and recommendations

8.1. Conclusion

The gust is dependent on the frequency and amplitude of the gust generator. Static gust vanes at zero angle of attack yield Von Kárman vortex street. In a steady state, the wake of the actuator disc expandes. The expansion is dependent on the porosity. Consistent with lower porosity, the higher the wake expansion is. At a certain distance downstream, the wake starts to recover to its freestream conditions. The vorticity in the wake of the actuator disc is the strongest, just behind the actuator disc and at the edge of the wake. The edge of the wake is the region with the strongest velocity gradients.

Various gust frequencies and amplitudes were tested. In the wake of the gust vanes, a Von Kárman vortex street is created. This vortex street is oscillating due to the moving gust vanes. In between the wake of the gust vanes, the velocity is increased or decreased depending on the gust vane angle. The area between the two gust vanes is decreased, which increases the velocity between the wakes, while the velocity at the outside of the domain is decreased and vice versa. The gust frequency and amplitude are responsible for the region the velocity increased. The larger the gust amplitude or the higher the gust frequency, the higher the velocity becomes in between the wakes.

The unsteady cases with an actuator disc show that the porosity has an influence on the wake expansion and on the velocity in the wake of the actuator disc. The wake is expanded more for lower porosity, while the wake compression is less dependent on porosity. The gust frequency has a higher influence on the wake of the actuator disc than the gust amplitude. For higher gust frequencies, the wake shows sinusoidal oscillations in the captured area of the experiments. For lower gust frequency, this is not visible.

The Pearson correlation coefficient shows the correlation between the incoming velocity and the velocity in the flow field. The gust increases or decreases the velocity between the gust vane wakes. The correlation between the incoming flow with the flow field shows similarities between the various gust frequencies and gust amplitudes. The flow field for a no-disc case shows strong correlation, no correlation and strong correlation. For higher frequencies, these correlated and non-correlated areas are smaller. Moreover, for higher gust frequency, more correlated and non-correlated regions are shown in the captured flow field. Thus, the Pearson correlation coefficient shows the change in velocity in the domain due to the gust. For actuator discs, the wake shows similar behavior of correlated and non-correlated regions.

The Proper Orthogonal Decomposition shows high energy in the wake of the gust vanes. This energy could represent the Von Kárman vortex street. In the wake of the actuator disc, the strongest energy is visible at the edges of the wake. Therefore, these high energy regions represent the tip vortices.

The thrust coefficient of the steady cases is close to literature data. The thrust coefficients for the unsteady cases are fluctuating around the thrust coefficient of the steady cases.

The uncertainty effect is increased, which leads to a high standard deviation of the data. A large standard deviation could lead to larger errors. An uncertainty analysis of the velocity data showed that the data converge very fast.

8.2. Recommendations

The first limitation was a large standard deviation of the velocity. A larger standard deviation can result in large fluctuations between the results. The second limitation is the PIV set-up. Despite the flow field being visible from one disc diameter upstream up to two-and-a-half disc diameters downstream, the laser beam was at its limits.

The first recommendation is to do the experiment with a larger flow field. Hereby, it is recommended to use lenses with a large capture area to reduce the negative influences of the overlapping regions of the cameras. In a larger downstream area, the sinusoidal oscillations of the wake of the actuator disc become visible at lower frequencies.

The second recommendation is that in the next experiment, the actuator disc is only removed after all trials are done. That means that the mounted actuator disc is tested for various gust frequencies and gust amplitudes before the actuator disc is replaced by another. This reduces the effect of small changes in actuator disc positions, and/or actuator disc rotations.

The third recommendation is to see if a low-speed laser and low-speed camera system can be used in further experiments. The low-speed laser is able to a much wider laser beam, which increases the flow field length. A larger flow field reduces the requirement for a shifted camera.

The fourth recommendation is to use a balance to measure the forces in the flow direction. If the balance was used, the thrust coefficients calculated could be verified with the measurements of the balance system.

The number of images captured by the cameras could be increased to decrease the uncertainty of the mean. The standard deviation is large, which means that the data is now wildly spread around the mean. With more images, the mean value becomes stronger, and the convergence of the data becomes better.

References

[1] -. *IEA Wind Task 30*. URL: https://iea-wind.org/task30/. (accessed: 15.11.2021).

[2] U.S. Energy Information Administration. *Wind explained History of wind power*. URL: https://www.eia.gov/energyexplained/wind/history-of-wind-power.php. (accessed: 17.01.2022).

[3] J.F. Ainslie. "Calculating the flowfield in the wake of wind turbines". In: *Journal of Wind Engineering and Industrial Aerodynamics* 11 (10 2018).

[4] A. Arabgolarcheh. "Modeling of near wake characteristics in floating offshore wind turbines using an actuator line method". In: *Renewable energy* 185 (2022), pp. 871–887.

[5] S. Aubrun. "Physical modelling of the far wake from wind turbines. Application to wind turbine interactions". In: *Proceedings of the European Wind Energy Conference*. Milan, Italy, 2007.

[6] S. Aubrun et al. "Wind turbine wake properties: Comparison between a non-rotating simplified wind turbine model and a rotating model". In: *Journal of Wind Engineering and Industrial Aerodynamics* 120 (2013), pp. 1–8.

[7] F. Berger and M. Kühn. "Experimental investigation of dynamic inflow effects with a scaled wind turbine in a controlled wind tunnel environment". In: *Journal of Physics: Conference Series* 1037 (5 2018).

[8] Frederik Berger et al. "Experimental analysis of the dynamic inflow effect due to coherent gusts". In: *Wind Energy Science* (2022). DOI: https://doi.org/10.5194/wes-2022-2.

[9] R. Braunbehrens and A. Segalini. "A statistical model for wake meandering behind wind turbines". In: *Journal of Wind Engineering and Industrial Aerodynamics* 193 (2019).

[10] F. Campagnolo et al. "Wind tunnel testing of wake steering with dynamic wind direction changes". In: *Wind Energy Science* 5 (4 2020), pp. 1273–1295.

[11] directoraat-generaal Communicatie. *Een Europese Green Deal*. URL: https://ec.europa.eu/info/strategy/priorities-2019-2024/european-green-deal_nl. (accessed: 17.01.2022).

[12] AWEP Facilities. *W-Tunnel*. URL: https://www.tudelft.nl/lr/organisatie/afdelingen/aerodynamics-wind-energy-flight-performance-and-propulsion/facilities/low-speed-wind-tunnels/w-tunnel. (accessed: 22.11.2021).

[13] C. Ferreira et al. "Dynamic inflow model for a floating horizontal axis wind turbine in surge motion". In: *Wind energy Science* 7 (2022), pp. 469–485. DOI: https://doi.org/10.5194/wes-7-469-2022.

[14] R. E. Froude. "On the Part Played in Propulsion by Difference in Pressure. Transaction of the Institute of Naval Architects". In: 30 (1889), pp. 390–405.

[15] S. Gambuzza. "Tailoring wind turbine wake models to incoming free-stream turbulence". In: *Journal of Physics: Conference Series* 2265 (2022).

[16] J. Geertsen. "Development of a Gust Generator for a Low Speed Wind Tunnel". In: *Master thesis* (2020).

[17] H.Snel and J.G.Schepers. "Joint investigation of dynamic inflow effects and implementation of an engineering method". In: *ECN Publications* (2017). URL: https://publications.ecn.nl/E/1995/ECN-C--94-107.

[18] O.L. Hansen. *Aerodynamics of Wind Turbines*. Earthscan, 2008. ISBN: 978-1-84407-438-9.

[19] R. J. Hearst and R. Pavole. "The effect of active grid initial conditions on high Reynolds number turbulence". In: *Experiments in Fluids* 56 (2015). DOI: DOI10.1007/s00348-015-2052-1.

[20] Philip Holmes, John L. Lumley, and Gal Berkooz. *Turbulence, Coherent Structures, Dynamical Systems and Symmetry*. Cambridge Monographs on Mechanics. Cambridge University Press, 1996. DOI: 10.1017/CBO9780511622700.

[21] V. Hong. “Analysis of an Actuator Disc under Unsteady Loading”. In: *Thesis* (2015). URL: https://repository.tudelft.nl/islandora/object/uuid%3Ac04ebfb6-4fd8-4856-830d-e26061c25e4c?collection=education.

[22] M. Huang et al. “Wake scaling of actuator discs in different aspect ratios”. In: *Renewable Energy* 183 (2022), pp. 866–876.

[23] K. Kaur. “Experimental Analysis of an Actuator Disk under cyclic unsteady loading”. In: *Thesis* (2017).

[24] P. Knebel, A. Kittel, and J. Peinke. “Atmospheric wind field conditions generated by active grids”. In: *Experiments in Fluids* 51 (2011), pp. 471–481. DOI: DOI10.1007/s00348-011-1056-8.

[25] T.T.B. Wester J. Kraus et al. “How to Design a 2D Active Grid for Dynamic Inflow Modulation”. In: *Flow, Turbulence and Combstion* 108 (2022), pp. 955–972. DOI: 10.1007/s10494-021-00312-8.

[26] C. Krishnaswami. “Experimental Analysis of Near andTransitional Wind Turbine Wake Using Stereo Particle Image Velocimetry”. In: *Thesis* (2013). URL: https://repository.tudelft.nl/islandora/object/uuid%3A9d61795b-1d2f-4021-9860-b796e7d1173b?collection=education.

[27] LaVision. *DaVis – Software Solution for Intelligent Imaging*. URL: https://www.lavision.de/en/products/davis-software/. (accessed: 25.04.2022).

[28] Qing’an Li et al. “Experimental and numerical investigation of the effect of turbulent inflow on a Horizontal Axis Wind Turbine (part II: Wake characteristics)”. In: *Energy* 113 (2016), pp. 1304–1315.

[29] Qing’an Li et al. “Experimental investigations of boundary layer impact on the airfoil aerodynamic forces of Horizontal Axis Wind Turbine in turbulent inflows”. In: *Energy* 135 (2017), pp. 799–810.

[30] Zhaobin Li and Xiaolei Yang. “Evaluation of Actuator Disk Model Relative to Actuator Surface Model for Predicting Utility-Scale Wind Turbine Wakes”. In: *Energies* 13 (14 2020). DOI: https://doi.org/10.3390/en13143574.

[31] L Lignarolo. “Tip-vortex instability and turbulent mixing in wind-turbine wakes”. In: *Journal of Fluid Mechanics* (2015). URL: https://www.researchgate.net/publication/282175655_Tip-vortex_instability_and_turbulent_mixing_in_wind-turbine_wakes.

[32] L. E. M. Lignarolo et al. “Experimental comparison of a wind-turbine and of an actuator-disc wake”. In: *Journal of Renewable and Sustainable Energy* (2016). DOI: ttp://dx.doi.org/10.1063/1.4941926.

[33] H. Makita. “Realization of a large-scale turbulence field in a small wind tunnel”. In: *Fluid Dynamic Research* 8 (1-4 1991).

[34] Pedro Martinez-Vazquez. *How to calculate wind turbulence intensity?* URL: https://www.researchgate.net/post/How_to_calculate_wind_turbulence_intensity. (accessed: 20.09.2022).

[35] K F McAnulty. *Proceedings of the fourth IEA symposium on the aerodynamics of wind turbines*. Jan. 1991.

[36] D. Medici. “Effect of wind turbine surge motion on rotor thrust and induced velocity”. In: *Wind Energy* 11 (10 2018).

[37] D. Medici and P. Hendrik Alfredsson. “Wind Turbine Near Wakes and Comparisons to the Wake Behind a Disc”. In: *43rd AIAA Aerospace Sciences Meeting and Exhibit - Meeting Papers*. Stockholm, Sweden, 2005, pp. 15593–15604.

[38] Christoph Mertens. *PIV high speed acquisition system*. URL: https://wiki.tudelft.nl/bin/view/Organisation/LR/WikiAero/ExperimentalWiki/PIVsystemsWiki/PhotronFastcamWiki. (accessed: 29.07.2022).

[39] L. Neuhaus et al. “Exploring the capabilities of active grids”. In: *Experiments in Fluids* 62 (2021). DOI: https://doi.org/10.1007/s00348-021-03224-5.

[40] E. F. J. Overmars et al. “Bias errors in PIV : the pixel locking effect revisited”. In: 2010.

[41] D.M. Pitt; D.A. Peters. “Theoretical prediction of dynamic-in ow derivatives”. In: *Ninth European Rotorcraft forum* (1981), p. 55.

[42] Fabio Pierella. “Wind tunnel investigation on the effect of the turbine tower on wind turbines wake symmetry”. In: *Wind energy* 20 (10 2017), pp. 1753–1769. DOI: https://doi.org/10.1002/we.2120.

[43] G. Raimund Pirrung and H. Aagaard Madsen. "Dynamic inflow effects in measurements and high-fidelity computations". In: *Wind energy* 3 (2018), pp. 545–551. DOI: https://doi.org/10.5194/wes-3-545-2018.

[44] M. Raffel et al. *Particle Image Velocimetry*. Springer, 2021. ISBN: 978-3-319-68851-0.

[45] Huilai Ren et al. "Actuator Disc Approach of Wind Turbine Wake Simulation Considering Balance of Turbulence Kinetic Energy". In: *Energies* 12 (1 2019). DOI: https://doi.org/10.3390/en12010016.

[46] B. Sanderse. "Aerodynamics of wind turbine wakes". In: *PHD* (2009). URL: https://www.researchgate.net/publication/242726502_Aerodynamics_of_wind_turbine_wakes_Literature_review.

[47] J.G. Schepers. "Engineering models in wind energy aerodynamics: Development, implementation and analysis using dedicated aerodynamic measurements". In: *PHD* (2012). URL: https://repository.tudelft.nl/islandora/object/uuid%3A92123c07-cc12-4945-973f-103bd744ec87?collection=research.

[48] F. F. J. Schrijer et al. "Experimental Capsule Afterbody Flow Investigation". In: *6th European Symposium on Aerothermodynamics for Space Vehicles*. Ed. by H. Lacoste and L. Ouwehand. Vol. 659. ESA Special Publication. Jan. 2009, 98, p. 98.

[49] P. M. Sforza. "Three-Dimensional Wakes of Simulated Wind Turbines". In: *AIAA Journal* 19 (1981). DOI: https://doi.org/10.2514/3.60049.

[50] S. E. Smith et al. "Dynamic effects of inertial particles on the wake recovery of a model wind turbine". In: *Renewable Energy* 164 (2021), pp. 346–361.

[51] H. Snel. "Investigation and modelling of dynamic inflow effects". In: *ECWEC Conference* (1993).

[52] Techimagine. *Photron FASTCAM SA1.1*. URL: https://www.techimaging.com/products/legacy/legacy-high-speed/product/photron-fastcam-sa1-1. (accessed: 25.04.2022).

[53] J. de Vaal. "Effect of wind turbine surge motion on rotor thrust and induced velocity". In: *Wind Energy* 17 (2014), pp. 105–121.

[54] J. Weiss. *A Tutorial on the Porper Orthogonal Decomposition*. 2019. DOI: ttps://doi.org/10.14279/depositonce-8512.

[55] Zhenlong Wu et al. "Insights into airfoil response to sinusoidal gusty inflow by oscillating vanes". In: *Physics of Fluids* 32 (12 2020).

[56] W. Yu, C. Ferreira, and G. A. M. van Kuik. "The dynamic wake of an actuator disc undergoing transient load: A numerical and experimental study". In: *Renewable energy* 132 (2019), pp. 1402–1414. DOI: https://doi.org/10.1016/j.renene.2018.09.013.

[57] W. Yu et al. "Experimental analysis on the dynamic wake of an actuator disc undergoing transient loads". In: *Experiments in Fluids* 58 (2017). DOI: https://doi.org/10.1017/jfm.2018.275.

[58] W. Yu et al. "New dynamic-inflow engineering models based on linear and nonlinear actuator disc vortex models". In: *Wind energy* 22 (11 2019), pp. 1433–1450. DOI: https://doi.org/10.1002/we.2380.

[59] W. Yu et al. "Validation of engineering dynamic inflow models by experimental and numerical approaches". In: *Journal of Physics* 753 (2 2016).

A

Appendix A

In this appendix, some graphs of the non-dimensional velocity versus y are visible. The main part of this appendix is to show that the velocity is changing not only due to the movement of the gust vanes, but the actuator disc also has an influence on the velocity field upstream and downstream of the actuator disc.

A.1. Steady cases

For the steady cases, in which there is no gust, the graphs look to be the same. The velocity in the wake of the actuator disc seems to be constant, while the velocity in the wake of the actuator disc is much smaller. For the cases with a disc, the wake of the actuator disc is visible. The velocity in the wake is much smaller than the freestream velocity. Another thing which is visible is the influence of the three different actuator discs. Disc 1, which has the lowest porosity, has a much stronger influence on velocity than discs with higher porosity. In case of actuator disc 1, the velocity in the wake of the actuator disc reduces to zero or becomes negative. For disc 2, the velocity in the wake of the actuator disc also becomes small, but the velocity stays positive. Disc 3 has a slightly different profile, due to the larger holes in the disc. Therefore, the velocity in the wake of the actuator disc has a kind of sinusoidal form.

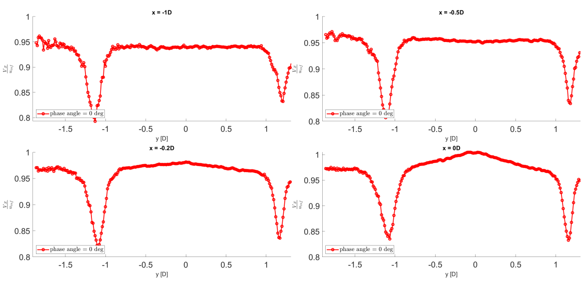

Figure A.1: No disc; Dimensionless velocity versus y [D]

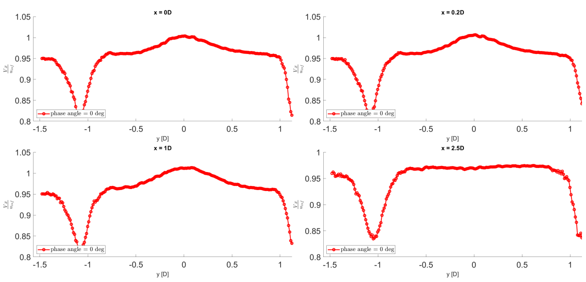

Figure A.2: No disc; Dimensionless velocity versus y [D]

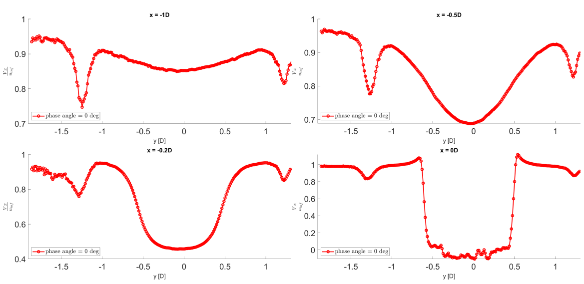

Figure A.3: Disc 1; Dimensionless velocity versus y [D]

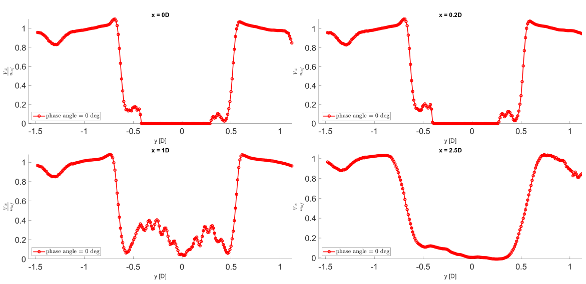

Figure A.4: Disc 1; Dimensionless velocity versus y [D]

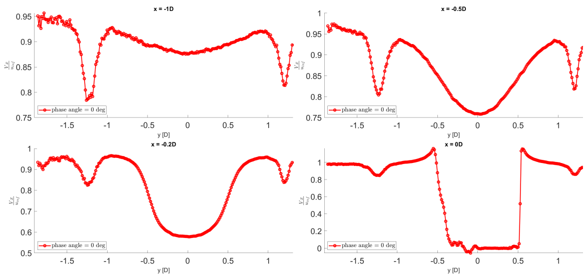

Figure A.5: Disc 2; Dimensionless velocity versus y [D]

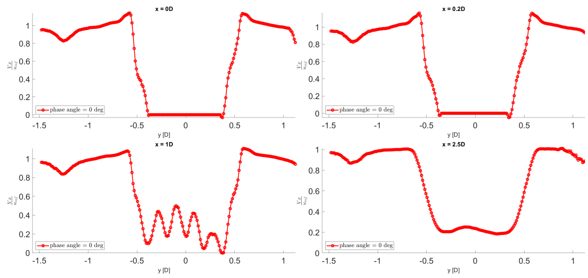

Figure A.6: Disc 2; Dimensionless velocity versus y [D]

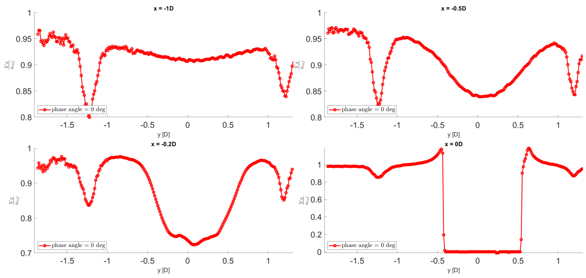

Figure A.7: Disc 3; Dimensionless velocity versus y [D]

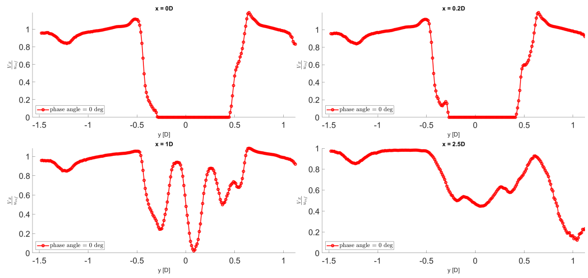

Figure A.8: Disc 3; Dimensionless velocity versus y [D]

A.2. Unsteady cases

In cases where the gust vane is moving, the wake of the gust vanes is still visible in the graphs. However, due to the moving gust vanes, the velocity distribution on the gust vane is changing. Therefore, the velocity in the wake of the gust vanes is also changing. Moreover, the wake of the gust vane is fluctuating towards the actuator disc before moving back. Another thing which is visible is that the velocity between the gust vane is also changing with respect to the freestream velocity. If the velocity is increased between the two gust vanes, the velocity outside of the gust vanes is lower and vice versa. In cases of an actuator disc, the velocity is only increased in the area between the wake of the actuator disc and the wake of the gust vanes.

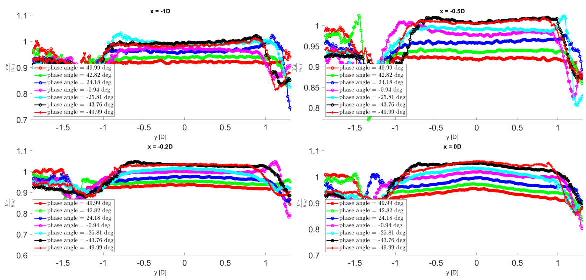

Figure A.9: No disc; 5 degree amplitude, 6Hz; Dimensionless velocity versus y [D]

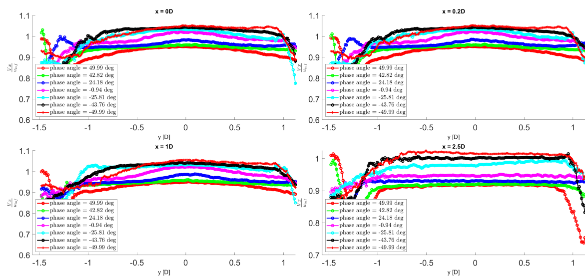

Figure A.10: No disc; 5 degree amplitude, 6Hz; Dimensionless velocity versus y [D]

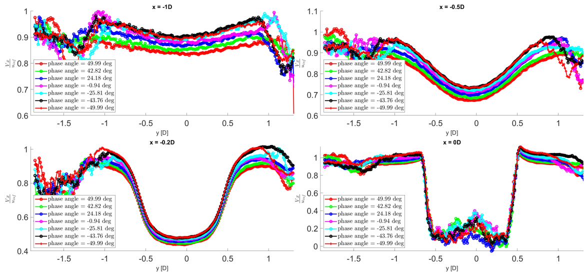

Figure A.11: Disc 1; 5 degree amplitude, 6Hz; Dimensionless velocity versus y [D]

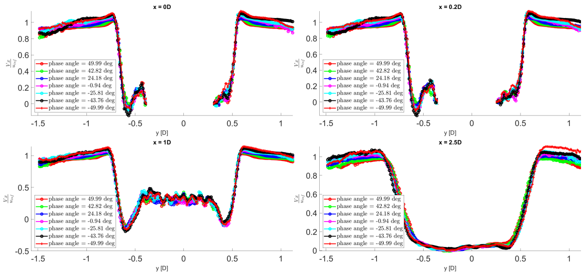

Figure A.12: Disc 1; 5 degree amplitude, 6Hz; Dimensionless velocity versus y [D]

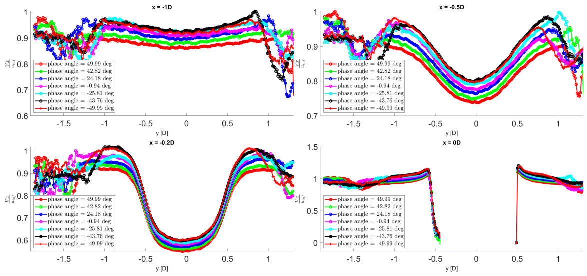

Figure A.13: Disc 2; 5 degree amplitude, 6Hz; Dimensionless velocity versus y [D]

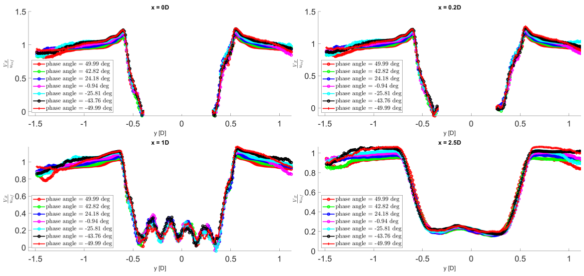

Figure A.14: Disc 2; 5 degree amplitude, 6Hz; Dimensionless velocity versus y [D]

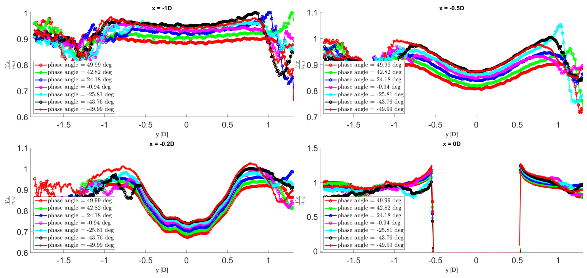

Figure A.15: Disc 3; 5 degree amplitude, 6Hz; Dimensionless velocity versus y [D]

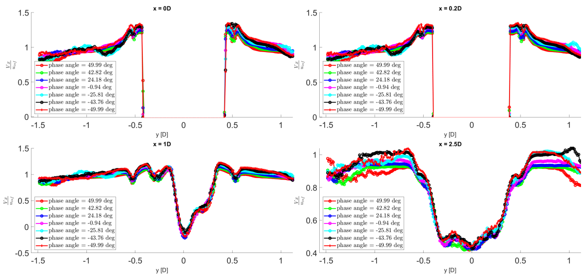

Figure A.16: Disc 3; 5 degree amplitude, 6Hz; Dimensionless velocity versus y [D]

Changing the gust amplitude or the gust frequency changes the velocity profile too. Due to the stronger wake of the gust vanes, the expansion and compression of the wake of the actuator disc is changed. Therefore, the velocity profile also changes.

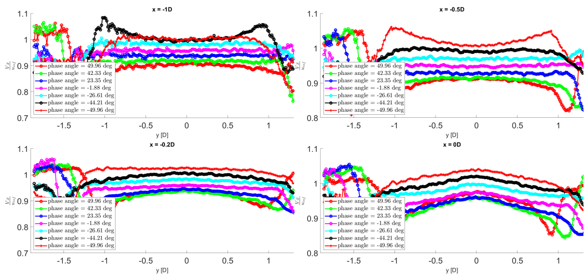

Figure A.17: No disc; 5 degree amplitude, 12Hz; Dimensionless velocity versus y [D]

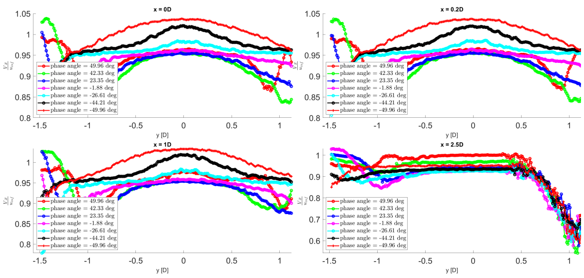

Figure A.18: No disc; 5 degree amplitude, 12Hz; Dimensionless velocity versus y [D]

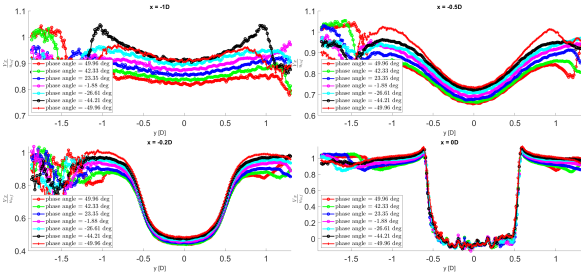

Figure A.19: Disc 1; 5 degree amplitude, 12Hz; Dimensionless velocity versus y [D]

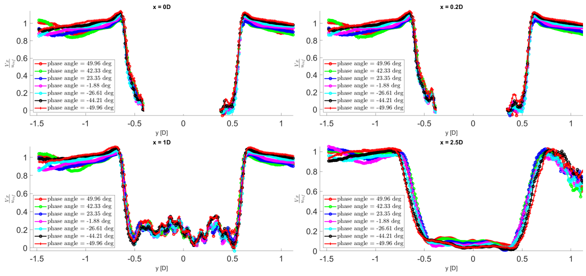

Figure A.20: Disc 1; 5 degree amplitude, 12Hz; Dimensionless velocity versus y [D]

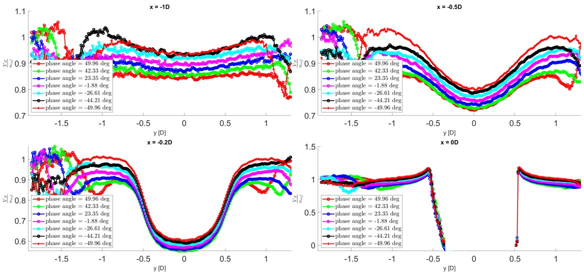

Figure A.21: Disc 2; 5 degree amplitude, 12Hz; Dimensionless velocity versus y [D]

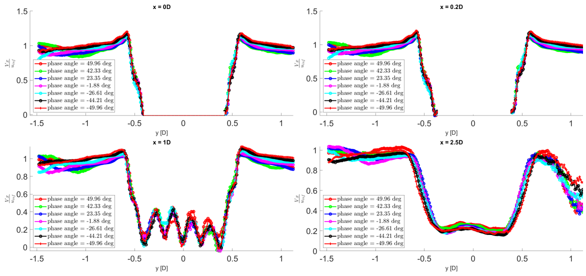

Figure A.22: Disc 2; 5 degree amplitude, 12Hz; Dimensionless velocity versus y [D]

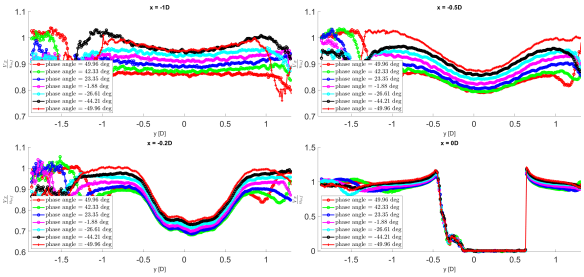

Figure A.23: Disc 3; 5 degree amplitude, 12Hz; Dimensionless velocity versus y [D]

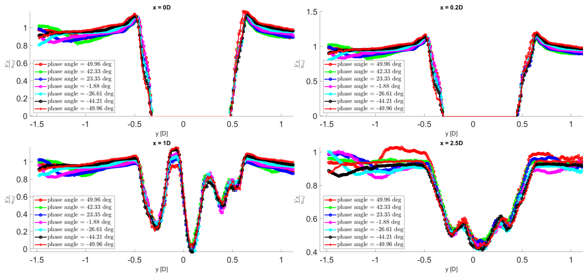

Figure A.24: Disc 3; 5 degree amplitude, 12Hz; Dimensionless velocity versus y [D]

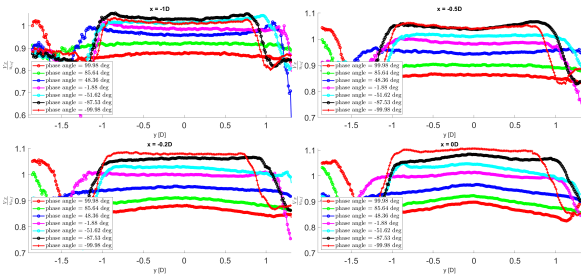

Figure A.25: No disc; 10 degree amplitude, 6Hz; Dimensionless velocity versus y [D]

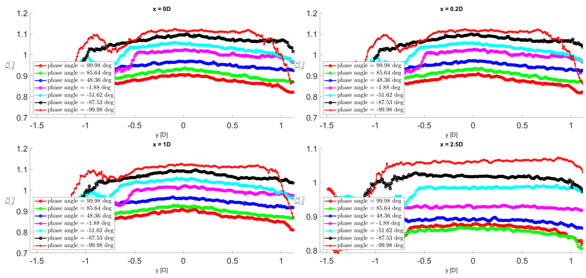

Figure A.26: No disc; 10 degree amplitude, 6Hz; Dimensionless velocity versus y [D]

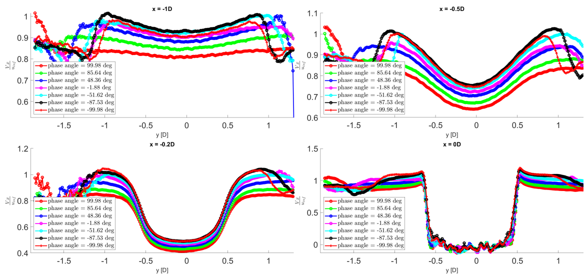

Figure A.27: Disc 1; 10 degree amplitude, 6Hz; Dimensionless velocity versus y [D]

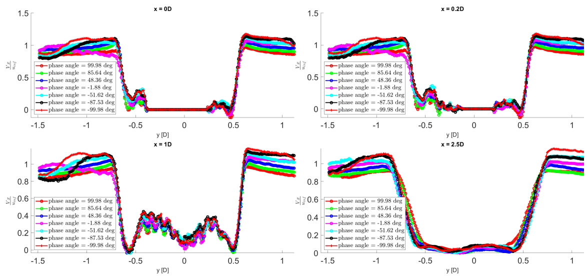

Figure A.28: Disc 1; 10 degree amplitude, 6Hz; Dimensionless velocity versus y [D]

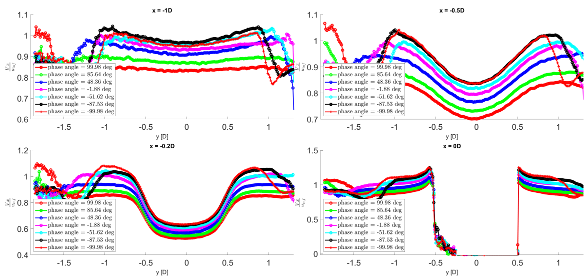

Figure A.29: Disc 2; 10 degree amplitude, 6Hz; Dimensionless velocity versus y [D]

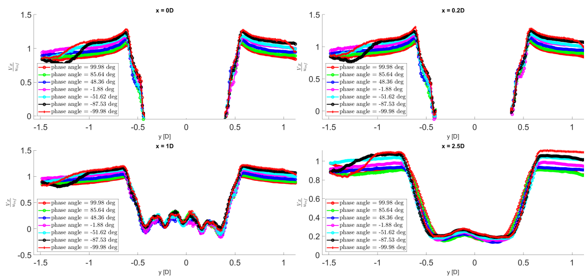

Figure A.30: Disc 2; 10 degree amplitude, 6Hz; Dimensionless velocity versus y [D]

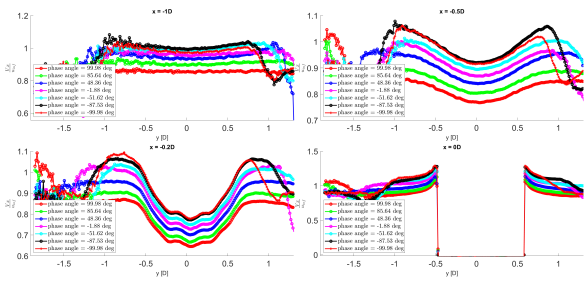

Figure A.31: Disc 3; 10 degree amplitude, 6Hz; Dimensionless velocity versus y [D]

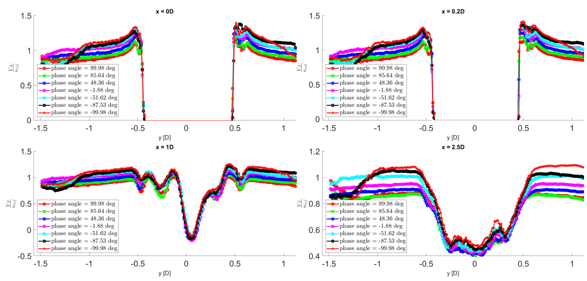

Figure A.32: Disc 3; 10 degree amplitude, 6Hz; Dimensionless velocity versus y [D]

B
Appendix B

In this appendix, the steady gust vane flow field is shown in detail. At nine different locations in the captured area of the first camera and at nine locations in the captured area of the second camera, the velocity field is shown versus y. The nine locations were randomly selected by Matlab, using the randi function.

It is visible that the flow field does not change in the case without a disc. The velocity in between the two gust vane wakes is almost constant. Also, the velocity in the gust vane wake is much smaller than the freestream velocity, but it does not change much. When an actuator disc is added, the velocity field changes. In the wake of the actuator disc, the velocity is much lower than in the freestream, due to the extraction of energy by the actuator disc.

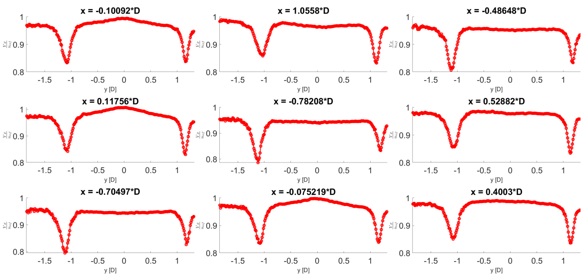

Figure B.1: No disc; Dimensionless velocity versus y [D]

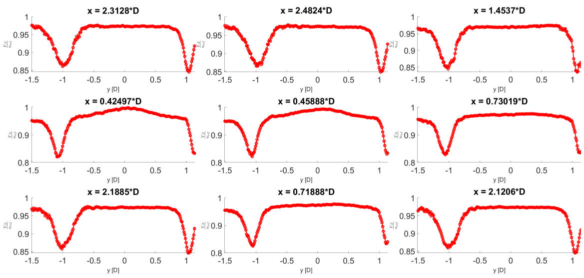

Figure B.2: No disc; Dimensionless velocity versus y [D]

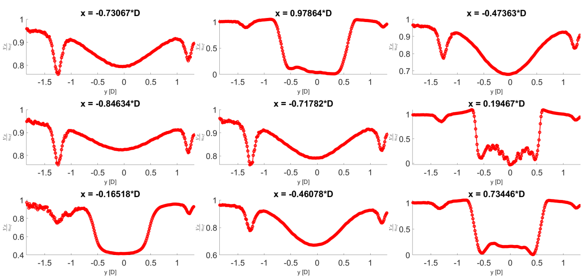

Figure B.3: Disc 1; Dimensionless velocity versus y [D]

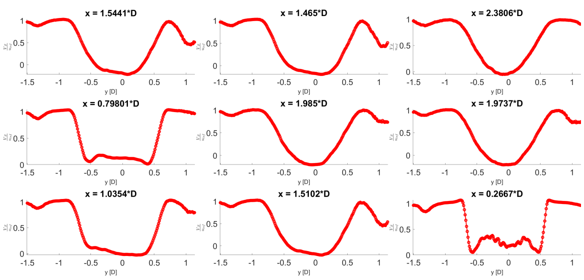

Figure B.4: Disc 1; Dimensionless velocity versus y [D]

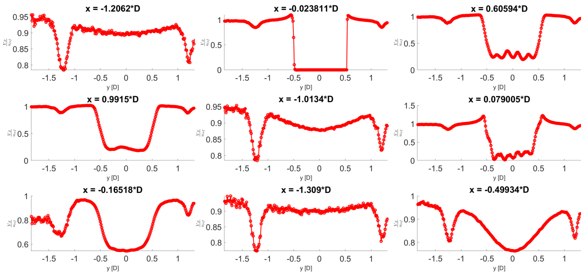

Figure B.5: Disc 2; Dimensionless velocity versus y [D]

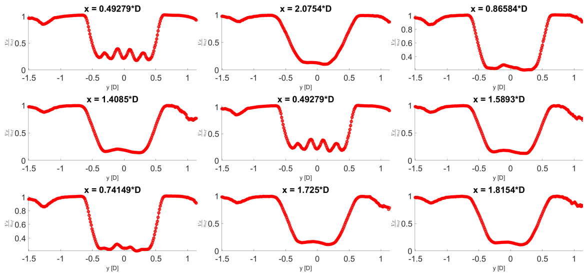

Figure B.6: Disc 2; Dimensionless velocity versus y [D]

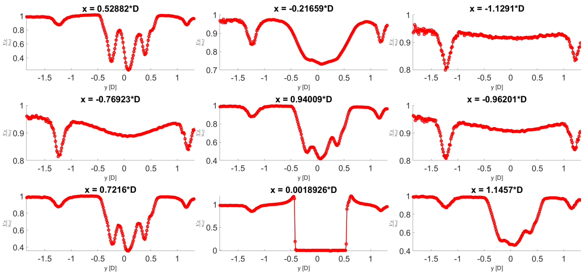

Figure B.7: Disc 3; Dimensionless velocity versus y [D]

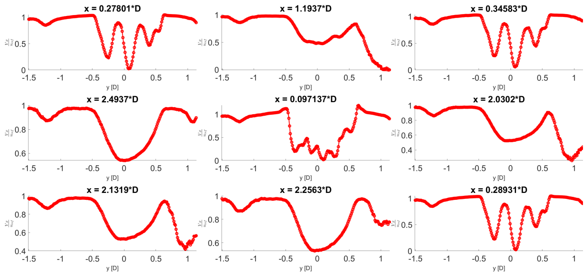

Figure B.8: Disc 3; Dimensionless velocity versus y [D]

Appendix C

This appendix shows the fluctuations in the velocity field of the steady cases. Besides the fluctuations in the flow field, the convergence of the cases is shown.

C.1. Velocity fluctuations steady cases

The figures in this appendix show the large fluctuations in the flow field of the steady cases. The steady cases are the four cases with the three different actuator discs, and the case without an actuator disc.

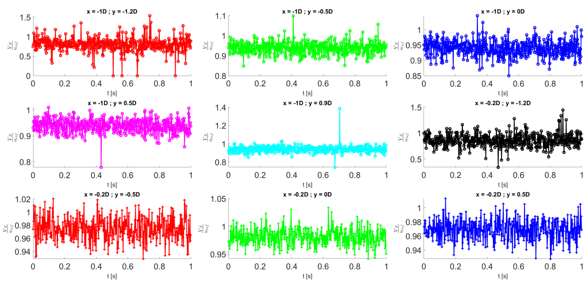

Figure C.1: No disc; steady case velocity fluctuations camera 1 part 1

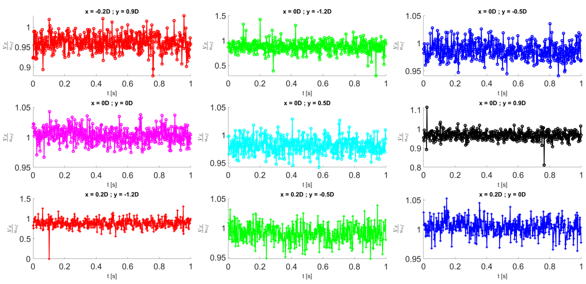

Figure C.2: No disc; steady case velocity fluctuations camera 1 part 2

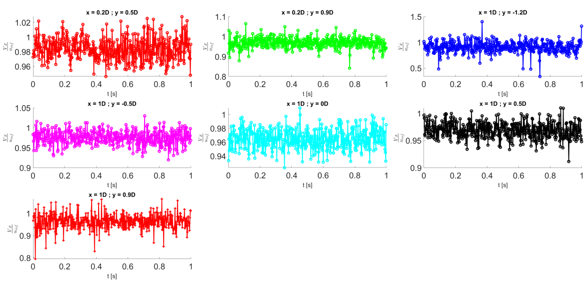

Figure C.3: No disc; steady case velocity fluctuations camera 1 part 3

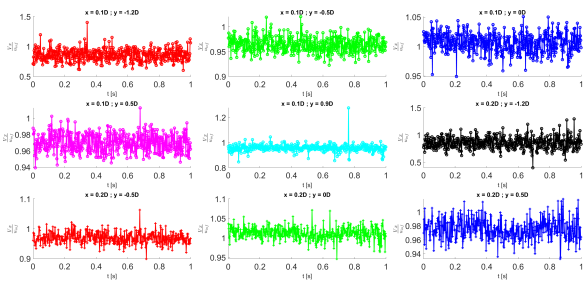

Figure C.4: No disc; steady case velocity fluctuations camera 2 part 1

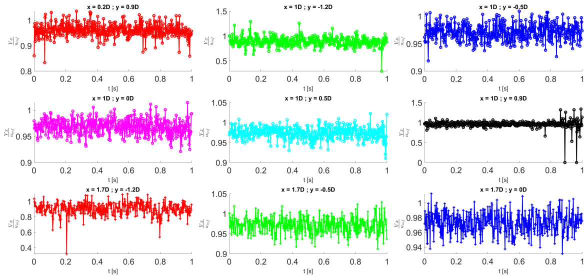

Figure C.5: No disc; steady case velocity fluctuations camera 2 part 2

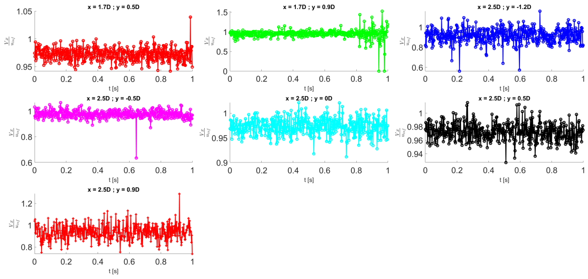

Figure C.6: No disc; steady case velocity fluctuations camera 2 part 3

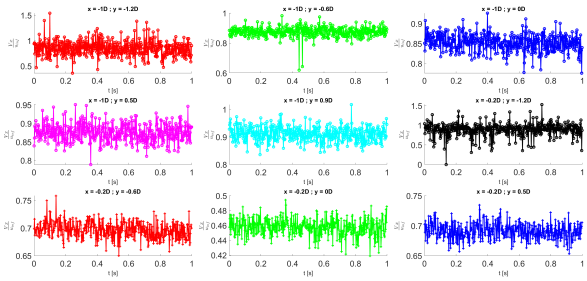

Figure C.7: Disc 1; steady case velocity fluctuations camera 1 part 1

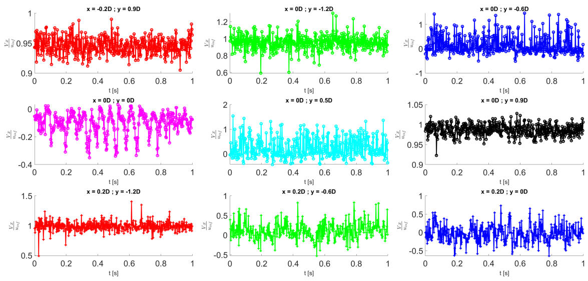

Figure C.8: Disc 1; steady case velocity fluctuations camera 1 part 2

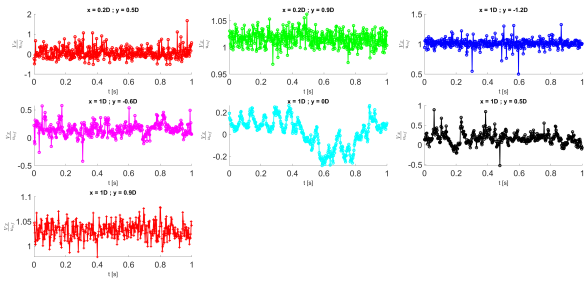

Figure C.9: Disc 1; steady case velocity fluctuations camera 1 part 3

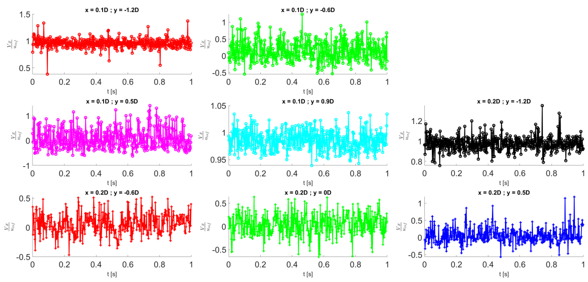

Figure C.10: Disc 1; steady case velocity fluctuations camera 2 part 1

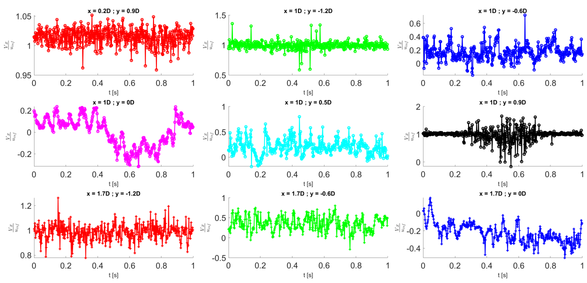

Figure C.11: Disc 1; steady case velocity fluctuations camera 2 part 2

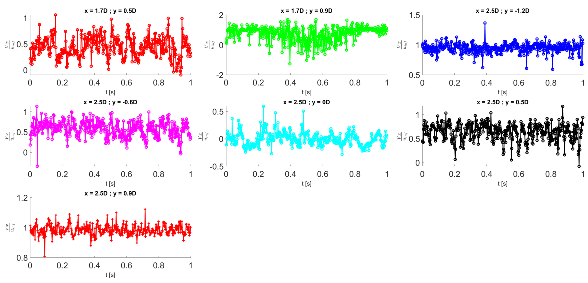

Figure C.12: Disc 1; steady case velocity fluctuations camera 2 part 3

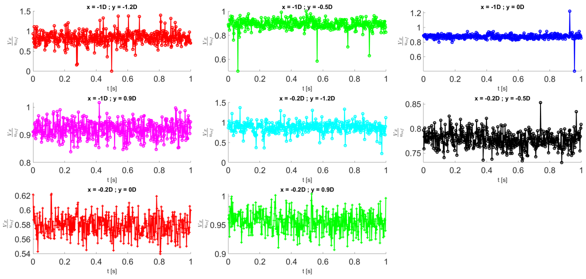

Figure C.13: Disc 2; steady case velocity fluctuations camera 1 part 1

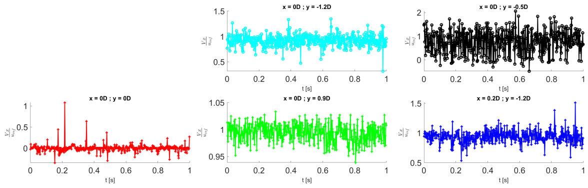

Figure C.14: Disc 2; steady case velocity fluctuations camera 1 part 2

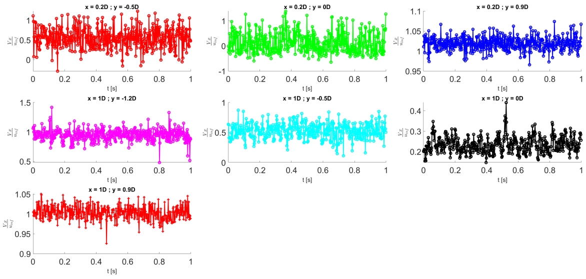

Figure C.15: Disc 2; steady case velocity fluctuations camera 1 part 3

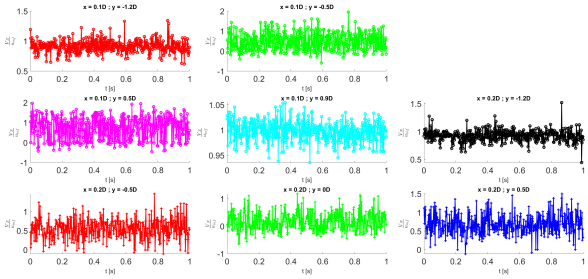

Figure C.16: Disc 2; steady case velocity fluctuations camera 2 part 1

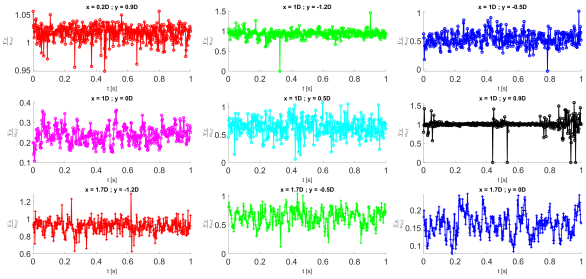

Figure C.17: Disc 2; steady case velocity fluctuations camera 2 part 2

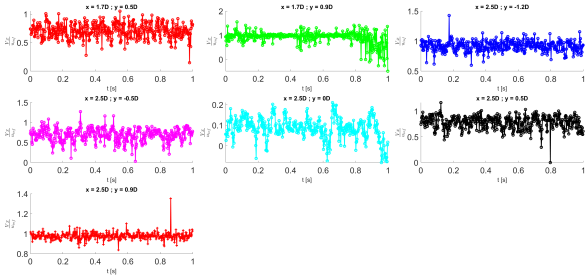

Figure C.18: Disc 2; steady case velocity fluctuations camera 2 part 3

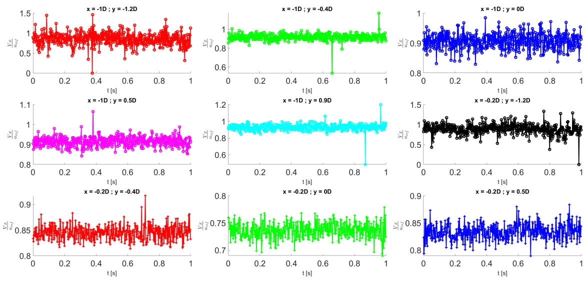

Figure C.19: Disc 3; steady case velocity fluctuations camera 1 part 1

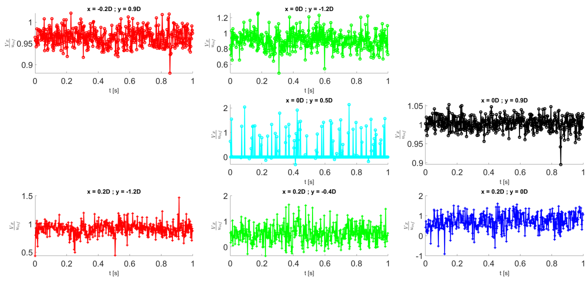

Figure C.20: Disc 3; steady case velocity fluctuations camera 1 part 2

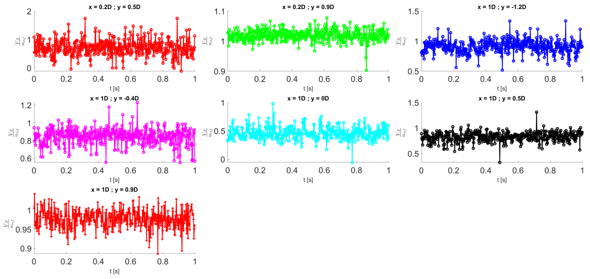

Figure C.21: Disc 3; steady case velocity fluctuations camera 1 part 3

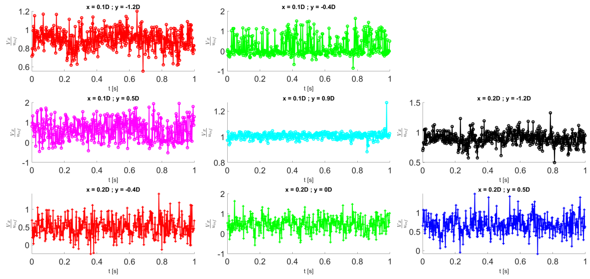

Figure C.22: Disc 3; steady case velocity fluctuations camera 2 part 1

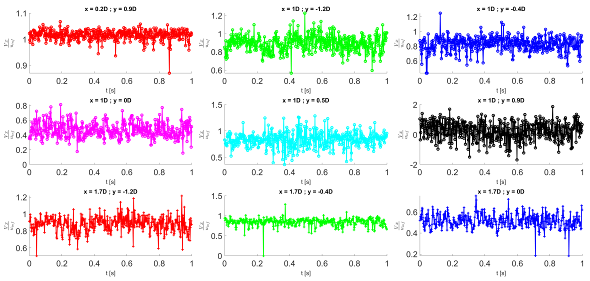

Figure C.23: Disc 3; steady case velocity fluctuations camera 2 part 2

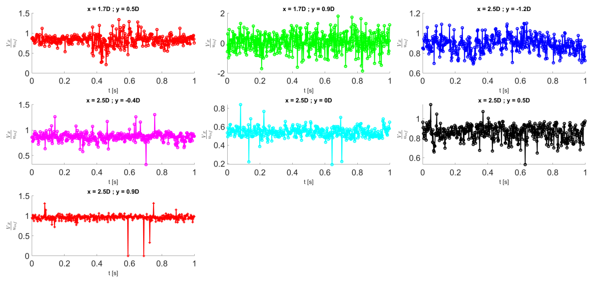

Figure C.24: Disc 3; steady case velocity fluctuations camera 2 part 3

C.2. Convergence steady cases

In the previous section of this appendix, velocity fluctuations in steady cases were introduced. This section shows that the results are converging. All cases are converging pretty fast to an average value.

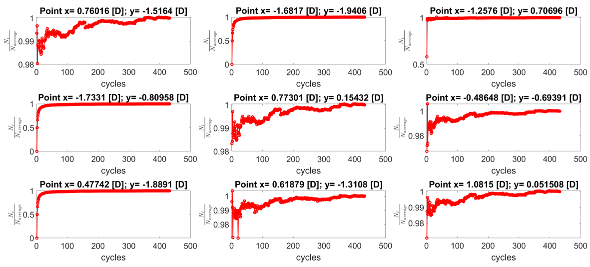

Figure C.25: No disc; steady case convergence camera 1

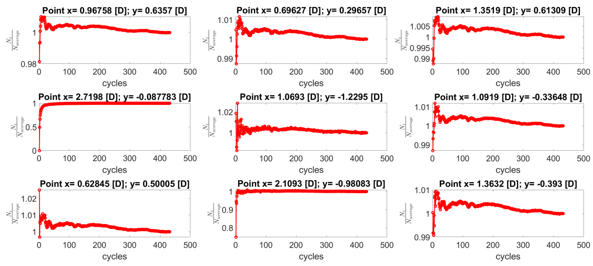

Figure C.26: No disc; steady case convergence camera 2

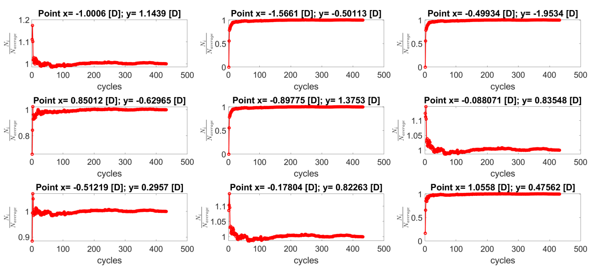

Figure C.27: Disc 1; steady case convergence camera 1

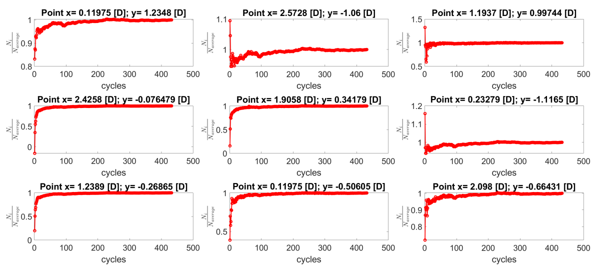

Figure C.28: Disc 1; steady case convergence camera 2

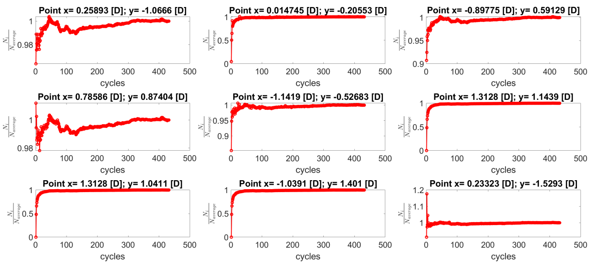

Figure C.29: Disc 2; steady case convergence camera 1

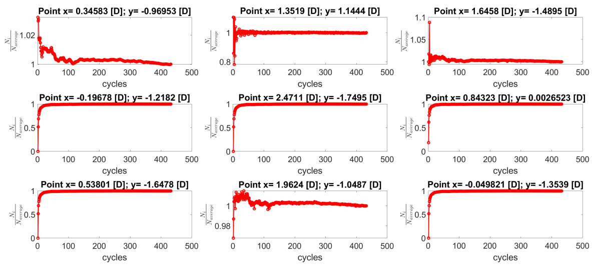

Figure C.30: Disc 2; steady case convergence camera 2

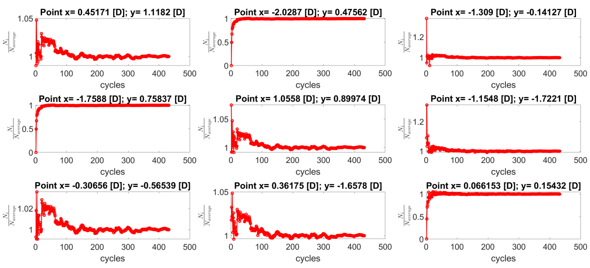

Figure C.31: Disc 3; steady case convergence camera 1

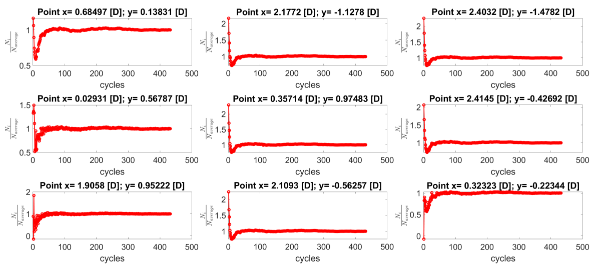

Figure C.32: Disc 3; steady case convergence camera 2

D

Appendix D

This appendix analyses the velocity profile and turbulent intensity of specific x-locations. The velocity and turbulent intensity are compared to the comparable steady state case. That means a steady state case with the same actuator disc.

The velocity at the 'inlet' of the flow field does not have a straight profile. The velocity in the area between the gust vane wakes is much higher than the velocity in the wake of the gust vanes. This was also something which was already visible in flow field analysis (see chapters 5, and 6). Another thing in the flow field here is the velocity inside and outside of the gust vane wake. At the bottom of the figure, it is visible that the velocity at the outside of the gust vane is higher for low gust vane phases. If the phase angle is changed, the velocity will be reduced. This is in comparison to the area between the two gust vane wakes, where the velocity is exactly the opposite. At negative gust vane angles, the velocity is lower than for positive gust vane angles. This is the result of the position of the two gust vanes. The incoming flow will move around the two gust vanes. For low gust vane phases, the airflow has a large gap to pass through. However, if the gust vane phase is increased, the gap between the two gust vanes in combination with the moving wake of the gust vanes, the velocity is increased due to a smaller area in between the wake of the gust vanes.

Next to the gust, the tubulence intensity is shown. The turbulence intensity is defined as:

$$I = \frac{u'}{U} \tag{D.1}$$

In this formula, u' is the root mean square value of the velocity in x-direction, and U is the average velocity in x-direction [34].

At $x = -1D$, the velocity profile shows the fluctuations around the steady case velocity. For low phases, the velocity between the two gust vanes is lower than the steady case velocity, while for larger phases the velocity is higher than the steady case. Outside the gust vane wake, the absolute value of the velocity is the opposite of what happens between the two gust vanes.

The turbulence intensity is the lowest between the two gust vane wakes. In the gust vane wake, the turbulence intensity is high. The turbulence intensity is high here, because the airflow wants to recover to its original freestream state; but the wake of the two gust vanes is such strong that the velocity is lower (see figures D.1, and D.2).

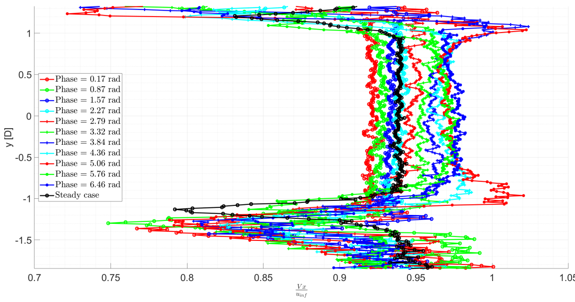

Figure D.1: No disc; Dimensionless velocity versus y [D] at $x = -1D$; 5 degree amplitude; 6Hz

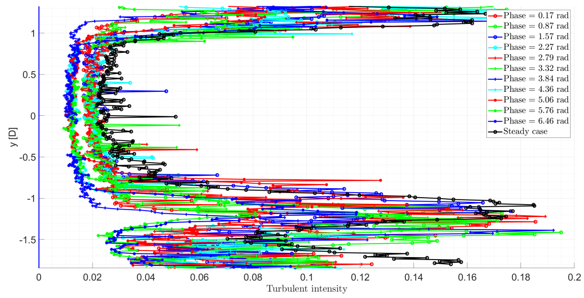

Figure D.2: No disc; Dimensionless turbulence intensity versus y [D] at $x = -1D$; 5 degree amplitude; 6Hz

If the gust vane frequency is changed, or the amplitude of the gust vanes is changed, the velocity profile looks the same as for the small amplitude and low frequency cases.

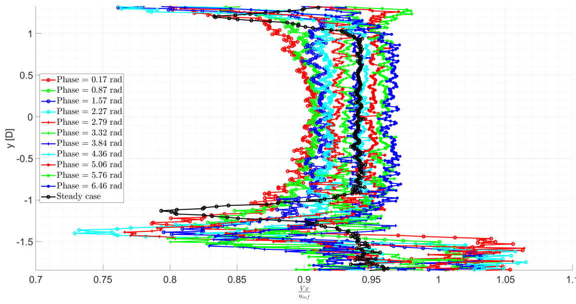

Figure D.3: No disc; Dimensionless velocity versus y [D] at $x = -1D$; 5 degree amplitude; 12Hz

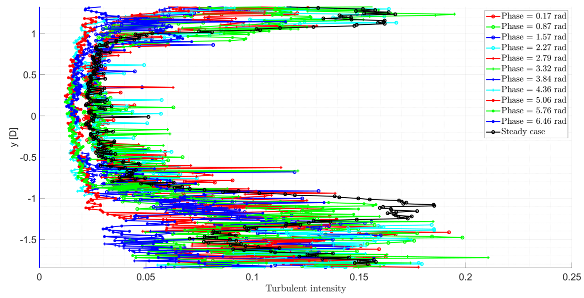

Figure D.4: No disc; Dimensionless turbulence intensity versus y [D] at $x = -1D$; 5 degree amplitude; 12Hz

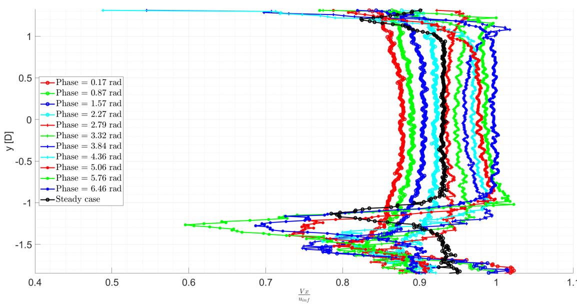

Figure D.5: No disc; Dimensionless velocity versus y [D] at $x = -1D$; 10 degree amplitude; 6Hz

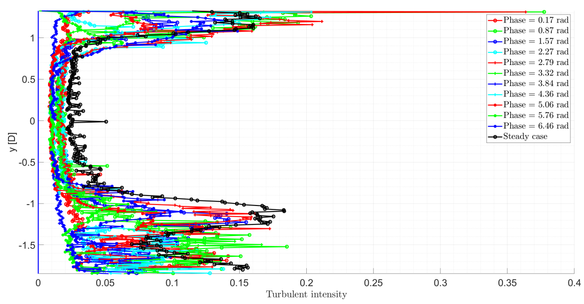

Figure D.6: No disc; Dimensionless turbulence intensity versus y [D] at $x = -1D$; 10 degree amplitude; 6Hz

If an actuator disc is added, neither the velocity profile, nor the turbulence intensity is changed. This seems reasonable, because the location was set at $x = -1D$ upstream of the location of the actuator disc. If the x-location is shifted to the location of the actuator disc ($x = 0D$), the profile of the turbulence intensity seems not to change. However, the velocity profile is different. Since the actuator disc is extracting energy from the flowfield, the velocity of the disc is reduced to almost zero. The zero velocity component has to do with the mask placed in the Davis software for analyzing reasons.

A better location is a little bit further downstream, for example $x = 0.2D$. Without an actuator disc, the situation does not change in comparison to the $x = -1D$ location (see figures D.7; D.8; D.9; D.10; D.11, and D.12).

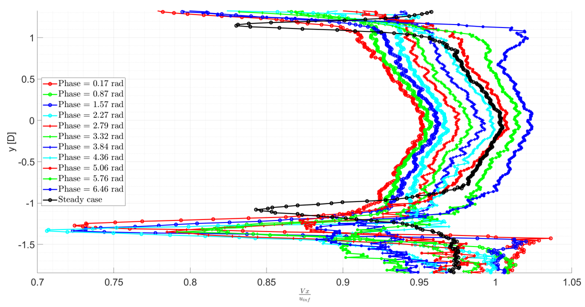

Figure D.7: No disc; Dimensionless velocity versus y [D] at $x = 0.2D$; 5 degree amplitude; 6Hz

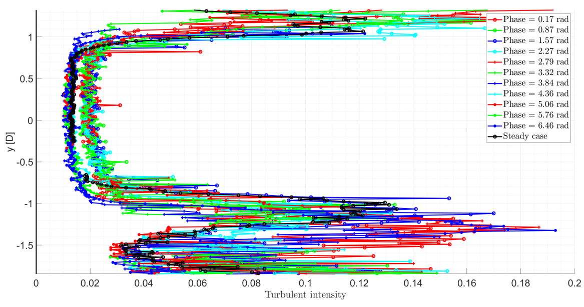

Figure D.8: No disc; Dimensionless turbulence intensity versus y [D] at $x = -0.2D$; 5 degree amplitude; 6Hz

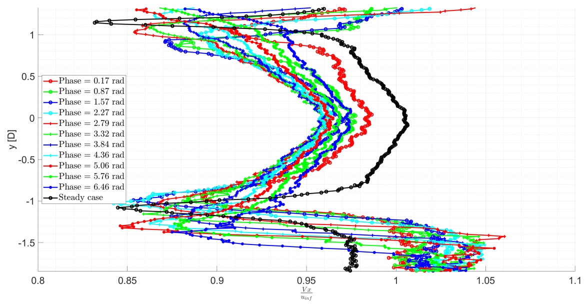

Figure D.9: No disc; Dimensionless velocity versus y [D] at $x = 0.2D$; 5 degree amplitude; 12Hz

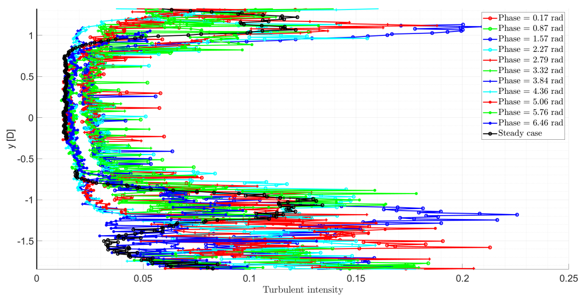

Figure D.10: No disc; Dimensionless turbulence intensity versus y [D] at $x = 0.2D$; 5 degree amplitude; 12Hz

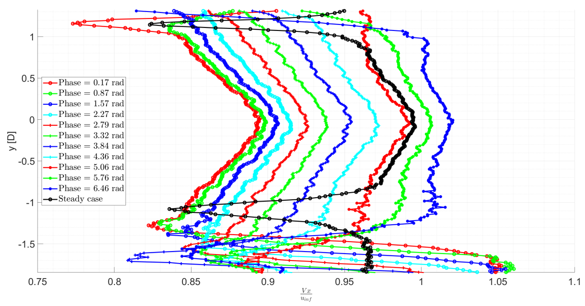

Figure D.11: No disc; Dimensionless velocity versus y [D] at $x = 0.2D$; 10 degree amplitude; 6Hz

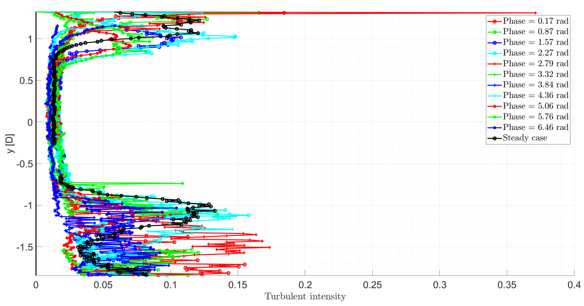

Figure D.12: No disc; Dimensionless turbulence intensity versus y [D] at $x = 0.2D$; 10 degree amplitude; 6Hz